On Formation of Multiple Zonal Jets in the Oceans

P. Berloff [*,†], **I. Kamenkovich**[‡], **and J. Pedlosky**[*]

April, 2008

Submitted to: *Journal of Fluid Mechanics*

Corresponding author e-mail and address: **pberloff@whoi.edu**;

Woods Hole Oceanographic Institution, Clark Lab., MS#29, Woods Hole, MA 02543, USA.

---

[*] Physical Oceanography Department, Woods Hole Oceanographic Institution, USA
[†] Department of Applied Mathematics and Theoretical Physics, University of Cambridge, UK
[‡] RSMAS, University of Miami, USA

Abstract

Multiple alternating zonal jets observed in the ocean are studied with an idealized quasigeostrophic model with the background flow imposed. Formation of the jets is governed by a spatially nonlocal mechanism that involves basin-scale instabilities. Energy of the background flow is released to the primary unstable mode with long meridional and short zonal lengthscale. This mode undergoes secondary instability that sets meridional scale of the multiple zonal jets. In a zonal channel, eddies generated by the instabilities maintain several weakly damped annular modes that significantly modify the jets and feed back on the primary instability.

It is found that the jets are driven by the mixed, barotropic-baroclinic dynamics and maintained by either Reynolds or form stress forcing, depending on the direction of the background flow. The underlying dynamical mechanism is illuminated both with statistical analysis of the nonlinear equilibrium solutions and with linear stability analysis of the flow components. Finally, we find that the jets are associated with alternating weak barriers to the meridional material transport, but locations of these barriers are not unique.

1. Introduction

The principal phenomenon studied in this paper is existence of multiple, alternating zonal jets in the oceans. Solid observational evidence of these jets emerged over the last few years, and it is plausible that these jets are dynamically similar to those observed in the atmospheres of giant gas planets, such as Jupiter (e.g., Kondratyev and Hunt 1982).

In this introduction we pose the problem, discuss the background, and describe the ocean model. The phenomenology of the modeled jets is described in section 2. Sections 3 and 4 deal with analysis of the nonlinear solutions and with the linear stability analysis of the flow components, respectively. The role of meridional boundaries is discussed in section 5, and the conclusions and discussion follow in section 6.

1.1 Statement of the Problem

Our principal hypothesis is that the oceanic jets are driven by the intrinsic nonlinear dynamics associated with mesoscale geostrophic eddies [1], rather than by inhomogeneities of the oceanic boundary conditions. The role of the eddies in driving the jets obtains most of the attention, but roles of the wind stress patterns (Treguier et al. 2003) and topographic effects (e.g., gaps in the mid-ocean ridges) should be seriously taken into account.

Our research strategy is the following. We find solutions of a hierarchy of idealized ocean models (their formulation and discussion is in section 1.3) that simulate multiple zonal jets and analyze the corresponding large-scale/eddy interactions. Our focus is on the time-mean patterns of both the flow and the eddy fluxes. (Analysis of the low-frequency variability of the jets is left for the future.) We also analyze material-transport properties and linear-stability aspects of the flow. The results are validated against a comprehensive simulation of the North Atlantic, which is analyzed in the

[1] A comprehensive recent review of the various mesoscale eddy effects in the ocean is by McWilliams (2007).

twin paper (Kamenkovich et al. 2008, hereafter KBP08). However, we completely neglect effects of bottom topography, complex coastline geometry, and inhomogeneity of the external forcing. On the other hand, the simplicity of the models allows us to vary such important parameters of the problem as the background flow intensity, lateral viscosity, bottom friction, large-scale dissipation, and planetary vorticity gradient.

Within the hierarchy, comparison of solutions of the *zonal-channel* and *closed-basin* ocean models allows us to assess the importance of the meridional boundaries. Comparison of the corresponding *two-* and *three-layer* solutions illuminates the importance of the higher vertical modes. Finally, in the models the eddies and, thus, the jets, are maintained by either *eastward-* (EB) or *westward-* background (WB) flow. (In the studies of the atmospheric jets, only eastward-background flows are considered, because of the generic equator-to-pole decrease of temperature associated with them.)

The main distinctions of this work from the previous studies are in the more detailed analysis of the baroclinic eddy effects and barotropic-baroclinic interactions, in the dynamical insights from the linear stability analysis of the flow components, and in understanding the important roles of the annular modes. Also, we connected these results with other important ideas, such as potential vorticity homogenization arguments and Rhines scaling for meridional structure of the jets.

1.2 Background

The severe lack of the detailed oceanic observations of the multiple zonal jets in the ocean is the main challenge — it leaves theoretical assumptions largely unconstrained. Nevertheless, there are ideas in the literature that have some observational support in the atmosphere. Also, over the last few years, predictions of the multiple zonal jets have emerged from the state-of-art, comprehensive, general circulation models of the ocean. In this section we briefly review most of the relevant literature.

Oceanic multiple zonal jets are *latent jets*, because they are substantially weaker than the associated mesoscale eddies, which tend to mask the jets in instantaneous snapshots. Typical velocities of the time-mean oceanic jets reach only a few centimeters per second, and only in the upper ocean. Due to their latency, the oceanic multiple jets can be interpreted as preferential pathways for the eddies. Atmospheric multiple zonal jets are *manifest jets*, because they are substantially stronger than the associated eddies. On giant gas planets, such as Jupiter, the jets manifest themselves as stripes of slightly different colors that have been observed for centuries.

Observational evidence of the oceanic jets has a short history, because the latent jets are difficult to observe. Anisotropy of the Lagrangian float dispersion and the corresponding dominance of its zonal component has been systematically measured and reported over the last two decades (e.g., Krauss and Boning 1987), but until recently these measurements failed to reveal the spatial structure of the corresponding anisotropic flow patterns. Only more recently, with more detailed float measurements, an array of alternating zonal flows has been observed in the deep Atlantic Ocean (Hogg and Owens 1999; Ollitrault et al. 2006). A similar flow pattern is recovered by the inversion of the observed tracer distribution (Herbei et al. 2008). In the Southern Ocean, hydrographic observations indicate that at least 3 zonal jets are embedded in the Antarctic Circumpolar Current (Nowlin and Klinck 1986; Orsi et al. 1995). Over the last few years, analysis of satellite altimetry observations dramatically changed our knowledge of multiple zonal jets (Maximenko et al. 2005; Sokolov and Rintoul 2007a; Huang et al. 2007): it is argued that the jets populate all oceans, and in the midlatitudes they are characterized by the meridional scale of about 300 km and by the zonal extent comparable with that of the basin. However, the vertical structure as well as the seasonal and interannual variabilities of the jets are not fully detected from the altimetry. Observations also detect noticeable deviations of the jets from strict zonality (Maximenko et al. 2008).

Comprehensive reviews of the relevant theoretical ideas have been written by Rhines (1994), and by Dritschel and McIntyre (2008). The theoretical cornerstone was laid by Rhines (1975), who, from the analysis of decaying barotropic turbulence, argued that the meridional scale (a.k.a. Rhines scale) of the jets is determined by a balance between the nonlinear advection and the linear meridional advection of the planetary vorticity [2]. Since then, all works on the jets invoke both nonlinearity of the flow and the meridional gradient of the Coriolis parameter (i.e., the beta effect) as the fundamental aspects. However, the required degree of nonlinearity is uncertain, and it has been argued that the barotropic jets are a weakly nonlinear phenomenon (Manfroi and Young 1999, 2002). Also, it has been argued that the jets emerge only if the beta effect exceeds a critical threshold, which depends on the latitude, the first Rossby deformation radius, and the intensity of the energy cascade (Smith 2004; Theiss 2004). Finally, with the latitude-dependent planetary-vorticity gradient, an equatorward energy cascade has been proposed that should amplify the jets at the low latitudes (Theiss 2004).

Since the pioneering work of Williams (1978), who looked at an idealized but global model of the atmosphere, particular attention has been paid to the barotropic dynamics: the barotropic jets emerge in forced-dissipative regimes driven by the spatially homogeneous, small-scale random forcing. Here, the central assumption is that the imposed forcing qualitatively approximates interactions of the barotropic mode with the transient baroclinic eddies. In this type of model, the jets are formed due to the inverse energy cascade, which is typical for 2D turbulence. In the cascade the beta effect creates strong anisotropy and channels a large fraction of the energy into the multiple zonal currents. Thus, the corresponding energy spectrum is strongly anisotropic (e.g., Vallis

[2] The Rhines scale is commonly thought to be the physical scale at which the inverse energy cascade in the turbulence is "arrested" by the propagating Rossby waves. On the other hand, there are arguments that most of the cascading energy overcomes the "arrest" and continues to cascade up to the largest scales (Huang and Robinson 1998; Sukoriansky et al. 2007).

and Maltrud 1993; Chekhlov et al. 1996), and the spectral nonlinear interactions are significantly nonlocal (Balk et al. 1990). It is argued that the universal anisotropic energy spectrum of the jets, $E(k_m) \sim k_m^{-5}$, where k_m is meridional wavenumber, coexists with the isotropic residual Kolmogorov spectrum, $E(k) \sim k^{-5/3}$ (Galperin et al. 2004). On the other hand, the jets can be viewed as coherent structures, which are incompletely characterized by the spectra. For example, in the doubly periodic domain, barotropic dynamics generates a "saw-tooth" vorticity profile, thus confounding any scaling behavior of the statistical-equilibrium energy spectrum, and the resulting long-time average of the flow is not unique, depending on the initial state and evolution history of the flow (Danilov and Gurarie 2004; Danilov and Gryanik 2004). With the help of the stochastic structural stability approach, the barotropic jets can be described as the preferred growing structures excited by the imposed stochastic forcing (Farrell and Ioannou 2007).

Baroclinic jets as well as the barotropic-baroclinic interactions are understood even less than the purely barotropic ones, because they require more complete models with more vertical degrees of freedom. In a two-layer, double-periodic flow driven by a background, baroclinically unstable, vertical shear, multiple zonal jets emerge and persist for a long time (Panetta 1993, hereafter P93). In a broad range of parameters, meridional scaling of these jets is found consistent with the Rhines scale. The jets are maintained by divergence of the momentum rather than buoyancy eddy flux. Also, P93 reports: (a) asymmetry between the (prograde) eastward (faster but narrower) and (retrograde) westward (weaker but broader) jets [3]; (b) intrinsic low-frequency variability associated with meridional migration, meandering, and merger of the jets.

Results of P93 have been extended toward multiple zonal jets in a wind-driven, two- and three-

[3]It is argued that in the double-periodic, barotropic decaying turbulence damped only by the high-order lateral friction this asymmetry becomes reversed, because in the westward jets transient Rossby waves are dissipated more efficiently than in the eastward ones (Ishioka et al. 2007).

layer zonal-channel model (Treguier and Panetta 1994). In the regime close to the Antarctic Circumpolar Current, this study not only predicted emergence of one or two zonal jets (depending on the wind stress profile) but also showed that rough bottom topography can lead to disruption and even disappearance of these jets through generation of the bottom-trapped stationary eddies. It is argued that the wind-driven flow in the channel undergoes irregular transitions between the one- and two-jet regimes, of which the latter is characterized by less energetic eddies (Lee 1997). In this study some of the eddy-jet interactions are characterized in terms of the Rossby wave absorption at the critical latitudes. Finally, multiple jets have been found in the full and truncated P93-like models with negative β-effect in the deep isopycnal layer (Kaspi and Flierl 2007).

It has been proposed that the structure of the P93 jets can be explained in terms of the *"potential vorticity (PV) staircase" conjecture* (Baldwin et al. 2007; Dritschel and McIntyre 2008), which stems from the inhomogeneous mixing idea of McIntyre (1982). The underlying idea of the conjecture is that the cores of the (prograde) eastward jets tend to act as narrow material transport barriers that separate broad zonal bands characterized by intense meridional mixing of material by the eddies. As a result of this barrier-and-mixer pattern, the meridional profile of the flow potential vorticity, which is an approximate material quantity mixed by the eddies, tends to resemble a "staircase" (e.g., P93; Huang and Robinson 1998), and the corresponding zonal velocity develops its east-west asymmetry [4], as dictated by the PV inversion. The existence of the material transport barriers and mixers has been confirmed in a number of jet studies: in some models (Juckes and McIntyre 1987; Haynes et al. 2007; Esler 2008; Greenslade and Haynes 2008; Beron-Vera et al. 2008), in observations (Haynes and Shuckburgh 2000; Marshall et al. 2006), and in some lab experiments (Sommeria et al. 1989).

On the basis of the inviscid equivalent-barotropic, zonal-channel simulations, it is argued that:

[4] An alternative argument explaining the velocity asymmetry exploits analogy with hydraulically controlled flow and, thus, relates velocity and width of the jet (Army 1989).

(a) the meridional spacing and amplitude of the jets are regulated by the penetration threshold of the barriers, and (b) the resulting meridional spacing is given by the Rhines scale, which is based on the maximum velocity of the transient vortices adjacent to the barriers (Dritschel and McIntyre 2008). A partial "PV staircase" is found in the forced-dissipative simulations with spherical geometry (Huang and Robinson 1998; Scott and Polvani 2007) and in laboratory experiments (one of the regimes reported by Read et al. 2007). On the other hand, no such evidence is found, so far, in the ocean observations and comprehensive-GCM solutions, and to what extent the multiple zonal jets observed in the ocean are transport barriers and mixers is an open question.

Finding relationships between meridional eddy fluxes and the background flow parameters is an important issue. In some works scaling for the diffusivity is given in terms of the inverse energy cascade arguments, without explicit accounting for the multiple jets (Smith et al. 2002; Lapeyre and Held 2003). On the other hand, it is suggested that baroclinic jets have baroclinic-barotropic interactions that cause these cascade arguments to break down (Thompson and Young 2007).

Historically, many of the idealized closed-basin studies focused on dynamics of the wind-driven large-scale gyres. The gyres are characterized by a strong nonzonal flow component that tends to mask weak zonal jets embedded in the flow. Nevertheless, these jets manifest themselves by inducing enhanced material dispersion in the zonal direction (Berloff et al. 2002). The formation of zonal jets in a closed stratified basin forced by spatially homogeneous, small-scale random forcing is discussed in Berloff (2005), where it is argued that the jets are driven by nonlinear interactions of the linear resonant modes. There, it is also shown that the amplitude of the jets increases toward the western boundary. Multiple jets have also been found in non-stratified (i.e., barotropic) closed basins by Nadiga (2006) and Kramer et al. (2006): in the former study it is argued that the jet spacing is consistent with the Rhines scaling, and the latter study suggests that the jets are driven by the resonant-mode interactions. Overall, the occurrence of multiple zonal jets in a closed basin is a poorly understood phenomenon.

The dynamical relationship between the equatorial and midlatitude multiple jets is unclear, and the former are not only more manifest but also have more complicated vertical structure (Firing 1987). It is argued that the equatorial jets are maintained by instabilities of the mixed Rossby-gravity wave (Hua et al. 2008).

In comprehensive ocean GCMs, the mesoscale eddies are typically not resolved and their effects are crudely parameterized in terms of the turbulent diffusion. The first study that showed emergence of multiple (and predominantly barotropic) zonal jets in the eddy-permitting model also detected basin-scale interannual variability of the flow that might be related to the jet-generating mechanism (Cox 1987). In some of the more recent eddy-resolving computations, the emergence of the multiple zonal jets is well-documented (Nakano and Hasumi 2005; Richards et al. 2006; Huang et al. 2007; KBP08). Analysis of the dynamical balances confirms the central role of mesoscale eddies in maintaining the jets; and it is shown that the vertical structure of the jets can be quite well approximated by the barotropic and two baroclinic modes (KBP08). Moreover, it is argued that in terms of the induced sea surface height anomalies these jets are qualitatively similar to those detected in the altimetry (Maximenko et al. 2005).

In summary, past studies have not yielded a universally accepted view on the origins and dynamics of the multiple zonal jets observed in the oceans (and atmospheres). However, nearly all theories argue that the jets are a nonlinear phenomenon driven by the mesoscale eddies in the presence of the meridional gradient of the planetary vorticity. Most theories focus on barotropic dynamics, although comprehensive GCMs suggest that the jets have a large non-barotropic component. Most theories neglect effects of the lateral boundaries, although this could be the main feature that distinguishes ocean and atmosphere multiple-jet dynamics. Important remaining theoretical questions involve the meridional scaling, east-west asymmetry, eddy/large-scale interactions, and meridional transport properties of the jets. Finally, vigorous research on zonal jets is carried out by the plasma physics community — many aspects of this effort have geophysical counterparts: a comprehensive review of the subject is written by Diamond et al. (2005).

1.3 Ocean Model

This study is largely motivated by the comprehensive, eddy-resolving GCM solutions analyzed in KBP08 (Fig. 1). In this GCM the multiple jets are more pronounced in the southern half of the subtropical gyre, where the background flow is predominantly zonal and westward, and in the region of the intense eastward flow (40-55°N). In these regions, the background flow is upper-ocean intensified, and nearly zonal; it doesn't change sign with depth and decays to zero near the bottom. To a large extent, our choice of the idealized model and background flow configuration is motivated by these characteristics.

The idealized ocean dynamics employed in this study is a fairly standard quasigeostrophic one for the midlatitude circulation (e.g., Holland 1978). For most of the study, the basin is configured as zonally periodic channel with flat bottom, but a closed basin is considered as well. The flow is driven by the prescribed background velocity with vertical shear, hence the forcing can also be interpreted as imposed buoyancy flux with uniform meridional gradient. The background flow configuration is linearly unstable for the parameters of interest, and the flow solutions are full with transient eddies. We hypothesize that the jets are driven by nonlinear interactions of the background flow instabilities.

Our choice of the simple channel geometry and uniform background flow substantially simplifies properties of the original GCM solution. Here, the motivation is to establish the simplest, but physically relevant, starting point; more physical complexity can be systematically added later on. The channel geometry removes zonal inhomogeneity of the time-mean eddy fluxes. Both uniformity of the background flow and absence of the bottom topography allow us to avoid additional lengthscales of the problem. Adding meridional boundaries in the closed-basin formulation will allow us to analyze importance of the annular modes, which are removed in this case. Finally, studying multiple-jet dynamics in the channel is important because of its potential relevance to the multiple jets observed in the Antarctic Circumpolar Current and atmospheres of giant gas planets (section 1.2).

In the idealized model, physical parameters that specify stratification, planetary vorticity, and bottom friction have fairly realistic values. Eddy diffusion that represents unresolved effects of the mesoscale and submesoscale turbulence on the larger scales is characterized by relatively low values of the eddy viscosity that are typical for eddy-resolving ocean circulation models. In combination with relatively fine spatial resolution of the model, this choice guarantees that mesoscale eddies are dynamically well resolved. We focus on relatively long, multi-decadal integrations of the model that are required for accurate statistical diagnostics. Most of the presentation deals with two reference solutions, for the EB and WB flow configurations, but dependence on the main parameters is thoroughly discussed. Parameters corresponding to the reference solutions for the EB and WB flows are summarized in Table 1.

The meridional width of the reference channel is $L_y = 1800$ km, but some solutions with $L_y = 3600$ km are also discussed. The channel is zonally periodic with the period $L_x = 2\,L_y$. The bottom is flat; therefore, topographic effects, potentially important for formation of the multiple jets, are excluded. Complex coastlines and inhomogeneity of the external forcing, also potentially important factors for the jets, are excluded as well. The background planetary vorticity gradient is $\beta = 2{\times}10^{-11}$ m^{-1} s^{-1}, and the mid-channel (45^{deg} north) Coriolis parameter is $f_0 = 0.83 \times 10^{-4}$s^{-1}. The bottom friction, γ, is varied from zero to 4×10^{-7} s^{-1}, but its reference value is zero. The eddy viscosity, ν, is varied from 50 to 400 $\mathrm{m^2\ s^{-1}}$, but its reference value is 100 $\mathrm{m^2\ s^{-1}}$.

Stratification is approximated with either 2 or 3 stacked isopycnal layers. In the two-layer case, the layer depths are $H_1 = 1$ and $H_2 = 3$ km, starting from the top; and, in the three-layer case, they are $H_1 = 1$, $H_2 = 1$, and $H_3 = 2$ km, respectively. The total depth of fluid is always $H = 4$ km. Reduced gravities, g'_1 and g'_2, are associated with the density jumps across the upper and lower interfaces between the isopycnal layers, and g'_2 exists only in the three-layer model. In three-layer model, the stratification parameters are:

$$S_1 = \frac{f_0^2}{H_1\, g'_1}\,, \qquad S_{21} = \frac{f_0^2}{H_2\, g'_1}\,, \qquad S_{22} = \frac{f_0^2}{H_2\, g'_2}\,, \qquad S_3 = \frac{f_0^2}{H_3\, g'_2}\,, \tag{1}$$

and the reduced gravities are chosen so that the first, Rd_1, and the second, Rd_2, baroclinic Rossby deformation radii are 25 and 12 km, respectively. In the two-layer model, there are only 2 stratification parameters, S_1 and $S_2 = S_{21}$, and g'_1 is chosen so that the only deformation radius, $Rd_1 = g'_1\sqrt{H_1 H_2}/f_0\sqrt{H_1 + H_2}$, is 25 km.

The quasigeostrophic PV equations (Pedlosky 1987) for 3 dynamically active isopycnal layers are:

$$\frac{\partial q_1}{\partial t} + J(\psi_1, q_1) + \beta\,\frac{\partial \psi_1}{\partial x} = \nu\nabla^4\psi_1 + D_1^{LS}\,, \tag{2}$$

$$\frac{\partial q_2}{\partial t} + J(\psi_2, q_2) + \beta\,\frac{\partial \psi_2}{\partial x} = \nu\nabla^4\psi_2 + D_2^{LS}\,, \tag{3}$$

$$\frac{\partial q_3}{\partial t} + J(\psi_3, q_3) + \beta\,\frac{\partial \psi_3}{\partial x} = \nu\nabla^4\psi_3 + D_3^{LS} - \gamma\nabla^2\psi_3\,, \tag{4}$$

where the layer index starts from the top; $J(,)$ is the Jacobian operator; D_i^{LS} is the large-scale dissipation operator discussed further below; and the last term in (4) is the bottom friction. Isopycnal PV anomalies, q_i, are related to velocity streamfunctions, ψ_i, through the elliptic, PV inversion subproblem:

$$q_1 = \nabla^2\psi_1 + S_1\,(\psi_2 - \psi_1)\,, \tag{5}$$

$$q_2 = \nabla^2\psi_2 + S_{21}\,(\psi_1 - \psi_2) + S_{22}\,(\psi_3 - \psi_2)\,, \tag{6}$$

$$q_3 = \nabla^2\psi_3 \qquad\qquad\qquad + S_3\,(\psi_2 - \psi_3)\,. \tag{7}$$

The two-layer modification of the model is formulated similarly:

$$\frac{\partial q_1}{\partial t} + J(\psi_1, q_1) + \beta\,\frac{\partial \psi_1}{\partial x} = \nu\nabla^4\psi_1 + D_1^{LS}, \tag{8}$$

$$\frac{\partial q_2}{\partial t} + J(\psi_2, q_2) + \beta\,\frac{\partial \psi_2}{\partial x} = \nu\nabla^4\psi_2 + D_2^{LS} - \gamma\nabla^2\psi_2\,; \tag{9}$$

$$q_1 = \nabla^2\psi_1 + S_1\,(\psi_2 - \psi_1)\,, \tag{10}$$

$$q_2 = \nabla^2\psi_2 + S_2\,(\psi_1 - \psi_2)\,. \tag{11}$$

The isopycnal flow velocity components are found from the velocity streamfunction:

$$u_i = -\frac{\partial \psi_i}{\partial y}\,; \qquad v_i = \frac{\partial \psi_i}{\partial x}\,. \tag{12}$$

The dynamical equations are actually solved either in their original, isopycnal-layer form or in terms of their vertical-mode equivalent (McWilliams 2006). No-slip lateral-boundary conditions are used for each isopycnal layer. The mass and momentum constraints are imposed following McWilliams (1977).

The forcing in the governing equations is introduced through the imposed, background vertical velocity shear (as in Haidvogel and Held (1980), and in P93):

$$\Psi_i = -U_i\,y\,; \qquad \psi_i \longrightarrow \Psi_i + \psi_i\,, \tag{13}$$

where U_i are the background zonal-velocity parameters of the problem. We always set the deepest-layer background velocity to zero, and in the three-layer model we set $U_2 = 0.5U_1$. Given (13), the governing equations are re-written with respect to perturbations, ψ_i and q_i, around the background flow. The background velocity, U_i, is horizontally uniform — this ensures that the characteristic length scales of the multiple jets are not imposed but internally generated by the intrinsic flow dynamics. The background flow is linearly unstable for sufficiently strong velocity shear, as suggested by the classical Phillips problem (e.g., Pedlosky 1987).

In the model we impose large-scale damping, D_i^{LS}, that selectively acts on the largest scales of motion and parameterizes otherwise neglected physics that is responsible for some large-scale energy sink (e.g., meridional boundary layers and interaction with bottom topography):

$$D_i^{LS} = \lambda_{ij} \, \psi_j \, , \tag{14}$$

where λ_{ij} is the large-scale damping (tensor) coefficient, and summation over the second index, j, is assumed on the right-hand side. In the model, λ_{ij} is chosen so that if (14) is projected on the vertical modes, then λ_{ij} becomes diagonal and isotropic tensor with the magnitude given by the large-scale damping rate parameter, λ. The reference value of λ is 2×10^{-7} m^{-2} s^{-1}, but we also assessed the effect of the large-scale damping by setting λ to zero. In some previous studies of the multiple zonal jets, large-scale damping is included either explicitly (e.g., Danilov and Gurarie 2004) or implicitly, in the form of thermal radiative cooling (e.g., P93).

The governing equations, either (2)–(7) or (8)–(11), with the imposed background shear (13), are discretised with the second-order finite differences. Formulation of the Jacobians is PV flux conserving. The prognostic equations are marched in time with the leapfrog scheme and 0.5-hour time step, and the elliptic PV inversion problem is solved for the corresponding velocity streamfunctions on each time step, by a direct solver. The horizontal grid resolution is uniform, with 512×257 grid points (resolution is about 7 km) for the reference solutions. Statistically equilibrated regimes are reached after 20-40 years of integration. The analysis is based on the subsequent 100 years of integration.

2. Phenomenology of the Jets

2.1 Main Features of the Multiple-Jet Regimes

Several regimes of the equilibrium flow are found and characterized in terms of the time-mean patterns (Figs. 2 and 3). Because of the computational constraints, we focus on the channel with $L_y = 1800$ km, which is equivalent to 72 Rd_1. Some of the benchmark solutions are found for $L_y = 3600$ km (i.e., 144 Rd_1), in order to demonstrate that, as long as there are many jets in the channel, the phenomenology and dynamics are largely insensitive to L_y.

Both EB and WB flow regimes have the following common features. First, the jets are *manifest* (more so in the EB flow), that is, they are strong relative to the eddies and can be easily observed not only in the time-mean but also in the instantaneous flow fields. The barotropic component of the jets is more manifest than the baroclinic one. (In section 5, we demonstrate that in the closed basin the jets become latent rather than manifest, due to the absence of the annular modes, but many aspects of their dynamics remain similar.) Second, the jets are always asymmetric in the sense that the eastward jets are faster and narrower than the westward ones. The total eastward and westward mass transports are always equal, as a result of the zonal momentum conservation. Third, the baroclinic component of the jets is more asymmetric than the barotropic one. Not only are the baroclinic westward jets relatively weak, but they are also characterized by the time-mean zonal velocity undulations in their cores (e.g., Fig. 2b,d). Fourth, the jets adjacent to the lateral boundaries are weaker than those in the middle of the channel. Finally, we found multiple equilibria characterized by different numbers of the jets in the channel (Fig. 3; section 2.3).

Despite many similarities, there are some significant differences between the EB and WB flow regimes (Figs. 2 and 3). First, the EB jets are about twice stronger than the WB jets, for the same degree of supercriticality. This is because the critical shear is about twice larger in the EB case, thus implying 4 times more available potential energy. Second, in the EB flow barotropic and baroclinic jet components flowing in the same zonal direction are located on the same latitudes, that is, they reinforce each other; whereas, in the WB flow they oppose each other. As a result of this behavior, in the EB/WB flow deep-ocean jets are weaker/stronger than the upper-ocean ones. Finally, there are significant dynamical differences, discussed in section 3.

2.2 Lagrangian Analysis and PV Washboard

This section discusses the meridional structure of the time-mean PV and relates it to the meridional material transport. This part of the analysis connects results of this paper to the "PV staircase" paradigm addressed in many studies and discussed in section 1.2.

In the presence of a regular array of multiple zonal jets, it is not surprising to see nearly periodic deformation of the corresponding meridional PV profile. An important question is to what extent this profile tends toward the perfect staircase, corresponding to broad regions of homogenized, zero-gradient PV separated by steep PV steps, corresponding to infinitely large gradient. For the broad range of explored parameters (section 2.3), we find that PV profiles do not approach the perfect staircase; instead, they can be characterized as PV "washboards" (Fig. 4). Unlike the "staircase", these "washboards" exhibit partially homogenized zones that separate equally broad steps with modestly strong PV gradients. The latter gradients, however, exceed the background PV gradient by a modest factor of 2 or smaller. More detailed inspection reveals that some of the inter-step zones and steps incorporate more localized and weaker steps and mixing zones, suggesting that the "staircase" paradigm is even less relevant.

The "PV staircase" paradigm — commonly discussed in the context of eastward background flows — implies that the cores of the prograde (i.e., adding to the background flow) jets tend to behave as barriers to, whereas the retrograde (i.e., subtracting from the background flow) jets behave as mixers (i.e., surf zones) of the meridional material transport. Since, in the absence of diabatic sources, PV is materially conserved quantity, these barriers and mixers, if very strong, should be associated with the clear meridional PV steps and inter-step zones, respectively. Here, the snag is that most of the corresponding studies are backed up by purely barotropic models, and it remains to be seen if a perfect staircase can be reached in a more realistic configuration of a baroclinic model.

In order to clarify relationship between the "washboard" and material transport, we carried out the Lagrangian analysis of the flow. The methodology is the following. Transport of material is represented by Lagrangian particles uniformly distributed in space at the starting time and advected by the flow. Time integration of the particle trajectories is performed by a fourth-order Runge-Kutta method, with the flow velocity obtained by the bi-cubic spatial interpolation of the velocity streamfunction field. For each latitude and isopycnal layer, we find an ensemble of particles which, by the end of the specified time interval, migrated across the latitude of interest in either northward or southward direction. Each ensemble incorporates several realizations that differ by the timing at which the particles were initialized in the evolving flow. We find that the time interval of 100 days, 500 realizations, 1000 particles in each realization, and 1 day intervals between the particle releases for each realization give reliable statistics.

The *total* meridional material flux, $M_i^{tot}(y)$, is estimated by dividing the total number of particles in the corresponding ensemble by the time interval and by the number of realizations. Part of this flux needs to be sorted out, because it can be interpreted as reversible. The reversibility is associated with coherent blobs of fluid that migrate across the latitude of interest but do not cross a PV isoline that evolves in time and corresponds to the time-mean PV on this latitude. The *irreversible* component, $M_i^{irrev}(y)$, of the total flux is obtained by counting only those particles that eventually crossed the corresponding PV isoline. Fluxes $M_i^{tot}(y)$ and $M_i^{irrev}(y)$ calculated from the reference solutions are shown in Fig. 5. The irreversible flux can be a small fraction of the total flux, and, as the figure suggests, it is a more accurate detector of the barriers and mixers.

In the EB regime, the cores of the upper-ocean prograde (eastward) jets manifest themselves as weak transport barriers separated by the mixing zones. However, in the deep ocean the picture is the opposite. In the WB regime, the upper-ocean barriers — located in pairs, between the prograde (westward) and retrograde (eastward) jet cores — are the weakest. The upper-ocean prograde jets and the cores of the retrograde jets behave as very weak mixers. In the deep ocean, the barrier/mixer contrast is noticeably larger; the mixing zones are located only on the prograde jets, and the barriers are located on the southern flanks of the prograde jets. Overall, the permeability contrast between the barriers and mixers — responsible for bending the "washboard" — can be characterized by factors of about 4 and 1.5 in the EB and WB regimes, respectively.

We confirmed the configurations of the barriers and mixers with a different methodology, by solving for the meridional eddy fluxes of the passive tracer concentration. The corresponding tracer equilibrium was maintained by imposing the tracer source with uniform meridional gradient. We also calculated effective diffusivities (Shuckburgh and Haynes 2003; Greenslade and Haynes 2008), and they yielded qualitatively similar results. Existence of the weak barriers in the upper-ocean eastward jets (of the EB regime) is consistent with the observed distinct bands of chlorophyll concentrations in the multiple jets of the Southern Ocean (Sokolov and Rintoul 2007b), but more detailed observational evidence of the jet's permeability is so far not available.

We estimated how close the time-mean flow approaches the prefect staircase by solving for the velocity profiles corresponding to the perfect PV staircases in the upper and deep isopycnal layers. Inversion of PV into velocity was made with the elliptic solver from the full model (section 1.3).

The outcome yielded a qualitatively incorrect velocity field: on the same latitudes deep-ocean jets emerging on the top of the background flow are in the opposite direction to the upper-ocean jets (Fig. 6; compare with Fig. 3a,c). Amplitudes of the jets are also predicted incorrectly. This is so because the actual jets in the model have equally important barotropic and baroclinic modes, whereas the implied two-layer staircase requires unrealistically small barotropic flow component.

To summarize, we found that description of the time-mean meridional PV in terms of the "staircase" is not accurate. The observed PV pattern — referred to as the "washboard" — is associated with weak and alternating material-transport barriers and mixers. Locations of the barriers and mixers depend on direction of the background flow and depth, and the barriers are not necessarily located on the prograde jets. The time-mean flow does not approach PV staircase because of the strong barotropic mode predicted by the dynamics.

2.3 Dependence on Parameters

We define the meridional jet scale, L_j, as the lengthscale corresponding to the mean wavenumber (i.e., the one corresponding to the median value in the spectrum), k_j, of the meridional power spectrum, $E(k)$, of the time-mean and zonally averaged, zonal barotropic velocity (Fig. 7). The barotropic component of velocity is chosen for compatibility and comparison with numerous previous studies of the multiple jets in barotropic models (section 1.2). Thus, L_j is diagnosed from the following relationships:

$$L_j \;=\; \frac{2\pi}{k_j}\,, \qquad 2\int_0^{k_j} E(k)\,dk \;=\; \int_0^{\infty} E(k)\,dk\,. \tag{15}$$

The above definition is different from the one used in P93 and Berloff (2005), where k_j corresponds to the maximum of $E(k)$. This is motivated by the fact that the spectrum typically has two extrema (see also annular-mode spectra in section 4.3): the new definition removes potential discontinuities from the functional dependency of k_j on parameters of the problem.

An important lengthscale of the problem is the Rhines scale:

$$L_r \; = \; (\frac{U}{\beta})^{1/2} \,, \tag{16}$$

where U is some velocity scale that characterizes transient fluctuations of the flow. There is ambiguity in choosing U, nevertheless in P93 it is argued that with U chosen as the square root of the eddy kinetic energy, meridional width of the multiple zonal jets scales with (16): i.e., $L_j \sim L_r$. (An alternative choice of U might be based on the barotropic-mode or upper-ocean eddy kinetic energy.)

The dependence of L_j on the background shear is obtained by calculating 2 sets of solutions that have either eastward or westward U_1, and $U_2 = 0$. All other parameters are as in the reference solutions. Overall, L_j increases with shear, but the underlying relationship is not simple. At least 3 different solution branches, obtained by starting the model from different initial conditions, are found in each set of the solutions (Fig. 8a). These branches have significant overlaps in terms of U_1, and, thus, they are multiple equilibria of the flow characterized by different numbers of the jets. By plotting the ratio $r = L_j L_r^{-1}$ against U_1, we find that L_j does not scale with L_r, even on individual branches (Fig. 8b). The Rhines scaling (16) implies that r is constant, which is apparently not the case, since r changes by a factor more than 5 over the explored range of U_1. A better scaling estimate is $r = c_1 + c_2\, U_1$, where the constant coefficients can be estimated from the EB- and WB-flow linear fits (Fig. 8b).

The dependence of L_j on β is studied by varying β around its reference value of 2×10^{-11} m s^{-1} (Fig. 9). L_j is minimal on the plateau that includes the reference value of β, and it gradually increases away from it. The Rhines scaling (16) is generally not confirmed, since r is not constant. However, in the EB flow, for β in the range between 1 and 2×10^{-11} m s^{-1}, the Rhines scaling is approximately confirmed, which is consistent with P93, where similar regime is analyzed. For smaller values of β, flow solutions are characterized by intense jets near zonal boundaries, hence comparison with the unbounded-domain results of P93 is not valid.

Variations of the bottom friction parameter, γ, reveal that, for both background flow directions, L_j moderately decreases when γ increases from zero to physically more realistic values (Fig. 10a). In the WB flow, this tendency reverses at $\gamma \approx 10^{-7}$ s^{-1} (spin-down time of about 4 months). The corresponding minimum of L_j is explained in section 2.4. The increase of L_j at larger values of γ is associated with the fading of the barotropic component of these jets due to intense bottom friction. This large-γ regime is dominated by the boundary jets and, therefore, is not in the main focus of this study. In the EB flow, L_j drops by 30% as γ increases from zero to about 10^{-8} s^{-1} (spin-down time of about 1-2 weeks); after that it remains largely insensitive to further increase of γ. In the range 10^{-7} s^{-1} $< \gamma < 410^{-7}$ s^{-1}, that has been explored in P93, L_j is approximately proportional to L_r. This implies that Rhines scaling reported in P93 is consistent with our results. For smaller values of γ and in the WB flow, this scaling is not confirmed.

We also varied eddy viscosity, ν, from the half of the reference value of 100 m^2 s^{-1} to the value at which flow becomes linearly stable (Fig. 10b). Exploration of very large Reynolds numbers corresponding to even lower values of ν is left for the future, as it requires massive computations on the finer horizontal grids needed for resolving finer lengthscales of the eddies. Overall, L_j increases with ν, more steeply in the WB flow. There is a sign of convergence of L_j at the values of ν smaller and about the reference value of 100 m^2 s^{-1}, suggesting robustness of the multiple jet configuration. Rhines scaling for the sets of solutions with variable ν is not confirmed as, over the explored range of ν, r decreases by a factor of 4 in the WB flow, and by about 40% in the EB flow.

The importance of the second baroclinic mode is studied by comparing two- and three-layer versions of the model (section 1.3). The three-layer reference solutions have important similarities and differences with their two-layer counterparts (Fig. 11; compare with Fig. 2). The similarity of the meridional jet structures allows us to focus the presentation on the two-layer flow regimes and to make connections to the three-layer regimes only when necessary. The main difference is the significant reduction of the barotropic component of the jets in the presence of the second baroclinic mode. This result undermines the common assumption (section 1.2) that the structure of the barotropic component of the jets can be properly captured with a purely barotropic model (see also demonstration of the importance of baroclinic-baroclinic interactions in section 3.3). In the WB flow, the second baroclinic mode plays more important role than in the EB flow. This is so because interactions with it result in significant changes of the first baroclinic mode component. This is so because of the enhanced importance of the deep-ocean flow, which is better represented with the increased vertical resolution.

2.4 Special Flow Regimes

Some solutions in the explored parameter range exhibit relatively weak multiple jets in the interior of the channel. In the EB flow, this flow behavior is achieved at small values of β, that correspond to more supercritical background flows. This regime is characterized by very energetic eddies. The time-mean flow is characterized by a few broad barotropic jets responsible for large values of L_j (Fig. 9a), by broad and weak baroclinic westward flow in the interior of the channel, and by intense and narrow baroclinic eastward jets near zonal boundaries. In the interior, there are relatively small meridional undulations of the baroclinic velocity on the scale of the barotropic jets. This flow regime is driven by the energetic eddies that meridionally mix buoyancy and significantly flatten the background isopycnals, so that the time-mean flow becomes less supercritical. Such strongly supercritical regimes are not seen in the counterpart GCM (KBP08), hence they are not the focus of our study.

In the WB flow, a similar regime with weak interior jets coexisting with strong near-boundary jets is found for large values of γ (Fig. 10a). The eddies are not exceptionally strong in this regime, but the time-mean jets, and especially their barotropic component, are very weak due to the bottom friction. The eddies are dominated by very pronounced meridionally elongated patterns ("noodles" from section 4), which are particularly efficient in mixing buoyancy and flattening the background isopycnals. These "noodles" are so efficient because they are not strongly localized on the weak jets (section 4.7). Also, stronger "noodles" favor shorter L_j (section 4.5). Overall, this flow regime is explained with the linear stability arguments as well as the reference flow regimes.

In the channel, *multiple* (i.e., more than 1 jet in one direction and 2 returning jets in the opposite direction) time-mean jets exist only when the large-scale damping is weak. That is, multiple jets are transient features that slowly merge together; they exist only during the transient spin-up stage, which lasts for several decades. We looked at λ ranging from 0 to 20 m^{-2} s^{-1} and found that L_j increases with decreasing λ. We will briefly consider here the $\lambda = 0$ case, referred to as the "merged-jets" regime (Fig. 12). Overall, this regime is similar to that studied by Lee (1997), and its main features are the following. First, the "merged-jets" solutions appear in pairs characterized by oppositely directed barotropic flow components — this is another example of the ubiquitous multiple equilibria. In the EB flow, the corresponding baroclinic flow components also oppose each other. Second, eddies in the "merged-jets" regime are weak relative to the time-mean flow. This regime is not consistent with the observed multiple and relatively narrow oceanic jets, which can be explained by significant large-scale damping caused by bottom topography and meridional boundaries in the real ocean (section 5).

3. Nonlinear Dynamics

3.1 Eddy Fluxes

Dynamical analysis of the flow solutions is based on calculating eddy fluxes of PV and its components: relative vorticity,

$$R_i \;=\; \nabla^2 \psi_i \,, \tag{17}$$

and isopycnal stretching (take $S_{22} = S_3 = 0$ in the two-layer model),

$$B_1 \;=\; S_1\,(\psi_2 - \psi_1)\,; \qquad B_2 \;=\; S_{21}\,(\psi_1 - \psi_2) + S_{22}\,(\psi_3 - \psi_2)\,; \qquad B_3 \;=\; S_3\,(\psi_2 - \psi_3)\,, \tag{18}$$

which corresponds to anomaly of the buoyancy. The main focus of the presentation is on the two-layer dynamics; the results of the three-layer model are discussed when the contribution of the second baroclinic mode to the dynamics is discussed.

First, the flow solutions are decomposed into the time-mean, $\overline{\psi_i}$, and fluctuation, ψ_i', components. The fluctuations are referred to as the (mesoscale) eddies. In the ith isopycnal layer, the eddy PV flux (vector) is defined as

$$\mathbf{f}_i(t,x,y) \;=\; \mathbf{u}_i\, q_i - \overline{\mathbf{u}}_i\, \overline{q_i}\,, \tag{19}$$

and the eddy fluxes of R, $\mathbf{f}_{R_i}$, and B, $\mathbf{f}_{B_i}$, are defined similarly. Eddy PV flux also consists of the time-mean and fluctuation components:

$$\mathbf{f}_i(t,x,y) \;=\; \overline{\mathbf{f}_i}(x,y) + \mathbf{f}'_i(t,x,y)\,, \tag{20}$$

where

$$\overline{\mathbf{f}_i}(x,y) \;=\; \overline{\mathbf{u}'_i\, q_i'}\,, \tag{21}$$

and there are analogous decompositions for the R- and B-fluxes. In the channel, due to the zonal symmetry, the time-mean fluxes have only meridional components (Figs. 13–14). In all solutions, eddy PV and buoyancy fluxes are directed down-gradient relative to the corresponding time-mean quantities; in this sense, these fluxes are diffusive. Relative-vorticity fluxes, in contrast, can be both down- and up-gradient.

The EB jets are essentially maintained by convergence of the upper-ocean $\overline{\mathbf{f}_R}$, which is consistent with conclusion of Thompson and Young (2007). However, the dynamics is a fundamentally two-layer one, as indicated by the important contribution of $\overline{\mathbf{f}_B}$. In the EB flow, $\overline{\mathbf{f}_R}$ and $\overline{\mathbf{f}_B}$ nearly cancel each other in the cores of the prograde jets, where they have well-defined local extrema. These partial eddy PV flux barriers, which correspond to this cancellation, are consistent with the associated weak material transport barriers (section 2.2). These barriers are separated by the partial mixing zones. In the deep ocean, the weak barriers and mixers exchange their locations (section 2.2), and the up-gradient $\overline{\mathbf{f}_R}$ competes with the $\overline{\mathbf{f}_B}$ in the retrograde jets. In the WB flow, in terms of the eddy flux patterns, the upper layer plays the role of the EB flow deep layer (Fig. 14). Contrast between the barriers and mixers is relatively weak, and there are meridional high-frequency variations associated with $\overline{\mathbf{f}_B}$. All of this is consistent with the material transport analysis (section 2.2). In the next section we analyze divergences of the eddy fluxes and their components.

3.2 Formulation of the Eddy Forcing and Its Components

The dynamical effect of the eddies is illuminated by time averaging the governing equations. The time-mean eddy forcing term,

$$F_i(x,y) \;=\; -\nabla\overline{\mathbf{f}_i}\,, \tag{22}$$

can be interpreted as internally generated PV forcing that maintains the time-mean flow (i.e., the multiple zonal jets). Minus divergences of $\mathbf{f}_R$ and $\mathbf{f}_B$ are the Reynolds, F_{R_i}, and form stress forcing, F_{B_i}, respectively. In the channel, the time-mean PV balance is between eddy forcing and dissipation. The key dynamical question concerns the composition of the eddy forcing in terms of the momentum and buoyancy components, and the vertical mode contributions. Analysis of the eddy forcing in terms of the vertical mode interactions is useful, because it permits direct comparison with the single-mode models, such as the barotropic one.

The vertical-mode velocity streamfunction and potential vorticity are related to the corresponding isopycnal-layer quantities as:

$$\phi^{(i)}(t,x,y) \;=\; \theta_{ij}\,\psi_j(t,x,y)\,, \qquad p^{(i)}(t,x,y) \;=\; \theta_{ij}\,q_j(t,x,y)\,, \tag{23}$$

where superscript is the mode index; summation over $j = \overline{1,N}$ (N is the number of the active isopycnal layers/vertical modes) is assumed; and θ_{ij} is the transformation matrix calculated from the stratification parameters (e.g., McWilliams 2006). The corresponding inverse transformation matrix is:

$$\omega_{ij} \;=\; \theta_{ij}^{-1}\,. \tag{24}$$

In terms of the vertical modes, relationship (5)–(7) that connects PV and velocity streamfunction fields is diagonalized:

$$p^{(i)} \;=\; \nabla^2\phi^{(i)} + T^{(i)}\,\phi^{(i)}\,, \tag{25}$$

where $T^{(i)}$ are transformed stratification parameters. The ordering is such that $T^{(1)}=0$ (barotropic) and $T^{(i)}<T^{(i+1)}$ (baroclinic modes). The governing equations are projected on the vertical modes in accord with (23), and the corresponding nonlinear terms are:

$$nonlinear^{(i)} \equiv \theta_{ij}\,J(\psi_j,q_j) \;=\; \theta_{ij}\,\omega_{jk}\,\omega_{jl}\,J(\phi^{(k)},p^{(l)}) \equiv \Theta^{(i)}_{kl}\,J(\phi^{(k)},p^{(l)})\,, \tag{26}$$

where $\Theta^{(i)}_{kl}$ are the nonlinear-term transformation matrices, and summation over the repetitive indices is assumed. It is easy to show that in the three-layer model:

$$\Theta^{(1)}_{ij} \;=\; 0 \quad \mathit{if} \quad i \neq j\,; \tag{27}$$

$$\Theta_{ij}^{(2)} \; = \; 0 \quad if \quad i=j=1\,, \quad or \quad i=1,\, j=3\,, \quad or \quad i=3,\, j=1\,; \tag{28}$$

$$\Theta_{ij}^{(3)} \; = \; 0 \quad if \quad i=j=1\,, \quad or \quad i=1,\, j=2\,, \quad or \quad i=2,\, j=1\,. \tag{29}$$

Eddy forcing is also projected on the vertical modes:

$$\overline{F^{(i)}}(x,y) \equiv -\Theta_{kl}^{(i)}\,\overline{J(\phi'^{(k)},p'^{(l)})} \equiv \sum_{k,l}^{N}\overline{F_{kl}^{(i)}} \; = \; \sum_{k,l}^{N}(\overline{F_{R_{kl}}^{(i)}}+\overline{F_{B_{kl}}^{(i)}})\,. \tag{30}$$

We focus on relative contributions of individual vertical-mode interactions to $\overline{F^{(i)}}$ — the corresponding matrix, $\rho_{kl}^{(i)}$, has elements that sum up to the unity:

$$\rho_{kl}^{(i)} \; = \; \frac{\iint \overline{F_{kl}^{(i)}}\,\overline{F^{(i)}}\,dx\,dy}{\iint \overline{F^{(i)}}^{2}\,dx\,dy}\,, \tag{31}$$

It is also decomposed into the Reynolds stress, $\rho_{R_{kl}}^{(i)}$, and form stress, $\rho_{B_{kl}}^{(i)}$, forcing components.

3.3 Analysis of the Eddy Forcing

With the eddy forcing analysis presented in this section, we capture the essentials of the large-scale/eddy interactions driving the jets. In particular, we analyze vertical-mode interactions, compare two- and three-layer dynamics, and find Reynolds and form stress contributions. In the channel, total eddy forcing is always balanced by the dissipation terms, which are dominated by the lateral friction. The large-scale dissipation is never a significant part of the balance, but the bottom friction contributes to it when γ is large. Many properties of the eddy forcing discussed in this section are predicted by the linear stability analysis (section 4).

Both in the EB and WB flows, the time-mean barotropic eddy forcing, $\overline{F^{(1)}}$, is concentrated around the cores of the eastward jets (Fig. 15). The corresponding barotropic-barotropic, $\overline{F_{11}^{(1)}}$, and baroclinic-baroclinic, $\overline{F_{jj}^{(1)}}$ ($j > 1$), components are equally important and have similar patterns (Fig. 15). The corresponding values of $\rho_{jj}^{(1)}$ (Table 2) suggest the following conclusions. First, the barotropic component of the multiple jets cannot be accurately modelled with purely barotropic dynamics driven by small-scale random fluctuations, which are often thought of as approximation for the baroclinic eddy forcing (section 1.2). Either the first baroclinic mode has to be explicitly taken into account, or the external forcing has to include some jet-like structure that accounts for the baroclinic eddy effects. Second, the barotropic eddy forcing components corresponding to the barotropic-barotropic and baroclinic-baroclinic interactions are positively correlated, that is, they reinforce rather than compete with each other. Third, comparison of the two- and three-layer barotropic dynamics suggests that the contribution of the second baroclinic mode is relatively unimportant in the WB flow, and moderately important in the EB flow. In the EB flow, $\overline{F_{11}^{(1)}}$ accounts for nearly 3/4 of the total two-layer eddy forcing, but in the three-layer model it accounts for less than 1/2 of the eddy forcing, suggesting that the relative contribution of the barotropic-barotropic interaction decreases with better vertical resolution.

The baroclinic dynamics is more complex than the barotropic one, because of the many eddy forcing terms involved. The first and second baroclinic-mode ρ-matrices are given in Tables 3 and 4, respectively, and the former ρ-matrix is calculated for both the two- and three-layer models. Meridional profiles of the baroclinic eddy forcing and some of its components are shown in Fig. 16. Analysis of the ρ-matrices and the meridional profiles suggests the following conclusions. Overall, both barotropic-baroclinic and baroclinic-baroclinic interactions are equally important in the EB and WB flows, and both of them maintain the jets. The second baroclinic mode is important for both background flow directions. Otherwise, the EB and WB flow dynamics are rather different.

In the EB flow, the baroclinic component of the jets is maintained/resisted by the Reynolds/form stress forcing. In the three-layer model, the form stress forcing plays resisting role in the second-mode baroclinic dynamics, and this role is due to interactions with the second baroclinic mode. The resisting role of the form stress forcing indicates baroclinic instability of the jets (Pedlosky 1987).

On the other hand, advections of the barotropic and first-baroclinic relative vorticities by the first baroclinic mode (i.e., the corresponding Reynolds stress forcings) maintain the jets — this can be viewed as a “negative” eddy viscosity effect (e.g., Starr 1968). This fundamental dynamics of the flow is explained in section 4 with the linear stability analysis.

In the WB flow, both in the two- and three-layer models, the Reynolds and form stress forcings act oppositely to what is found in the EB flow. The baroclinic components of the jets are maintained mostly by the form stress forcing. The Reynolds stress forcing associated with advection of the barotropic relative vorticity by the baroclinic modes acts in a sense opposite to the form stress forcing. Thus, the eddies act to destroy the horizontal shear through the eddy viscosity effect (a.k.a. barotropic instability), but they maintain properly tilted isopycnals and, hence, the jets through the converging eddy buoyancy flux. Although, the ultimate source of the energy is the baroclinic tilt of interface, locally, the available potential energy is actually increased in the jets. Advection of the baroclinic relative vorticity by the baroclinic modes is relatively unimportant; and cross-interactions of the baroclinic modes are more important than their self-interactions. The WB eddy forcing also contains the meridional high-frequency harmonic that, along with the key dynamics, is explained with the linear stability analysis (section 4).

4. Linear Stability Problem

The linear stability analysis considered in this section is an extension of the classical works (Phillips 1956; Pedlosky 1975a). The presentation is focused on the linearized two-layer dynamics, although we also looked at the three-layer model, in a similar way.

4.1 Formulation

The linearized governing equations of the two-layer dynamics are:

$$\frac{\partial q_1}{\partial t} + J(\Psi_1, q_1) + J(\psi_1, Q_1) + \beta\,\psi_{1x} \quad = \quad \nu\nabla^4\psi_1 + \lambda_{1j}\,\psi_j\,, \tag{32}$$

$$\frac{\partial q_2}{\partial t} + J(\Psi_2, q_2) + J(\psi_2, Q_2) + \beta\,\psi_{2x} \quad = \quad \nu\nabla^4\psi_2 + \lambda_{2j}\,\psi_j - \gamma\nabla^2\psi_2\,, \tag{33}$$

where Q_i and Ψ_i are the background PV and velocity streamfunction, respectively. We find that in the linear stability calculations the effect of the large-scale damping is negligible, therefore, in the following analysis we set λ_{ij} to zero.

Three types of the background flow are considered: (1) zonal, meridionally uniform flow; (2) combination of (1) with meridional, zonally periodic flow; and (3) zonal, meridionally nonuniform flow. The first type, given by (13), is the simplest one: it corresponds to the background flows used in all nonlinear calculations of section 3. The corresponding critical eigenmode describes the primary instability. The second type of the background flow is dictated by the critical modes of the flow of the first type:

$$\Psi_i \;=\; -U_i\,y + \int_0^x V_i(x)\,dx\,, \tag{34}$$

and it yields critical eigenmode describing the secondary instability. We consider meridional velocity components that are zonally periodic:

$$V_i(x) \longrightarrow A_v\,V_i\,\cos(2\,\pi\,x/L_0 + \Phi_i)\,. \tag{35}$$

Here, V_i, L_0, and Φ_i are given by the primary instability pattern, and the amplitude A_v is a new parameter of the problem. Finally, with the third flow type we analyze the stability of the finite-amplitude zonal jets:

$$\Psi_i \;=\; -A_u \int_0^y U_i(y)\, dy\,. \tag{36}$$

The linearized equations are Fourier transformed in time and in either one or both horizontal directions (appendix A). The direction that is not Fourier transformed is discretised with second-order finite differences and the spatial resolution is kept the same as in the full nonlinear model. We tested that the outcome is not sensitive to further refinement of the grid. For flow of the third type, a no-slip boundary condition is applied on the zonal boundaries. The discretised equations are solved numerically, as the generalized eigenvalue problem. The outcome is in terms of the eigenmode patterns and the eigenvalues, which specify growth rates and temporal frequencies of the eigenmodes.

4.2 Uniform Background Flow: Unbounded Domain

Marginal stability curves corresponding to uniform zonal flow of variable strength are shown in Fig. 17, and the typical dispersion relationships are shown in Fig. 18. Overall, the dispersion relationship is that of the classical Rossby waves modified by the background shear and damping. Without damping and with equal layer depths, this is the Phillips problem (Pedlosky 1987). In both EB and WB flows, and depending on the parameters of the problem, the critical eigenmode (Fig. 18) has relatively large zonal wavenumbers, k, which correspond to the period of 180-270 km. Given $Rd_1 = 25$ km, this is 7-11 Rd_1 — noticeably longer than $2\,\pi\,Rd_1$. The critical meridional wavenumbers, l, are always equal to *zero*, hence the critical eigenmode can be characterized as a set of *meridional alternating jets*: following Pedlosky (1975a) we refer to such pattern as the *“noodles”*. In the supercritical EB/WB flow, the phase of the critical eigenmode always propagates to the east/west, and the corresponding eigenperiods are interannual/intermonthly. Regardless of the background shear, there are also very weakly damped eigenmodes with small k and l — they can be easily excited by transient forcing. In the next section we argue that some of the eigenmodes with $k = 0$ (annular eigenmodes) and small l significantly contribute to the multiple jets.

The "noodles" are specific Rossby waves propagating either in the same direction as the background flow or against it: the latter/former occurs in the EB/WB flow. Increasing the speed of the background flow results in shorter time periods, longer zonal wavelengths, and larger growth rates of the "noodles" (Fig. 17). We also studied the dependence on ν, γ, and β. The magnitude of the critical background flow strength increases with ν and β, but does not depend on γ. the zonal eigenperiod, $2\,\pi/k$, increases moderately with ν and very weakly with γ. This is because Newtonian damping, unlike the bottom drag, acts selectively on the smaller scales and, thus, moves the stability threshold to larger scales. The time period is largely insensitive to ν; variation of γ changes it noticeably only in the EB flow, so that larger friction implies shorter period. Increasing β decreases the zonal eigenperiod for both background flow directions — this makes the "noodles" more narrow. The corresponding time period becomes even longer/shorter in the EB/WB flow, increasing asymmetry between the EB and WB "noodles".

To summarize, generation of the "noodles" is a very robust phenomenon, but the details are sensitive to the background flow and other parameters. In the ocean regions populated by the multiple zonal jets, there are recent observations of the sea surface meridional patterns consistent with "noodles" (Sen et al. 2006; Huang et al. 2007), and qualitatively similar patterns are diagnosed from the comprehensive GCM solutions (KBP08).

4.3 Annular Modes

The analysis of the previous section is extended from the unbounded domain to the zonal channel. Stability properties of the corresponding flow are found to be very similar: details of the zonal-channel "noodles" are accurately predicted by the unbounded-domain analysis. In the free-slip channel, the critical (i.e., with the largest growth rate) mode is exactly the sum of the 2 critical eigenmodes of the unbounded domain, with $\pm l_{crit}$. In the no-slip channel, which is in the focus of this study, the above mode is modified near the boundaries. We find that this modification has little impact on other properties of the mode.

Weakly damped annular eigenmodes predicted by the unbounded-domain analysis are modified by the zonal boundaries (Fig. 19). The bounded modes preserve their weak decay rates, and the modes with fewer meridional lobes need weaker forcing to get excited. The spectrum of the bounded annular modes is discrete. Here, an important property of the annular modes is that they do not depend on the background flow, as can be easily seen from the governing equations.

We order the annular modes in terms of increasing decay rate. It can be easily seen that the baroclinic component of the reference EB and WB solutions is dominated by the eighth mode and the "merged-jets" flow regime is dominated by the second mode (section 2). Half of the annular modes (e.g., the third mode in Fig. 19a) have zonal velocity which is meridionally antisymmetric with respect to the middle of the channel. Such modes imply non-zero total viscous flux of the relative vorticity from the lateral boundaries into the channel interior, therefore, they do not satisfy the momentum constraint imposed by the dynamics (McWilliams 1977). This explains why multiple-jet time-mean flows predicted by the full model have zonal velocity nearly symmetric around the middle latitude — they are dominated by the meridionally symmetric modes [5]. Decay rates of the annular modes increase with the mode index more than in the unbounded domain, so that the tenth mode decays 5 times faster than the first one. This suggests that the full flow is likely to be dominated

[5]There are special antisymmetric flow configurations that have no relative vorticity flux from the lateral boundaries, but, for unknown to us reasons, the dynamics doesn't favor antisymmetric flow contributions.

by relatively few annular modes. In terms of the vertical structure, the annular modes are all mixed, but the interesting lower modes have a ratio of their barotropic to baroclinic component, which is either small (< 0.1) or large (> 10): such modes can be accurately (but not precisely) characterized as barotropic and baroclinic. In the reference channel, the first dozen modes with weak decay rates are baroclinic, and the barotropic modes of interest have higher indices.

How do the annular modes contribute to the time-mean multiple jets? Let's consider a set of the $n = \overline{1, N}$ annular mode streamfunctions projected on the vertical modes, $\chi_n^{(i)}(y)$ (each vertical mode is denoted by the superscript). The modes are ordered in terms of the increasing decay rate and are normalized by the energy norm. The observed, time-mean jet streamfunction can be represented as:

$$\varphi^{(i)} \;=\; \sum_{1}^{N} C_n \, \chi_n^{(i)} \,, \tag{37}$$

where the set of C_n is the annular mode spectrum. (If N is the number of all meridional degrees of freedom, then this relationship is exact). We define the scalar product of two streamfunction fields as

$$\{\phi \, \psi\} \;=\; \frac{1}{L_y} \int_0^{L_y} \phi(y) \, \psi(y) \, dy \,. \tag{38}$$

Multiplication of (37) by each of the N annular modes, yields the corresponding set of linear equations on C_n:

$$\{\varphi \, \chi_n\} \;=\; \sum_{m=1}^{m=N} C_n \, \{\chi_n \, \chi_m\} \,. \tag{39}$$

Scalar products of the annular modes on the r.h.s. of (39) are generally non-zero for $n \neq m$, because the modes are not orthogonal to each other.

We solved the linear algebraic problem (39) numerically, not only for the time-mean jets but also for the spin-up experiments discussed in section 4.4. The outcome, illustrated by Fig. 20, can be summarized as the following. The dominant annular modes appear as a result of the transverse instability of the “noodles” (sections 4.4 and 4.5). These modes are picked up by the meridional scale of this instability (note, that meridional scaling in Fig. 22 matches meridional scaling of the annular modes associated with the primary spectral peaks in Fig. 20a). The annular mode spectrum is dominated by very few barotropic and baroclinic primary modes: even 1-2 such modes capture the velocity profile of the zonal jets quite well (Fig. 20b,c). The barotropic modes have generally larger C_n, and this is even more so in the WB flow regime, but this simply reflects the fact that the barotropic mode is stronger than the baroclinic one. Later in the flow spin-up process, when the primary annular modes saturate (section 4.4), the spectrum develops secondary baroclinic- and barotropic-mode peaks (e.g., as around $n = 50$ and 80 in Fig. 20a). These peaks correspond to the excited secondary annular modes, which have meridional scale twice shorter than that of the primary annular modes. The secondary modes are responsible for the east-west asymmetrization of the barotropic and baroclinic multiple jets.

Analysis of the annular modes provides simple explanation of the “merged-jets” regime (section 2.4) achieved with no large-scale damping ($\lambda = 0$). In the flow spin up towards the “merged-jets” regime, the annular-mode spectral power slowly and gradually shifts towards the lowest modes — this process is associated with merger of the individual zonal jets, which appear initially. This is because, in comparison with the reference value of λ, decay rates of the lowest annular modes decrease by 2 orders of magnitude. The higher modes remain virtually unaffected, and the shapes of the annular modes are not significantly affected by the large-scale damping, therefore, apart from keeping the flow out of the “merged-jets” state, the damping does not introduce any other significant effect on the multiple jets.

To summarize, in addition to the “noodles”, the weakly damped annular modes are another important and previously missed aspect of the multiple-jet dynamics in the zonal channel. These modes not only provide the natural template for the multiple zonal jets, but also “localize” the “noodles” and modify the eddies (sections 4.6 and 4.7).

4.4 Spin-Up Experiments

Analysis of the fully nonlinear spin-up of flow from the state of rest, which is seeded with random small-amplitude perturbations, provides further insights in the process of multiple jet formation (Fig. 21).

On the first stage of the spin up, structure of the emerging “noodles” (Fig. 21a) is very consistent with the primary instability, linear “noodles” predicted by the linear stability analysis (section 4.3). Also, in Fig. 21a there are “braids” that distort the “noodles”: we associate them with weakly damped modes occupying the lower left corners of the dispersion diagrams in Fig. 18. We checked that if initial perturbation is chosen in the form of the linear “noodles”, then the large-scale modes are not significantly excited, because they are initially absent.

On the second stage of the spin up, the “noodles” succumb to the secondary instability (Fig. 21b), discussed in section 4.5. This instability imposes meridional scale of the future multiple jets. On this scale, eddy forcing associated with the secondary instability excites the corresponding annular mode, which becomes the primary annular mode of the emerging jets (section 4.3).

The third spin-up stage is localization of the flow instabilities by the growing dominant annular mode (Fig. 21c). During this process, the secondary annular mode — associated with the secondary spectral peak in Fig. 20a and responsible for the east-west asymmetry of the jets — is also excited as a result of the eddy forcing associated with the meridionally localized instabilities (section 4.6). In the meantime, some jets can merge, because the flow regime allows for multiple equilibria characterized by slightly different numbers of the jets (sections 2.1 and 2.3). The jets become manifest, but their development saturates on some level. The saturation mechanism is associated with equilibrated localization of the instabilities (section 4.7). The third spin-up stage is realizable only in the open-channel situation, because there are annular modes available. If the annular modes are not permitted (section 5), the multiple jet formation process stops at the second stage.

Comparison of the spin-up experiments with oceanic observations is problematic, since the ocean stays close to the equilibrated state effected by the seasonal and low-frequency variability. However, the emergence of "noodles" followed by the emergence of zonal currents is consistent with observations of seasonally modulated instabilities of the South Pacific subtropical countercurrent (Qiu et al. 2008). In the comprehensive GCM, the first and second spin-up stages are also reported in some parts of the basin (KBP08).

4.5 Secondary Instability

The finite-amplitude "noodles" are unstable to the transverse secondary instability, which is consistent with the one seen in the spin-up solutions (section 4.4). Flow for the corresponding linear stability problem consists of the ensemble of finite-amplitude "noodles", given by the primary stability analysis, superimposed on the uniform background flow [6] (Fig. 22a,e). The amplitude of the reference "noodles" is given by the spin-up solutions at the end of the first spin-up stage, but we treat the amplitude as a free parameter, as in (35). The "noodles" are kept "frozen" in time, that is, their propagation is not taken into account, for simplification of the linear analysis. We verified that this simplification does not introduce large errors by calculating growing and breaking "noodles" in the fully nonlinear model. In these calculations, the initial "noodles" were meridionally and periodically perturbed with different length scales: meridional scale corresponding to the fastest growing transverse mode was consistent with the scale predicted by our linear analysis.

[6]Here, the argument is similar to Manfroi and Young (2002), but the background flow and baroclinic effects are taken into account.

The secondary instability, given by the fastest growing eigenmode, is meridionally periodic, with the scale L_j corresponding to the multiple zonal jets (Fig. 22). In the zonal direction, the secondary eigenmodes are not trapped to the individual "noodles", as indicated by their amplitudes that never approach zero. The zonal period of the eigenmode amplitude is half of the period of the "noodles", thus, indicating that the corresponding northward and southward flow jets provide equal contributions to the eigenmode. Other eigenmode properties differ for the EB and WB flows: in the former case, the eigenmode is characterized by the "checkerboarded" velocity streamfunction, whereas, in the latter case, the streamfunction is "striped". This is because the WB eigenmode is characterized by weaker zonal variation of the phase. As can be seen in their zonal averages, both the "checkerboarded" and "striped" patterns have obvious contributions of the dominant annular modes. Hence, the transverse instability provides an efficient mechanism of the energy transfer from the meridional to zonal motions.

The meridional lengthscale of the secondary instability, that is, the scale of the fastest growing eigenmode, strongly depends on the amplitude of the "noodles" (Fig. 23a). If the amplitude approaches zero, then the meridional lengthscale increases to infinity, because instability of the background flow with infinitesimal "noodles" are the "noodles" themselves. If the amplitude becomes 1.5-2 times larger than the background zonal flow, then the meridional lengthscale saturates at about 300-400 km (i.e., 12-16 Rd_1), which is consistent with the emerging multiple zonal jets. Can the transverse instability be dominated by larger lengthscales associated with the weaker "noodles"? For instance, Fig. 23a suggests that critical instabilities of the WB flow "noodles" with the velocity amplitude of about 1.5-4.0 cm s^{-1} have the meridional lengthscale of about 600 km. The answer is no, because instabilities of the weaker "noodles" have growth rates that are smaller than the growth rates of the "noodles" themselves (Fig. 23b). This implies that the growing primary-instability pattern, until it reaches significant amplitude, will overtake and dwarf the growing secondary instability. We confirmed this by fully nonlinear calculations, as those described in the beginning of this section.

Finally, we find that eigenperiods of the critical eigenmodes are infinitely large. Thus, the corresponding phase velocity is zero, and the secondary instabilities do not propagate in space. This also implies that the transverse instability does not propagate meridionally, hence the multiple zonal jets are pinned to their locations and do not average out in the time mean.

To summarize, meridional scale of the multiple zonal jets is set by the transverse instability of the "noodles" growing on the background shear. The corresponding critical eigenmode efficiently projects on the dominant annular mode that acts as the template for the emerging jets. The corresponding energy transfer from the meridional to zonal motions is consistent with observations (Qiu et al. 2008).

4.6 Localization of the Eddies by the Annular Modes

Spin-up of the annular modes is an essential aspect of the multiple jets forming in an open channel. When the important annular modes reach large amplitudes, they effectively modify background flow and alter the eddies to a degree which needs to be accounted for by proper extension of the linear stability analysis (section 4.2).

We take the time-mean velocity profile (i.e., jets plus the background flow), as predicted by the nonlinear model, and scale its non-background part with the nondimensional amplitude, A_u, which is subsequently varied from 0 to 1.5. Thus, $A_u = 0$ corresponds to the uniform background flow (sections 4.2 and 4.3), and $A_u = 1$ corresponds to the actual velocity profile predicted by the nonlinear model. Since the time-mean velocity profile is nearly symmetric with respect to the middle latitude of the channel, for additional clarity we make it exactly symmetric by setting:

$$u_i(y) \longrightarrow A_u\, u_i(y) \longrightarrow \frac{A_u}{2}\left(u_i(y) + u_i(L_y - y)\right). \tag{40}$$

The corresponding linear stability problem is solved not only for $0 < A_u < 1.5$, but also, as a sensitivity study, for several values of ν and γ. The critical eigenmode for $A_u = 0$ corresponds to the "noodles" modified by the zonal boundaries (section 4.3). The near critical eigenmodes have zonal wavenumbers similar to the critical one; their meridional wavenumbers such that they can be interpreted as meridionally elongated cells with either 1, or 2, or even more meridional zero crossings between the boundaries. We tracked the evolution of these modes, as well as evolution of the "noodles", for gradually increasing A_u. The outcome is that at large A_u the eigenmodes become significantly transformed and meridionally localized on the multiple jets (Fig. 24). We leave out details of the complex localization process and focus on the important aspects.

One such aspect is grouping of the critical and nearly critical eigenmodes into 3 eigenmode types, discussed further below, that are well-defined at large A_u (Fig. 24). The exact threshold value of A_u (somewhere around 0.5) is hard to define, but it is significantly less than 1.

The eigenmode properties depend both on A_u and friction parameters, but at large A_u this dependence gradually fades away: when A_u approaches 1.3 — regardless of the background flow direction and friction parameters — l_{crit} and ω_{crit} converge to the universal values (Fig. 25). Overall, with the increasing A_u, the meridional period of the critical mode increases by about 30%. The meridional period tends to increase with the increasing ν and γ, as in the primary stability analysis (section 4.2). The eigenperiod decays with A_u, reaching the values of less than 1 day for A_u near 1.5. It is sensitive to friction only in the EB flow regime with $A_u < 0.5$, where stronger friction implies a shorter eigenperiod. Finally, the eigenperiod is negative/positive in the WB/EB case, indicating that the critical mode propagates to the west/east.

We focused on the 10 eigenmodes ("top 10") with the largest (positive) growth rates, ordered them according to their growth rates, and traced them over the range of A_u. The three types of the eigenmodes can be characterized as the following (Figs. 26 and 27). In terms of the amplitude, the type-1 and type-2 eigenmodes are trapped to the westward jets (i.e., prograde/retrograde jets in the WB/EB flow), and the type-3 eigenmode is trapped to the eastward (i.e., opposite) jets. Formally, we measure the degree of the amplitude/jet alignment by correlating the corresponding profiles: the correlation coefficients are strongly positive/negative for the type-1 and -3 eigenmodes, and weakly negative for the type-2 ones. In terms of the amplitude, all eigenmodes are meridionally symmetric with respect to the middle latitude of the channel, but in terms of the phase they are either symmetric or antisymmetric. (For A_u approaching 1.5, some of the eigenmodes split in pairs that have meridionally asymmetric amplitudes, which are equivalent under the transformation $y \longrightarrow L-y$.) The westward-trapped eigenmodes are meridionally localized on the pairs of westward jets and are characterized by either 2 (type-1) or 4 (type-2) maxima of the amplitude. In the latter case, the amplitude has the characteristic "double-hump" structure in each jet. The eastward-trapped eigenmodes also come in pairs, except for the eigenmode trapped on the central eastward jet. Meridional structure of the eigenmodes indicates that the dynamics remains meridionally nonlocal for all values of A_u, although degree of the nonlocality decreases with increasing A_u.

The eigenmodes can be additionally classified into types "A" and "B", which are characterized by the meridionally antisymmetric/symmetric eigenphase. In case of the type-1 and -2 eigenmodes, the "A" and "B" subtypes are characterized by either zero or non-zero amplitudes, respectively, in the eastward-jet region separating the large-amplitude westward-jet regions.

There are significant differences between the EB and WB flow eigenmodes — they underpin the corresponding kinematic and dynamic differences found in the nonlinear model solutions (section 3). In terms of the growth rates, type-1/type-2 eigenmodes dominate in the EB/WB flow regimes; but the corresponding subtype "A" always dominates over "B". Consistent with the nonlinear analysis, the EB/WB eigenmodes have larger amplitudes in the upper/deep ocean. In all of the eigenmodes, but substantially more so in the WB flow, there is significant vertical phase shift, which indicates intensive conversion of the potential energy between the eigenmode and the time mean flow. In the WB flow, the type-1 and type-3 amplitudes are more tightly confined to the upper-ocean jet cores. Finally, in the case of $A_u = 1$ the eigenperiods of the type-1, -2, and -3 eigenmodes are about 200/80, 800/100, and 100/200 days for the EB/WB flow regimes.

4.7 Analysis of the Localized Eigenmodes

Analysis of the eigenmodes meridionally localized on the multiple zonal jets (section 4.6) yields the following results.

The structure of the transport barriers and mixers predicted by the nonlinear model (section 2.2) is explained by the dominance of the westward-trapped eigenmodes. In the EB flow, the upper-ocean barrier/mixer contrast is more pronounced than in the WB flow, because the maximum/minimum amplitude ratio is more pronounced in the type-1 rather than type-2 eigenmode. In the deep ocean, the type-3 EB eigenmode is more efficient in terms of the meridional mixing efficiency, therefore, it is responsible for establishing eastward jets as the mixers. In the WB flow, the deep-ocean barriers are associated with the main zeros of the type-2 eigenmode, that are located between the double humps; and the double barriers around the upper-ocean prograde jet cores are associated with the secondary maxima and minima of the type-2 amplitude.

Analysis of the eigenmodes allows an interpretation of the dynamical results of section 3. First, we calculated the eddy forcing patterns associated with the barotropic and baroclinic self-interactions of the eigenmodes (Figs. 28 and 29) and correlated them with the corresponding PV profiles of the time-mean jets. Significant positive/negative correlation suggests that the eigenmode of interest maintains/resists the corresponding vertical-mode component of the jets (Table 5). We find that the baroclinic jets are maintained by the type-1 and -2 eddy forcings, and the barotropic jets are maintained by the type-3 eddy forcing. The baroclinic jets are resisted by the type-3 eddy forcing but substantially more so in the WB flow. The barotropic jets are weakly resisted by the type-1 eddy forcing, and the type-2 eddy forcing resists them only in the EB flow.

Regardless of the background flow direction, the barotropic jets are maintained by the same type-3 eigenmode — this explains the dynamic similarity of the EB and WB flows. Also, the type-3 eddy forcing has equally important barotropic-barotropic and baroclinic-baroclinic components that are qualitatively similar to those predicted by the nonlinear model. The baroclinic jets can be maintained by either type-1 or type-2 eddy forcing, depending on which mode has the highest growth rate. At this point direction of the background flow is crucial, because the type-1/type-2 eddy forcing dominates in the EB/WB flow regime. This duality explains the absence/presence of the high-frequency oscillation in the EB/WB eddy forcings of the nonlinear solutions.

Important differences between the eigenmode eddy forcings in the EB and WB flows explain the following key aspects of the dynamics (Figs. 28 and 29). In the EB flow, the nonlinear baroclinic dynamics is such that the Reynolds and form stress forcings significantly balance each other, and the former maintains the jets. The linear eigenmode analysis not only confirms this general behavior but also provides more an insightful explanation. The Reynolds stress forcing contribution comes solely from the type-3 mode, whereas the other modes provide weak Reynolds stress forcings that are poorly correlated with the jets. The type-3 form stress forcing very efficiently resists the jets, but its effect is partially canceled by the type-1 and -2 form stress forcings. Thus, the baroclinic jets are explained by the collective jet-maintaining action of the Type-1 and -2 form stress forcing and the Type-3 Reynolds stress forcing; this action is resisted by the Type-3 form stres forcing. In other words, the eastward jets are more baroclinically unstable rather than “negatively viscous” (Starr

1968), but the baroclinic instability effect is substantially compensated by the jet-driving buoyancy fluxes in the westward jets.

In the WB flow, the nonlinear baroclinic dynamics is such that the form stress forcing maintains the jets, and the Reynolds stress forcing resists them. The eigenmode analysis suggests that the jet-resisting Reynolds stress forcing and the jet-maintaining form stress forcing is associated with the Type-1 and -2 eigenmodes. However, the forcings associated with the Type-3 eigenmode tend to partially compensate for these effects: the eastward jets are baroclinically unstable, whereas the counteracting "negative viscosity" effect is present but rather weak.

What is the mechanism that bounds growth of the jets and equilibrates the flow? Below, we demonstrate that this mechanism has a simple explanation in terms of the structural changes of the eigenmodes that are associated with transient situations when the jets are weaker or stronger than on the average. This equilibration mechanism is complimentary to some others, which are based on the weakly nonlinear triad interactions (Pedlosky 1975a,b) and on the nonlinear Lyapunov stability arguments (Shepherd 1988).

To find this, first, we defined a measure of strength of the multiple jets as the meridional average of zonally averaged zonal velocity, $\tilde{u}$:

$$\Sigma^{(i)}(t) \;=\; \frac{1}{L_y}\int_0^{L_y} |\tilde{u}^{(i)}(t,y)|\, dy\,, \tag{41}$$

where the superscript denotes the vertical mode. Then, we calculated PDFs of $\Sigma^{(i)}$ and found that the corresponding variances in the EB regime are about $\pm 2\%$ of the time-mean $\overline{\Sigma^{(i)}}$, and in the WB regime they are about $\pm 5\%$ and $\pm 9\%$ of $\overline{\Sigma^{(1)}}$ and $\overline{\Sigma^{(2)}}$, respectively. All PDFs are characterized by single-maximum bell-shaped curves (not shown). We also calculated time series, $\Upsilon^{(i)}(t)$, of correlation between instantaneous zonally averaged meridional profiles of the PV anomaly and the eddy forcing. We verified that $\Upsilon^{(i)}(t)$ is highly and positively correlated with $d\Sigma^{(i)}(t)/dt$, suggesting that the jets are amplified, when the eddy forcing has significant projection on them. We also diagnosed time series of the total eddy energy of the flow, by defining eddies as fluctuations around instantaneous zonally averaged flow. Then, we focused on the conditional states when flow is either weaker (i.e., weak state: $\Sigma < \overline{\Sigma}$) or stronger (i.e., strong state: $\Sigma > \overline{\Sigma}$) than the average. When instantaneous weak/strong flow is accelerated/decelerated, we refer to it as driven toward the average; if the opposite is true, then the flow is driven away from the average. In the EB regime, we find that when barotropic/baroclinic flow is driven toward the average, correlation of its eddy forcing with the jets changes by about 3%/20%: in the weak state eddy forcing is more efficient, and in the strong state it is less efficient. In the WB flow, the situation is similar and the corresponding correlation changes are about 5% and 35% for the barotropic and baroclinic flow components, respectively. At the same time, the corresponding change of the eddy energy is about 2%: the energy is larger in the weak state and smaller in the strong state. Relatively small change of the eddy energy suggests that equilibration is achieved mostly due to the change of the eddy forcing efficiency rather than of the eddy intensity.

The change of the eddy forcing efficiency is simply explained in terms of the meridionally localized linear eigenmodes (Table 5). Around the flow equilibrium, stronger jets result in more meridionally localized eddy forcing associated with the eigenmodes (Figs. 28 and 29), and such forcing becomes less correlated with the jets. The only exception is the baroclinic type-2 eddy forcing in the WB flow, but its effect is strongly overcome by contributions of the other eigenmodes.

To summarize, analysis of the multiple-jet linear eigenmodes yields insights into the kinematic and dynamic properties of the nonlinear dynamics. In particular, it explains the barrier/mixer patterns of the meridional material transport and the associated eddy PV fluxes, and it explains the relative roles of the momentum and buoyancy fluxes in maintaining the jets, and it explains the mechanism of the flow equilibration. Overall, the underlying linear eigenmodes can be viewed as descendants of the “noodles” that are distorted and partially localized on the jets.

5. Role of Meridional Boundaries

Multiple time-mean zonal jets in the ocean are latent, that is, masked by relatively energetic and isotropic mesoscale eddies (e.g., Huang et al. 2007), whereas the atmospheric jets are manifest, that is, dominant over the eddies. Here, we argue that the difference of patterns can be explained by the presence of meridional boundaries in the ocean, which remove the annular modes from the system, and that the underlying dynamics is rather similar. We test this hypothesis by replacing half of the channel with the square basin: the dynamical equations and the background flow remain intact, but there are additional no-flow boundary conditions on the meridional walls (i.e., the model becomes as in Berloff (2005), but with forcing in terms of the uniform background flow). To keep the analysis as simple as possible we consider a basin in which the basic flow is the same as in the previous section. That is, we allow the basic flow to enter the left hand boundary and leave the right hand boundary unaltered by the meridional walls. Those boundaries, however, are used to constrain the perturbations to that flow to satisfy zero normal velocity conditions on the meridional boundaries. This intermediate way station between a complete basin model and the fully reentrant channel keeps the basic problem simple but removes the annular modes as solutions of the perturbation problem. On the one hand, this model allows isolation of the basic effect of the meridional boundaries, but, on the other hand, its background flow remains ultimately simple and unchanged by these boundaries. To summarize what is discussed below, the main differences between the closed-basin and zonal-channel jets are due to absence of the annular modes and presence of the weakly damped basin modes (Berloff 2005).

For the closed-basin reference solutions we use the values of $U_1 = 6.5$ and -2.5 cm s^{-1} that yield the clearest multiple-jet patterns (Fig. 30). The jets — actually, zonally elongated recirculation cells

— are substantially weaker than those in the channel, despite the equally strong eddies. Also, the jets do not have the east-west asymmetry found in the channel. We argue that the above properties are due to the absence of the annular modes, which in the channel are excited by the secondary instability of the "noodles" and contribute to the jets. In the closed basin we couldn't find multiple flow equilibria, which in the channel are associated with particular combinations of the annular modes. For the same reason, the large-scale damping can be relaxed in the closed basin, because due to the absence of the annular modes there is no "merged-jets" regime (section 2.4). Finally, the tendency toward the "PV staircase" — already weak in the zonal channel — is barely manifested in the closed basin, because of the weak meridional localization of the "noodles" in the absence of the annular modes. All these properties are also characteristic of the GCM-simulated jets in the midlatitude North Atlantic (KBP08).

Another important aspect of the closed-basin dynamics in the WB flow is excitation of the weakly damped, large-scale, second baroclinic basin mode that coexists with the "noodles". Basin modes of this sort, though in the absence of the background flow, are discussed in Berloff (2005). The excited basin mode propagates to the west on the interannual time scale (i.e., basin-crossing time of the second baroclinic mode) and explains several features of the jets. First, in the middle of the basin the instantaneous jets are efficiently averaged out in the time-mean sense by the meridional fluctuations associated with the propagating large-scale mode. Second, in the time-mean baroclinic component of the flow, there are well-defined, large-scale, cyclonic and anticyclonic recirculations near the northern and southern basin boundaries, respectively. These recirculations are driven by the nonlinear self-interactions of the large-scale propagating mode (Berloff 2005). In the EB flow, the situation is different, because the corresponding mode has to propagate against the background flow — this shortens its zonal lengthscale and, thus, makes it more damped. Nevertheless, these modes manifest themselves as weak, meridionally coherent enhancements of the eddy amplitudes.

The zonal inhomogeneity of the jets is a robust feature of the WB flow regime: the jets are attached to the western boundary and extend over 3/4 and 1/2 of the basin, in the two- and three-layer models, respectively. A similar behavior is found in the comprehensive GCM (KBP08). This is so, because the growth rate of the secondary instability is comparable to the transit time of the westward propagating “noodles” (LaCasce and Pedlosky 2004), hence the jets develop over some distance from the eastern boundary.

We explored the empirical dependences of L_j on parameters of the problem and found general similarities with the channel (section 2.3). However, in the closed basin L_j is typically 20-30% shorter. This difference is due to the fact that, in the absence of the annular modes and subsequent localization, the closed-basin “noodles” are more pronounced, grow to larger amplitudes, and, hence, experience secondary instability with shorter lengthscale (section 4.5). We also find that the dynamical balances in the closed basin and zonal channel are qualitatively similar (section 3), but the eddy forcings as well as the barrier/mixer contrasts are much weaker in the basin, which is consistent with the latency of the jets.

6. Conclusions and Discussion

Multiple alternating zonal jets are studied in a hierarchy of idealized dynamical ocean models. This study is guided by the analysis of a comprehensive, eddy-resolving general circulation model of the North Atlantic (KBP08). First, we analyze fully nonlinear regimes, and then we explain formation of the jets with linear stability arguments. We look at the two main regimes, in which the eddies and the jets are maintained by either eastward or westward baroclinic shear. The main focus is on the flow in the zonal channel, although the closed-basin dynamics is also looked at.

The main conclusions are that (1) the underlying dynamical mechanism forming the jets is fundamentally non-local in space, (2) the linear stability arguments are useful even for the nonlinear regimes of interest, and (3) the jets have mixed barotropic-baroclinic dynamics and, therefore, can not be adequately represented by the barotropic and equivalent-barotropic models.

6.1 Summary

The main results of this study can be summarized as the following:

(1) The background flow is unstable to the primary-instability mode, which has the pattern of alternating *meridional* jets (i.e., "noodles");

(2) During spin up from the state of rest, the secondary instability of the primary-instability mode generates the initial multiple zonal jets;

(3) In the zonal channel, there are annular modes characterized by very weak decay rates;

(4) Eddy forcing of the secondary instability excites the annular modes that, on the one hand, are relatively large-scale (hence, are more resistant to dissipation) and, on the other hand, have significant projection on the eddy forcing itself;

(5) Weak large-scale damping keeps the solutions away from the drift into the regime dominated by the gravest annular mode;

(6) Equilibrium spectra of the excited annular modes are characterized by several peaks, which explain the shape of the zonal jets;

(7) Several multiple equilibria are found that differ by the number of the time-mean jets;

(8) As a result of meridional nonlocality of the underlying dynamics, Rhines scaling for meridional spacing of the jets is not confirmed;

(9) Growth of the annular modes, and, hence, emergence of the strong zonal jets, is associated with spatial localization of the "noodles" into 3 types of the meridionally localized eigenmodes, two of which are mostly trapped on the westward jets, and the third one is trapped on the eastward jets;

(10) Eddy forcings of the meridionally localized eigenmodes maintain either baroclinic or barotropic components of the jets, and act through the particular combination of the Reynolds and form stress eddy forcings;

(11) Fully nonlinear dynamics predicts that in the eastward-background flow baroclinic component of the jets is maintained by the Reynolds stress forcing and resisted by the form stress forcing, whereas in the westward-background flow the Reynolds stress forcing resists and the form stress forcing maintains the jets;

(12) It also predicts that in the eastward-background flow the baroclinic component of the jets is maintained by the barotropic-baroclinic interactions, whereas in the westward-background flow both barotropic-baroclinic and baroclinic-baroclinic interactions are important;

(13) The barotropic component of the jets is maintained by both barotropic-barotropic and baroclinic-baroclinic interactions;

(14) The nonlinear eddy/large-scale interactions are explained in terms of the eddy forcings associated with the meridionally localized eigenomdes;

(15) The mechanism that bounds growth of the multiple jets and equilibrates the flow is also explained in terms of the meridionally localized eigenomdes;

(16) Not only the first but also the second baroclinic mode is found to be important for maintaining the baroclinic component of the jets; the barotropic component of the jets is maintained mostly by the barotropic and first baroclinic modes;

(17) Some parts of the multiple jets, depending on the direction of the background flow and depth, act as either weak barriers to or weak mixers of the meridional material transport, thus causing eddy/large-scale interaction through divergence of potential-vorticity eddy fluxes;

(18) If the basin is closed by the meridional walls, the jets are latent; they are maintained by the

secondary instability of the "noodles", as there are no annular modes available that could significantly amplify the jets and localize the eddies.

6.2 Discussion

Results of this study have numerous connections to the existing literature on the atmospheric and oceanic multiple alternating zonal jets. Some of the most important connections are discussed in this section.

The atmospheric jets have been known for a long time, and atmosphere of the Jupiter is the finest example of them. The Earth is smaller than the Jupiter, and it is argued that only 2 eastward jets (one in each hemisphere), known as the midlatitude jetstreams, and trade winds in between them fit the planet. Whereas atmospheric jets are manifest, the oceanic jets are latent and, therefore, difficult to observe. Although some traces of the oceanic jets have been observed in the past, and near the equator several prominent jets have been thoroughly studied, only the last few years witnessed an avalanche of evidence coming from the satellite observations and extensive float measurements. Now, we know that, from the Antarctic shore to the Arctic Ocean, the jets exist almost everywhere. On the other hand, we know nothing about their vertical structure, low-frequency variability, and role in the global climate. Also, we poorly understand the underlying physical mechanisms that generate these jets. This study is a step toward this understanding.

Our confidence in the oceanic jet existence is boosted not only by the observational evidence, but also by the eddy-resolving solutions of the modern GCMs that, due to the increased spatial resolution, begin to simulate multiple jets and predict their vertical structure. A complete dynamical analysis of the corresponding GCM solutions is difficult but feasible in the future. Idealized dynamical models of various types and configurations have been predicting emergence of zonal jets since the pioneering work of Rhines (1975). The emergence of multiple alternating zonal jets is a universal nonlinear phenomenon that tends to occur when two key factors are combined: the flow is full of eddies, and there is meridional PV gradient in the background. Apart from the key factors, the underlying physical mechanisms remain unclear both for the atmospheric and oceanic jets. Different dynamical models may produce different jets for different dynamical reasons, and their relevance to the real world remains to be verified.

So far, the theoretical focus has been on barotropic dynamics, on unbounded periodic domains, on the inverse energy cascade driven by imposed small-scale forcing, and on a spectral description of the phenomenology. Other important aspects remain virtually unexplored: the role of the baroclinic modes; boundary effects including bottom topography and complex coastline; more physical representation of the forcing; co-existence of the inverse and forward energy cascades; the role of the coherent structures; the role of the large-scale geographical inhomogeneities; and low-frequency variability of the jets. At present, the main theoretical challenge is to sort out important and unimportant aspects, to identify potentially important physical mechanisms, and to move from the simplest models that isolate particular mechanisms to complex models that allow for competition between several mechanisms.

We focused on a fairly simple, multi-layer QG model configured in a zonal channel and driven by the imposed vertical shear. By using various analytical techniques, we understand the dynamical mechanisms that cause formation of the multiple alternating zonal jets in the model. In some regimes, the emergence of the multiple zonal jets from the eddies can be viewed as an example of "negative viscosity" phenomena (Phillips 1956; Starr 1968). In such phenomena large-scale flow patterns are maintained (rather than resisted) by the Reynolds stress forcing. In other regimes we find that the jets are maintained by the form stress forcing associated with divergence of the buoyancy eddy fluxes. For the jet formation, the most fundamental underlying process — built in the model — is eddy-driven down-gradient mixing of the background PV, which is maintained by the large-scale forcing. This mixing is controlled by the flow dynamics, and it is spatially inhomogeneous due to the coupling between the jets and the eddies. The central issue of our study is understanding how exactly the dynamics controls PV mixing and, thus, organizes the jets.

The meridional scaling of the jets is an important property that needs to be predicted. The Rhines scale comes from the balance between nonlinear advection and meridional advection of the planetary vorticity. It is commonly thought to be the lengthscale at which the inverse energy cascade, typical for the 2D turbulence, is "arrested" by propagating Rossby waves, so that the energy becomes directed into zonal jets. In this study we undermine this conjecture by arguing that the energy efficiently overcomes the "arrest" and rapidly propagates to the alternating meridional jets: "noodles". What happens to the energy absorbed by the "noodles", and what happens to the "noodles" themselves? In the absence or insufficiency of the selective large-scale dissipation, there is only one way to remove the absorbed energy and, thus, to achieve a statistical equilibrium. It is to cascade the energy forward from the "noodles" to the mesoscale instabilities and eddies, and then to the smaller scales affected by the energy dissipation. In principle, the equilibration could be achieved by the energy dissipation in the viscous boundary layers on the zonal walls, but in our model this mechanism is relatively inefficient. To summarize, our findings suggest that co-existence of the energy flux into the alternating meridional jets and the forward energy cascade is a fundamental aspect of the multiple zonal jet generation.

The mechanism of multiple jet formation operating in the model is fundamentally nonlocal. The background shear generates meridional "noodles" that emerge to finite amplitude and, then, undergo the secondary, transverse instability that sets meridional width of the jets. In the zonal channel, the secondary instability efficiently projects on the few annular modes that grow and contribute to the multiple jets. Emerging multiple jets feed back on the primary and secondary instabilities through the localization mechanism that reorganizes the "noodles" into 3 types of the unstable eigenmodes. Analysis of these eigenmodes and their nonlinear self-interactions yields significant insights into the flow dynamics and kinematics. In particular, it explains relative roles of the vertical modes, and of the Reynolds and form stress forcings in the barotropic and baroclinic dynamics. Also, we hypothesize that excessive meridional localization of instabilities provides bounding mechanism responsible for equilibration of the multiple jets. Despite many complicating physical factors neglected in the idealized model, the "noodles" solutions are remarkably similar to the meridional patterns seen in the observations and comprehensive GCMs (Huang et al. 2007; KBP08).

Our results imply that there is no simple and universal scaling for the meridional jet scale, L_j, because instabilities — that generate the jets — should depend on the vertical and horizontal structure of the background flow. On the other hand, we argue that L_j can be predicted by the linear stability analysis — this point of view is in the sharp contrast with the nonlinear inverse cascade arguments.

We connected our results to the "PV staircase" paradigm promoted in many studies (section 1.2) and found that description of the time-mean meridional PV in terms of the "staircase" is not accurate. The observed PV pattern — referred to as the "washboard" — is associated with weak alternating material-transport barriers and mixers. Locations of the barriers and mixers depend on direction of the background flow and depth, and the barriers are not necessarily located on the prograde jets. The time-mean flow does not approach PV staircase because of the strong barotropic mode predicted by the dynamics. These results are consistent with the companion analysis of the comprehensive, general circulation model (KBP08).

Observations and comprehensive GCMs (section 1.2) suggest that the multiple zonal jets have equally important barotropic and baroclinic components. A similar conclusion has been drawn by

Thompson and Young (2007). What is the minimal number of the vertical modes that have to be taken into account? Our results suggest that, for capturing the qualitative dynamics, the two-layer model is the minimal one, and, for more accurate quantitative predictions, the second baroclinic mode, and, perhaps, even higher modes have to be taken into account. We also find that accurate prediction of barotropic component of the jets from a purely barotropic model in which effects of the higher modes are approximated by the small-scale random forcing (e.g., as in a number of studies discussed in section 1.2) can be problematic. This is because the barotropic jets are largely driven by the baroclinic-mode Reynolds stress forcing. Correspondingly, prediction of the baroclinic component of the jets from the similarly forced equivalent-barotropic model is likely to be inaccurate due to the missing contribution of the barotropic eddies.

The following future developments of the results of this paper are anticipated. Calculation of the spectrum of the eigenmodes directly from the fully nonlinear solutions can provide further insight into the flow equilibration process as well as into the kinematics of mixing across and along the jets. Exploration of the larger Reynolds numbers corresponding to the lower values of eddy viscosity should shed some light on importance of the presently unresolved eddy scales. Spatial inhomogeneities of the background flow, deliberately neglected in this study, can impose their own lengthscales and, thus, alter the multiple jet pattern. In particular, nonzonality of the background flow can significantly boost generation of the eddies (Spall 2000), and horizontal shear can become a significant source of PV. Setting the background flow in terms of the double-gyre configuration would be an interesting step forward: it may account for regional inhomogeneity of the jet properties as well as observed deviations of jets from strict zonality. In the channel, we find multiple flow equilibria characterized by different jet spacing; an open question is whether transient forcing can induce low-frequency variability associated with transitions between these equilibria. The flow also possesses natural low-frequency variability associated with changes of the strength as well as with meridional displacements of the transient jets. It is likely that seasonal (Qiu et al. 2008) and decadal (Berloff et al. 2007) variabilities of the ocean modulate the jets, but the corresponding quantitative description of these processes is still missing. Dynamical connection of the midlatitude and equatorial zonal jets is another poorly understood aspect. Finally, the roles of the mild and steep bottom topographies in organizing the jets should be explored in the quasigeostrophic and primitive-equation models, respectively.

Acknowledgments:

Funding for PB was provided by NSF grants OCE 0344094 and OCE 0725796, and by the research grant from the Newton Trust of the University of Cambridge. Funding for IK was provided by NSF grants OCE 0346178 and 0749722. Funding for JP was provided by NSF grant OCE 0451086. PB is also grateful for stimulating discussions with Peter Haynes and Michael McIntyre.

Appendix A

Linear Stability Problem

We discuss formulation of the two-layer linear stability problem, and the analogous three-layer formulation is not shown for brevity.

In the situation with a uniform shear and the unbounded domain, given Fourier transform of the perturbation streamfunction,

$$\psi_i \;\longrightarrow\; \psi_i \exp[i(kx + ly - \omega t)]\,, \tag{A1}$$

the following linearized equations are obtained:

$$\begin{aligned}
\omega[-(k^2 + l^2 + S_1)\psi_1 + S_1\psi_2] \;=& \\
&\psi_1\left[-kU_1(k^2 + l^2) + k(\beta - S_1U_2) + i\nu(k^4 + 2k^2l^2 + l^4) + i\lambda_{11}\right] \\
&+\psi_2\left[kS_1U_1 + i\lambda_{12}\right],
\end{aligned} \tag{A2}$$

$$\begin{aligned}
&\omega[S_2\psi_1 - (k^2 + l^2 + S_2)\psi_2] \;= \\
&\quad \psi_1\left[kS_2U_2 + i\lambda_{21}\right] \\
&+\psi_2\left[-kU_2(k^2 + l^2) + k(\beta - S_2U_1) + i\nu(k^4 + 2k^2l^2 + l^4) + i\lambda_{22} + i\gamma(k^2 + l^2)\right].
\end{aligned} \tag{A3}$$

Nontrivial solutions of the above pair of the equations require that the determinant of the coefficients of ψ_i is zero. This statement yields the dispersion relationship between k, l, and ω.

In the zonal channel with either uniform or nonuniform shear, $U_i(y)$, given Fourier transform in the zonal direction,

$$\psi_i \;\longrightarrow\; \psi_i(y) \exp[i(kx - \omega t)]\,, \tag{A4}$$

the linearized equations are:

$$\omega[\psi_1'' - (k^2 + S_1)\psi_1 + S_1\psi_2] \;=$$

$$i\nu\psi_1^{IV} + [k(U_1 - i2\nu)]\psi_1'' + [k(\beta - k^2U_1 - U_1'' - S_1U_2) + i(\nu k^4 + \lambda_{11})]\psi_1$$

$$+[kS_1U_1 + i\lambda_{12}]\psi_2\,, \tag{A5}$$

$$\omega[\psi_2'' - (k^2 + S_2)\psi_2 + S_2\psi_1] \;=$$

$$i\nu\psi_2^{IV} + [k(U_2 - i2\nu) - i\gamma]\psi_2'' + [k(\beta - k^2U_2 - U_2'' - S_2U_1) + i(\nu k^4 + \lambda_{22} + \gamma k^2)]\psi_2$$

$$+[kS_2U_2 + i\lambda_{21}]\psi_1\,. \tag{A6}$$

The above equations are discretised with finite differences and solved numerically.

In the unbounded domain with a uniform zonal shear, U_i, and periodic meridional jets with finite amplitude, $V_i(x)$, we apply Fourier transform in the meridional direction:

$$\psi_i \;\longrightarrow\; \psi_i(x)\exp[i(ly - \omega t)]\,. \tag{A7}$$

We look for $\psi_i(x)$ that is periodic over the domain that includes 8 meridional jets.

References

Army, L., 1989: Hydraulic control of zonal currents on a β-plane. *J. Fluid Mech.*, **201**, 357–377.

Baldwin, M., P. Rhines, H.-P. Huang, and M. McIntyre, 2007: The jet-stream conundrum. *Science*, **315**, 467–468.

Balk, A., S. Nazarenko, and V. Zakharov, 1990: On the nonlocal turbulence of drift type waves. *Phys. Rev. Lett. A*, **146**, 217–221.

Berloff, P., A. Hogg, and W. Dewar, 2007b: The turbulent oscillator: A mechanism of low-frequency variability of the wind-driven ocean gyres. *J. Phys. Oceanogr.*, **37**, 2363–2386.

Berloff, P., 2005: On rectification of randomly forced flows. *J. Mar. Res.*, **63**, 497–527.

Berloff, P., J. McWilliams, and A. Bracco, 2002: Material transport in oceanic gyres. Part I: Phenomenology. *J. Phys. Oceanogr.*, **32**, 764–796.

Beron-Vera, F., M. Brown, M. Olascoaga, I. Rypina, H. Kocak, and I. Udovydchenkov, 2008: Zonal jets as transport barriers in planetary atmospheres. *J. Atmos. Sci.*, in press.

Chekhlov, A., S. Orszag, S. Sukoryansky, B. Galperin, and I. Staroselsky, 1996: The effect of small-scale forcing on large-scale structures in two-dimensional flows. *Physica D*, **98**, 321–334.

Cox, M., 1987: An eddy-resolving numerical model of the ventilated thermocline: Time dependence. *J. Phys. Oceanogr.*, **17**, 1044–1056.

Danilov, S., and D. Gurarie, 2004: Scaling, spectra and zonal jets in beta-plane turbulence. *Phys. Fluids*, **16**, 2592–2603.

Danilov, S., and V. Gryanik, 2004: Barotropic beta-plane turbulence in a regime with strong zonal jets revisited. *J. Atmos. Sci.*, **61**, 2283–2295.

Diamond, P., S.-I. Itoh, K. Itoh, T. Hahm, 2005: Zonal flows in plasma — a review. *Plasma Phys. Control. Fusion*, **47**, R35–R161.

Dritschel, D., and M. McIntyre, 2008: Multiple jets as PV staircases: The Phillips effect and the resilience of eddy-transport barriers. *J. Atmos. Sci.*, **65**, 855–874.

Esler, G., 2007: The turbulent equilibration of an unstable baroclinic jet. *J. Fluid Mech.*, **599**, 241–268.

Farrell, B., and P. Ioannou, 2007: Structure and spacing of jets in barotropic turbulence. *J. Atmos. Sci.*, **64**, 3652–3665.

Firing, E., 1987: Deep zonal currents in the central equatorial Pacific. *J. Mar. Res.*, **45**, 791–812.

Galperin, B., H. Nakano, H. Huang, and S. Sukoriansky, 2004: The ubiquitous zonal jets in the atmospheres of giant planets and Earth's oceans. *Geophys. Res. Lett.*, **31**, L13303.

Greenslade, M., and P. Haynes, 2008: Vertical transition in transport and mixing in baroclinic flows. *J. Atmos. Sci.*, in press.

Haidvogel, D. and I. Held, 1980: Homogeneous quasi-geostrophic turbulence driven by a uniform temperature gradient. *J. Atmos. Sci.*, **37**, 2644–2660.

Holland, W., 1978: The role of mesoscale eddies in the general circulation of the ocean — Numerical experiments using a wind-driven quasigeostrophic model. *J. Phys. Oceanogr.*, **8**, 363–392.

Haynes, P., D. Poet, and E. Shuckburgh, 2007: Transport and mixing in kinematic and dynamically-consistent flows. *J. Atmos. Sci.*, **64**, 3640–3651.

Haynes, P., and E. Shuckburgh, 2000: Effective diffusivity as a diagnostic of atmospheric transport. Part I: Stratosphere. *J. Geophys. Res.*, **105**, 22777–22794.

Herbei, R., I. McKeague, and K. Speer, 2008: Gyres and jets: Inversion of tracer data for ocean circulation structure. *J. Phys. Oceanogr.*, in press.

Hogg, N., and B. Owens, 1999: Direct measurement of the deep circulation within the Brazil basin. *Deep-Sea Res.*, **46**, 335–353.

Hua, B. L., M. D'Orgeville, M. Fruman, C. Menesguen, R. Schopp, P. Klein, and H. Sasaki, 2008: Destabilization of mixed Rossby-Gravity waves and equatorial zonal jets formation. *J. Fluid Mech.*, submitted.

Huang, H.-P., A. Kaplan, E. Curchitser, and N. Maximenko, 2007: The degree of anisotropy for mid-ocean currents from satellite observations and an eddy-permitting model simulation. *J. Geophys. Res.*, **112**, C09005.

Huang, H.-P., W. Robinson, 1998: Two-dimensional turbulence and persistent zonal jets in a global barotropic model. *J. Atmos. Sci.*, **55**, 611–632.

Ishioka, K., J. Hasegawa, and S. Yoden, 2007: Asymmetrization mechanism of jet profiles in decaying beta-plane turbulence. *J. Atmos. Sci.*, **64**, 3340–3353.

Juckes, M., and M. McIntyre, 1987: A high resolution, one-layer model of breaking planetary waves in the stratosphere. *Nature*, **328**, 590–596.

Kamenkovich, I., P. Berloff, and J. Pedlosky, 2008: On the structure and dynamics of the zonal jets in the North Atlantic. In preparation.

Kaspi, I., and G. Flierl, 2007: Formation of jets by baroclinic instability on gas planet atmospheres. *J. Atmos. Sci.*, **64**, 3177–3194.

Kondratyev, K., and G. Hunt, 1982: *Weather and Climate on Planets.* Oxford, Pergamon Press, 768 pp.

Kramer, W., M. van Buren, H. Clercx, and G. van Heijst, 2006: Beta-plane turbulence in a basin with no-slip boundaries. *Phys. Fluids*, **18**, 026603.

Krauss, W., and C. Boning, 1987: Lagrangian properties of eddy fields in the northern North Atlantic as deduced from satellite-tracked buoys. *J. Mar. Res.*, **45**, 259-291.

LaCasce, J., and J. Pedlosky, 2004: The instability of Rossby basin modes and the oceanic eddy field. *J. Phys. Oceanogr.*, **34**, 2027–2041.

Lapeyre, G., and I. Held, 2003: Diffusivity, kinetic energy dissipation, and closure theories for the poleward eddy heat flux. *J. Atmos. Sci.*, **60**, 2907–2916.

Lee, S., 1997: Maintenance of multiple jets in a baroclinic flow. *J. Atmos. Sci.*, **54**, 1726–1738.

Manfroi, A., and W. Young, 2002: Stability of β-plane Kolmogorov flow. *Physica D*, **162**, 208–232.

Manfroi, A., and W. Young, 1999: Slow evolution of zonal jets on the beta plane. *J. Atmos. Sci.*, **56**, 784–800.

Marshall, J., E. Shuckburgh, H. Jones, C. Hill, 2006: Estimates and implications of surface eddy diffusivity in the Southern Ocean derived from tracer transport. *J. Phys. Oceanogr.*, **36**, 1806–1821.

Maximenko, N., O. Melnichenko, P. Niiler, and H. Sasaki, 2008: Stationary mesoscale jet-like features in the ocean. *Geophys. Res. Lett.*, submitted.

Maximenko, N., B. Bang, and H. Sasaki, 2005: Observational evidence of alternating zonal jets in the world ocean. *Geophys. Res. Lett.*, **32**, L12607.

McIntyre, M., 1982: How well do we understand the dynamics of stratospheric warmings? *J. Meteor. Soc. Japan*, **60**, 37–65.

McWilliams, J., 2007: The nature and consequences of oceanic eddies. In *Eddy-resolving oceanic general circulation modeling*. Edited by H. Hasumi and M. Hecht, in preparation.

McWilliams, J., 2006: *Fundamentals of Geophysical Fluid Dynamics*. Cambridge University Press, 249pp.

McWilliams, J., 1977: A note on a consistent quasigeostrophic model in a multiply connected domain. *Dyn. Atmos. Oceans*, **1**, 427–441.

Nadiga, B., 2006: On zonal jets in oceans. *Geophys. Res. Lett.*, **33**, L10601.

Nakano, H., and H. Hasumi, 2005: A series of zonal jets embedded in the broad zonal flows in the Pacific obtained in eddy-permitting ocean general circulation models. *J. Phys. Oceanogr.*, **35**, 474–488.

Nowlin, W., and J. Klinck, 1986: The physics of the Antarctic Circumpolar Current. *Rev. Geophys.*, **24**, 469–491.

Ollitrault, M., M. Lankhorst, D. Fratantoni, and P. Richardson, 2006: Zonal intermediate currents in the equatorial Atlantic Ocean. *Geophys. Res. Lett.*, **33**, L05605.

Orsi, A., T. Whitworth, and W. Nowlin, 1995: On the meridional extent and fronts of the Antarctic Circumpolar Current. *Deep-Sea Res.*, **42**, 641–673.

Panetta, L., 1993: Zonal jets in wide baroclinically unstable regions: Persistence and scale selection. *J. Atmos. Sci.*, **50**, 2073–2106.

Pedlosky, J., 1987: *Geophysical Fluid Dynamics.* 2nd edn., Springer-Verlag, 710 pp.

Pedlosky, J., 1975a: On secondary baroclinic instability and the meridional scale of motion in the ocean. *J. Phys. Oceanogr.*, **5**, 603–607.

Pedlosky, J., 1975b: The amplitude of baroclinic wave triads and mesoscale motion in the ocean. *J. Phys. Oceanogr.*, **5**, 608–614.

Phillips, N., 1956: The general circulation of the atmosphere: A numerical experiment. *Quart. J. Roy. Met. Soc.*, **82**, 123–164.

Qiu, B., R. Scott, and S. Chen, 2008: Length scales of eddy generation and nonlinear evolution of the seasonally-modulated South Pacific subtropical countercurrent. *J. Phys. Oceanogr.*, submitted.

Read, P., Y. Yamazaki, S. Lewis, P. Williams, R. Wordsworth, K. Miki-Yamazaki, J. Sommeria, H. Didelle, and A. Fincham, 2007: Dynamics of convectively driven banded jets in the laboratory. *J. Atmos. Sci.*, **64**, 4031–4052.

Rhines, P. 1975: Waves and turbulence on a beta-plane. *J. Fluid Mech.*, **69**, 417–443.

Rhines, P., 1994: Jets. *Chaos*, **4**, 313–339.

Richards, K., N. Maximenko, F. Bryan, and H. Sasaki, 2006: Zonal jets in the Pacific ocean. *Geophys. Res. Lett.*, **33**, L03605.

Scott, R., and L. Polvani, 2007: Forced-dissipative shallow-water turbulence on the sphere and the atmospheric circulation of the giant planets. *J. Atmos. Sci.*, **64**, 3158–3176.

Shepherd, T., 1988: Nonlinear saturation of baroclinic instability. Part I: The two-layer model. *J. Atmos. Sci.*, **45**, 2014–2025.

Shuckburgh, E., and P. Haynes, 2003: Diagnosing transport and mixing using a tracer-based coordinate system. *Phys. Fluids*, **15**, 3342–3357.

Smith, K., 2004: A local model for planetary atmospheres forced by small-scale convection. *J. Atmos. Sci.*, **61**, 1420–1433.

Smith, K., G. Boccaletti, C. Henning, I. Marinov, C. Tam, I. Held, and G. Vallis, 2002: Turbulent diffusion in the geostrophic inverse cascade. *J. Fluid Mech.*, **469**, 13–48.

Sen, A., B. Arbic, R. Scott, C. Holland, E. Logan, and B. Qiu, 2006: Persistent small-scale features in maps of the anisotropy of ocean surface velocities implications for mixing? Eos Trans. AGU, **87**(52), Fall Meet. Suppl., Abstract OS13B-1553.

Sokolov, S., and S. Rintoul, 2007a: Multiple jets of the Antarctic Circumpolar Current south of Australia. *J. Phys. Oceanogr.*, **37**, 1394–1412.

Sokolov, S., and S. Rintoul, 2007b: On the relationship between fronts of the Antarctic Circumpolar Current and surface chlorophyll concentrations in the Southern Ocean. *J. Geophys. Res.*, **112**, C07030.

Sommeria, J., S. Meyers, and H. Swinney, 1989: Laboratory model of a planetary eastward jet. *Nature*, **337**, 58–61.

Spall, M., 2000: Generation of strong mesoscale eddies by weak ocean gyres. *J. Mar. Res.*, **58**, 97–116.

Starr, V., 1968: *Physics of negative viscosity phenomena.* McGraw-Hill, New York, 256 pp.

Sukoriansky, S., N. Dikovskaya, and B. Galperin, 2007: On the "arrest" of inverse energy cascade and the Rhines scale. *J. Atmos. Sci.*, **64**, 3312–3327.

Theiss, J., 2004: Equatorward energy cascade, critical latitude, and the predominance of cyclonic vortices in geostrophic turbulence. *J. Phys. Oceanogr.*, **34**, 1663–1678.

Thompson, A., and W. Young, 2007: Baroclinic eddy heat fluxes: zonal flows and energy balance. *J. Atmos. Sci.*, **64**, 3214–3231.

Treguier, A., N. Hogg, M. Maltrud, K. Speer, and V. Thierry, 2003: The origin of deep zonal flows in the Brazil basin. *J. Phys. Oceanogr.*, **33**, 580–599.

Treguier, A., and L. Panetta, 1994: Multiple zonal jets in a quasigeostrophic model of the Antarctic Circumpolar Current. *J. Phys. Oceanogr.*, **24**, 2263–2277.

Vallis, G., and M. Maltrud, 1993: Generation of mean flows and jets on a beta plane and over topography. *J. Phys. Oceanogr.*, **23**, 1346–1362.

Williams, G., 1978: Planetary circulations: 1. Barotropic representation of jovian and terrestrial turbulence. *J. Atmos. Sci.*, **35**, 1399–1426.

Figure Captions

Fig. 1. Multiple zonal jets simulated by a comprehensive, eddy-resolving GCM of the North Atlantic (taken from Kamenkovich et al. 2008). Shown is zonal velocity, averaged over 9 years, at 500 m depth (CI is 0.5 cm s^{-1}).

Fig. 2. Multiple-jet flow in the two-layer zonal channel. Instantaneous (a) barotropic and (b) baroclinic velocity streamfunctions in the eastward-flow regime with $U_1 = 6$ cm s^{-1} (CI=2 Sv). The corresponding time-mean zonal velocity profiles are shown in the right panels. Panels (c) and (d) show the same quantities as the upper panels but for the westward-flow regime with $U_1 = -3$ cm s^{-1} (CI=1 Sv). Straight lines indicate the background velocities. Latitude values are normalized by the width of the channel ($L_y = 1800$ km $= 72Rd_1$).

Fig. 3. Time-mean zonal velocity components in the broad channel. Upper row of panels shows the upper-ocean (thick line) and deep-ocean (thin line) velocity components. Lower row of panels shows the corresponding barotropic (thick line) and baroclinic (thin line) velocity components. Multiple eastward-flow solutions with either 10 or 9 eastward jets are shown in panels (a,d) and (b,e), respectively. These solutions are the broad-channel equivalents of the solution in Fig. 2a,b. Westward-flow solution, which is the broad-channel equivalent of the solution in Fig. 2c,d, is shown in panels (c,f). Straight lines indicate the background velocities. Latitude values are normalized by the width of the channel ($L_y = 3600$ km $= 144Rd_1$).

Fig. 4. Meridional structure of the time-mean PV. Upper/lower row of panels corresponds to the EB/WB flow from Fig. 3a/c. (a,c) The upper- (thick) and deep-ocean (thin curve) PV profiles; and (b,d) the corresponding PV gradients. The upper- and deep-ocean PV profiles are normalized by $L_y|\beta + S_1U_1|$ and $L_y|\beta - S_2U_1|$, respectively; hence, the corresponding background gradients (indicated by straight lines) are either +1 or -1, depending on the sign of the background PV gradient.

Fig. 5. Meridional material transport. Total, M_i^{tot}, and irreversible, M_i^{irrev}, material fluxes are shown with thick curve and thick curve with filled circles, respectively. Both fluxes are normalized by the maximum value of the corresponding total flux. The corresponding profiles of the time-mean PV (thin) and zonal velocity (dashed curve) anomalies are shown for convenience, with arbitrary amplitudes. (a) Upper- and (b) deep-ocean material fluxes for the reference EB flow solution. The lower row of panels corresponds to the WB regime; since the background flow is negative, the corresponding material fluxes are multiplied by -1, for convenience.

Fig. 6. Zonal velocity profiles corresponding to the ideal PV staircases. These velocities are in sharp contrast to velocities of the actual solutions of the flow dynamics (Figs. 2 and 3). Isopycnal-layer velocities of the (a) eastward- and (b) westward-background reference solutions. Upper- and deep-ocean velocity profiles are normalized by their peak values and shown with thick and thin curves, respectively.

Fig. 7. Fourier power spectrum of the time-mean, zonal barotropic velocity shown in Fig. 3d. Velocity was normalized by its maximum value before calculating the spectrum. Straight vertical line corresponds to L_j.

Fig. 8. Dependence of the meridional jet scaling, L_j, on the background flow velocity. (a) Ratio of L_j to the channel width, and (b) ratio of L_j to the Rhines scale, L_r. Multiple solution branches are connected with continuous curves; straight lines in (b) indicate linear best-square fits.

Fig. 9. Dependence of the meridional jet scaling, L_j, on the planetary vorticity gradient, β. (a) Ratio of L_j to the channel width is shown for EB (thick) and WB (thin curve) flow solutions. Panel (b) shows ratio of L_j to Rhines scale, L_r, for the same set of solutions.

Fig. 10. Dependence of the meridional jet scaling, L_j, on the (a) bottom friction, γ, and (b) lateral eddy viscosity, ν. Individual dots are connected with curves, except when straight line is least-square

fitted in (b): thick and thin curves correspond to the EB and WB flow solutions, respectively.

Fig. 11. Time-mean zonal velocities of the three-layer channel model. Isopycnal-layer velocities corresponding to the (a) eastward- and (b) westward-background reference solutions are shown in the upper- (thick), middle- (dashed thick), and deep-ocean layers (thin curve). The lower row of panels shows the corresponding barotropic (thick), first baroclinic (dashed thick), and second baroclinic (thin curve) velocities. Vertical lines indicate the corresponding background flow velocities.

Fig. 12. Single-jet flow regime. Instantaneous (a) barotropic and (b) baroclinic velocity streamfunctions in the EB flow regime with $U_1 = 6$ cm s^{-1} ((a) CI=4 Sv, (b) CI=1 Sv). The corresponding time-mean zonal velocity profiles are shown in the right panels with thick curves (such profiles for the alternative multiple solution are shown with thin curves).

Fig. 13. Time-mean meridional eddy fluxes of PV and its components in the reference EB solution. The upper row of panels describes fluxes of (a) PV, (b) relative vorticity, and (c) buoyancy in the upper ocean. The lower row of panels describes the same quantities but for the deep ocean. In each panel, the flux (thick curve) is normalized by the maximum value of the corresponding full PV flux. The corresponding profiles of the time-mean PV and its components are shown with thin curves, and the profiles of the time-mean zonal velocity are shown with dashed curves only on the left panels (both of these quantities have arbitrary units).

Fig. 14. The same as Fig. 13, but for the reference WB solution.

Fig. 15. Barotropic eddy forcing and its components. (a) Barotropic-barotropic (continuous) and baroclinic-baroclinic (dashed curve) eddy forcing components of the reference, three-layer EB flow solution. (b) Full eddy forcing (thin) is shown along with the time-mean barotropic PV component (thick curve). The eddy forcing itself and its components are normalized by the maximum value of the eddy forcing; the barotropic PV is shown with arbitrary units.

Fig. 16. Baroclinic eddy forcing and its components. (a) Barotropic-baroclinic (thin) and baroclinic-baroclinic (dashed curve), (b) relative-vorticity (thin) and buoyancy (dashed curve) eddy forcing components of the reference, three-layer EB flow solution. (c) Full eddy forcing (thin) is shown along with the time-mean baroclinic PV component (thick curve). The eddy forcing itself and its components are normalized by the maximum value of the eddy forcing; the baroclinic PV is shown with arbitrary units. The lower row of panels shows the same quantities, but for the WB flow solution.

Fig. 17. Properties of the most unstable eigenmode (i.e., “noodles”) growing on the uniform zonal flow in the unbounded domain: dependence on the planetary vorticity gradient, β. (a) Zonal period, (b) time period, and (c) growth rate as functions of the upper-ocean background velocity. On each panel, thick curve corresponds to the reference values of $\nu = 100$ m^2 s^{-1}, $\gamma = 0$ s^{-1}, and $\beta = 2 \times 10^{-11}$ m^{-1} s^{-1}. There are three values of β considered: 0.5, 2, and 4×10^{-11} m^{-1} s^{-1} (curves corresponding to the lowest value are labeled by “0.5”).

Fig. 18. Dispersion relationship of the linear stability problem: uniform zonal flow in the unbounded domain. The upper row of panels shows (a) growth rate and (b) eigenfrequency of the reference EB flow as functions of the zonal (k) and meridional (l) wavenumbers. The lower row of panels shows the same values but for the reference WB flow. Contour intervals: (a) and (c) CI=0.1 years^{-1}; (b) CI=0.04 and 1.0 years^{-1} for the small and large eigenfrequencies, respectively; and (d) CI=0.5 years^{-1}. Positive/negative contours in the right panels correspond to the phase lines propagating to the east/west.

Fig. 19. Annular eigenmodes. (a) Upper-ocean zonal velocity profiles of the second (dashed), third (thin), and eighth annular eigenmodes (thick curve), and (b) decay rates of the first 20 annular eigenmodes, ranked according to the increasing decay rate. The eigenmodes are calculated for the

reference control parameters. Zonal velocities in (a) are normalized by their maximum absolute values. Filled/empty circles in (b) indicate predominantly baroclinic/barotropic eigenmodes.

Fig. 20. Evidence of the annular modes in the multiple-jet flow. (a) Normalized spectrum of the annular modes, $P_{ann}(n)$, where n is mode index, calculated for the time-mean flow shown in Fig. 3d. Predominantly baroclinic/barotropic modes are indicated with the filled/empty circles. Contributions of the leading (b) two barotropic and (c) one baroclinic annular modes (indicated by the large circles in panel (a)) to the jets are shown with thick curves, and the corresponding barotropic and baroclinic zonal velocity profiles are shown with thin curves.

Fig. 21. Spin up of the multiple jets. Instantaneous upper-ocean streamfunction is obtained (a) after 2 years of the model integration starting from small random perturbations, (b) 200 days later, and (c) another 200 days later (CI are (a) 0.4 Sv and (b,c) 5 Sv). The basin is twice as large in each dimension as the one used for the EB flow reference solution (compare with Fig. 2a,b), but all other parameters are the same. Panel to the right of each streamfunction field shows the corresponding zonally averaged zonal velocity, and panel below the streamfunction field shows meridionally averaged meridional velocity.

Fig. 22. Critical eigenmodes of the finite-amplitude "noodles". Left/right column of panels corresponds to the EB/WB reference solution. (a,e) Meridional velocity of the background "noodles" in the upper- (thick) and deep-ocean (thin curve) isopycnal layers. (b,f) Upper-ocean velocity streamfunction (arbitrary amplitude). (c,g) Amplitude (normalized by its upper-ocean maximum value) and (d,h) phase of the zonal component of the critical eigenmode.

Fig. 23. Stability properties of the finite-amplitude "noodles". (a) Meridional period and (b) growth rate of the critical eigenmodes of the EB and WB reference solutions. Positive/negative values of the maximum upper-ocean meridional velocity, V_1, indicate EB/WB flows. Thin horizontal

lines in (b) indicate growth rates of the infinitesimal “noodles”.

Fig. 24. Localization of the “noodles” on the multiple jets. Amplitudes of the eigenmodes of (a) Type-1, (b) Type-2, and (c) Type-3 are shown for amplitude of the background jets, A_u, equal to 0.2 (thin), 0.5 (thin with filled circles), and 1.5 (thick curve). On panel (c), three isolated peaks corresponding to A_u=1.5 (thick curve) belong to three separate Type-3 eigenmodes trapped by the corresponding eastward jets (two more eigenmodes of this sort, trapped on the near-boundary eastward jets are not shown). Dashed curves in the panel (a) indicate the background and time-mean zonal velocities in the upper ocean (arbitrary units).

Fig. 25. Stability properties of the multiple zonal jets. Dependence on the jets amplitude, A_u, eddy viscosity, ν, and bottom friction, γ, is explored. Left/right half of each panel corresponds to the WB/EB flow reference parameters. Upper panels show dependence on A_u of (a) zonal and (b) time periods of the critical eigenmode, for $\nu = 50, 100, 200$ and 400 m^2 s^{-1}. Left/right half of each panel corresponds to the WB/EB flow reference parameters. Amplitudes corresponding to the WB flow reference solution are indicated as $-A_u$, and amplitudes equal to the minus and plus unity correspond to the actual time-mean jets from the WB and EB flow reference solutions, respectively. Lower panels show the same properties but for $\gamma = 0, 2$, and 4 $\times 10^{-7}$ s^{-1}. Functions corresponding to the reference values of $\nu = 100$ m^2 s^{-1} and $\gamma = 0$ are shown with thick curves, and, for clarity, some curves are marked with the corresponding values of ν and γ.

Fig. 26. Unstable eigenmodes of the EB flow with multiple zonal jets. Eigenmodes shown have indices (a) 1, (b) 2, (c) 8, and (d) 9, ordered in terms of the increasing decay rates. Contour plots show velocity streamfunctions of the eigenmode patterns in the 1/4-period section of the channel. Since the eigenmodes are either symmetric or antisymmetric with respect to the middle latitude of the channel, the upper-ocean pattern is shown in the northern half of the plot and the deep-ocean

one — in the southern half. All of the eigenmodes are normalized by the energy norm, and the (arbitrary) contour interval is the same throughout the figure. Sub-panels to the right of the contour plots show corresponding amplitudes of the upper- (thick continuous) and deep-ocean (thick dashed curve) components of the eigenmodes; the curves are normalized by the upper-ocean maximum amplitude. In each panel, thin curve with straight line in the middle show the time-mean zonal velocity profile of the jets (with arbitrary units).

Fig. 27. The same as Fig. 26, but for the WB flow. The eigenmodes shown have indices (a) 1, (b) 2, (c) 3, and (d) 7.

Fig. 28 Eddy forcing of the meridionally localized eigenmodes and its components: EB flow. Upper row of panels corresponds to the barotropic eddy forcing of the gravest eigenmodes localized in the center of the channel: (a) Type-1, (b) Type-2, and (c) Type-3 eigenmodes. Upper row of panels: Full eddy forcing (thick), as well as its barotropic-barotropic (thin) and baroclinic-baroclinic (thin with filled circles) components are shown. Lower row of panels: Full eddy forcing (thick), as well as its Reynolds stress (thin) and form stress (thin with filled circles) forcing components are shown. The corresponding time-mean PV anomalies are shown with dashed curve (arbitrary value). Each eddy forcing curve is normalized by the maximum absolute value of the eddy forcing corresponding to the gravest eigenmode.

Fig. 29 The same as Fig. 28, but for the WB flow.

Fig. 30. Multiple-jet flow in the two-layer closed basin. Instantaneous (a) barotropic and (b) baroclinic velocity streamfunctions in the eastward-flow regime with $U_1 = 6.5$ cm s^{-1} (CI=2.5 Sv). The corresponding time-mean zonal velocity profiles are shown in the right panels. Panels (c) and (d) show the same quantities as the left panels but for the westward-flow regime with $U_1 = -2.5$ cm s^{-1} (CI=1 Sv).

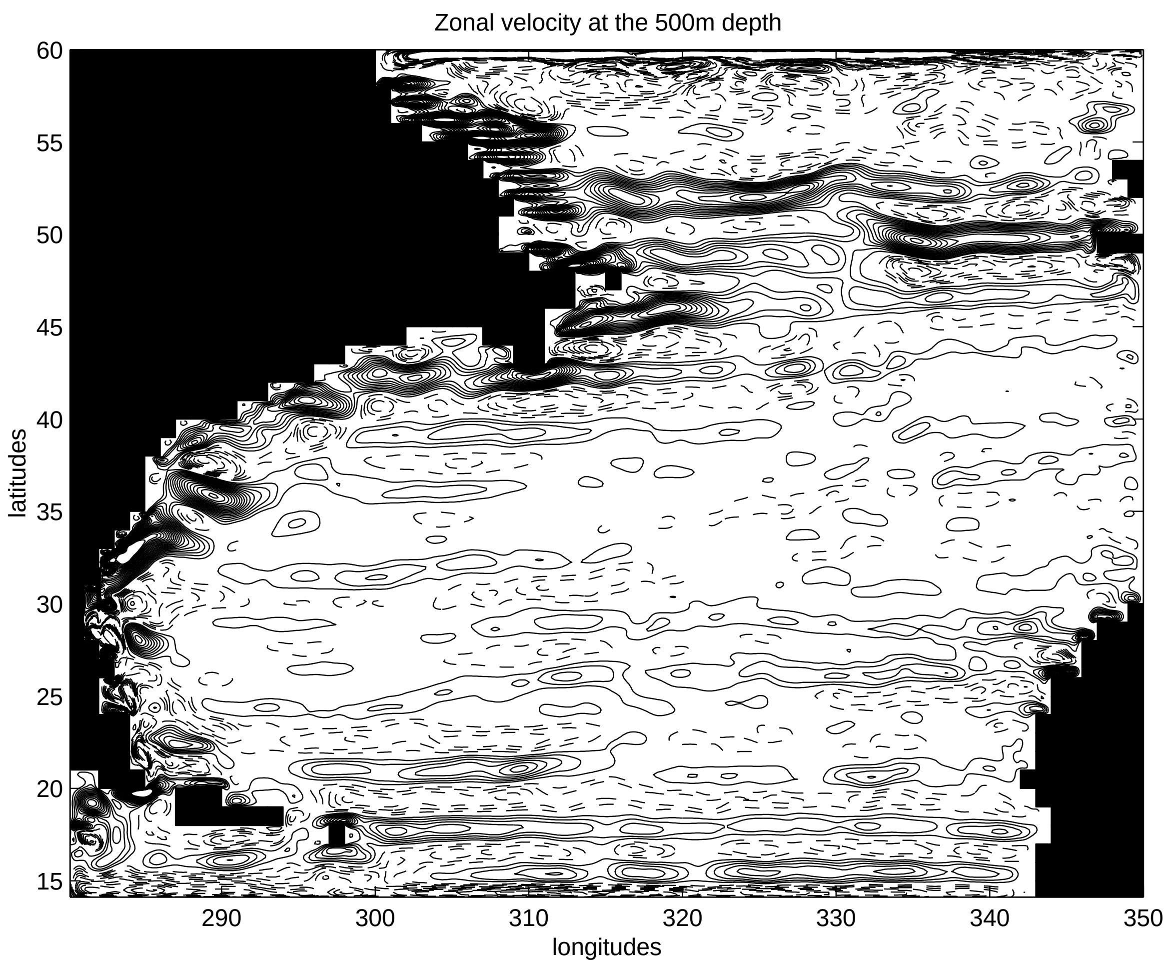

Figure 1: Multiple zonal jets simulated by a comprehensive, eddy-resolving GCM of the North Atlantic (taken from Kamenkovich et al. 2008). Shown is zonal velocity, averaged over 9 years, at 500 m depth (CI is 0.5 cm s^{-1}).

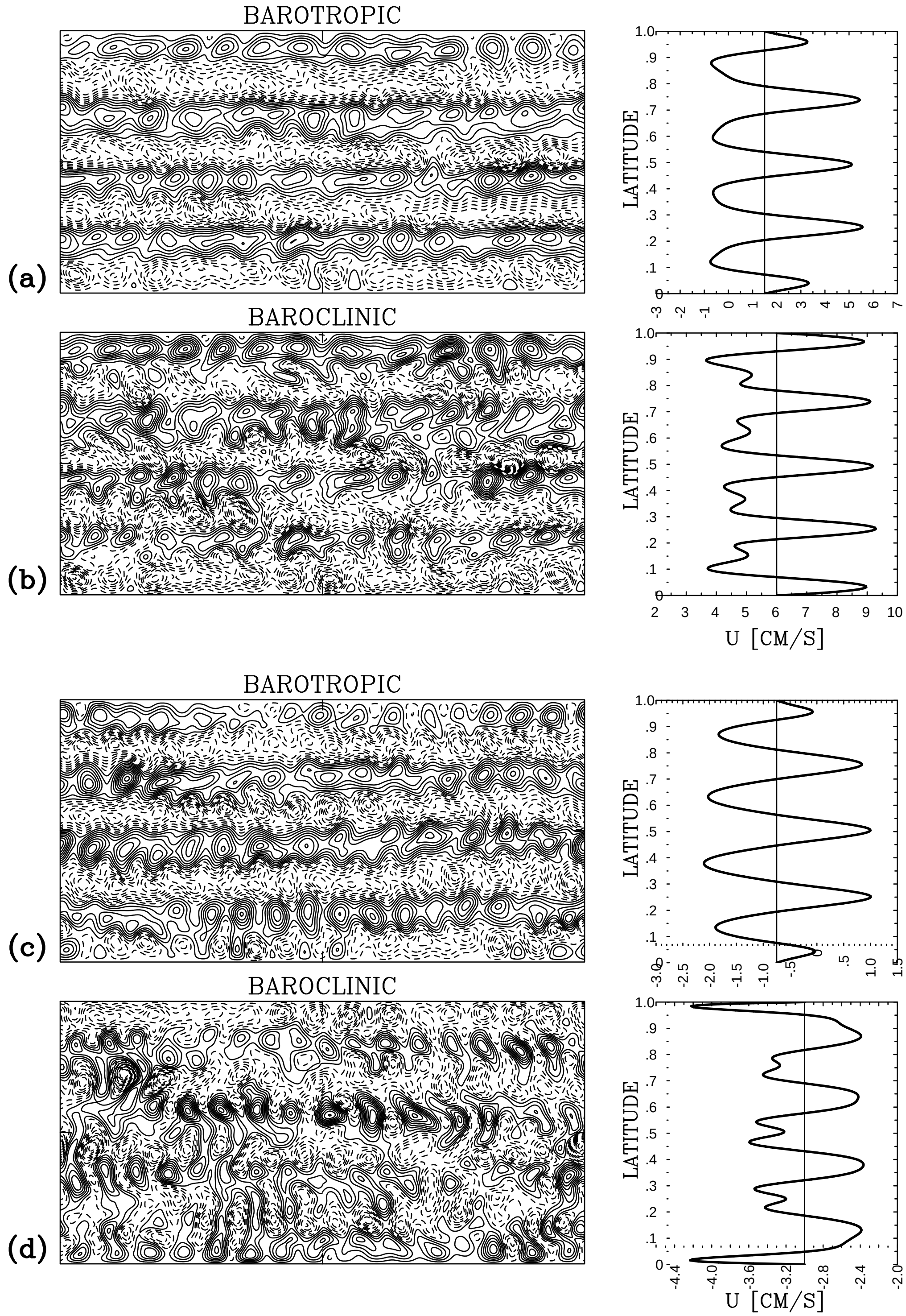

Figure 2: Multiple-jet flow in the two-layer zonal channel. Instantaneous (a) barotropic and (b) baroclinic velocity streamfunctions in the eastward-flow regime with $U_1 = 6$ cm s^{-1} (CI=2 Sv). The corresponding time-mean zonal velocity profiles are shown in the right panels. Panels (c) and (d) show the same quantities as the upper panels but for the westward-flow regime with $U_1 = -3$ cm s^{-1} (CI=1 Sv). Straight lines indicate the background velocities. Latitude values are normalized by the width of the channel ($L_y = 1800\,\text{km} = 72 Rd_1$).

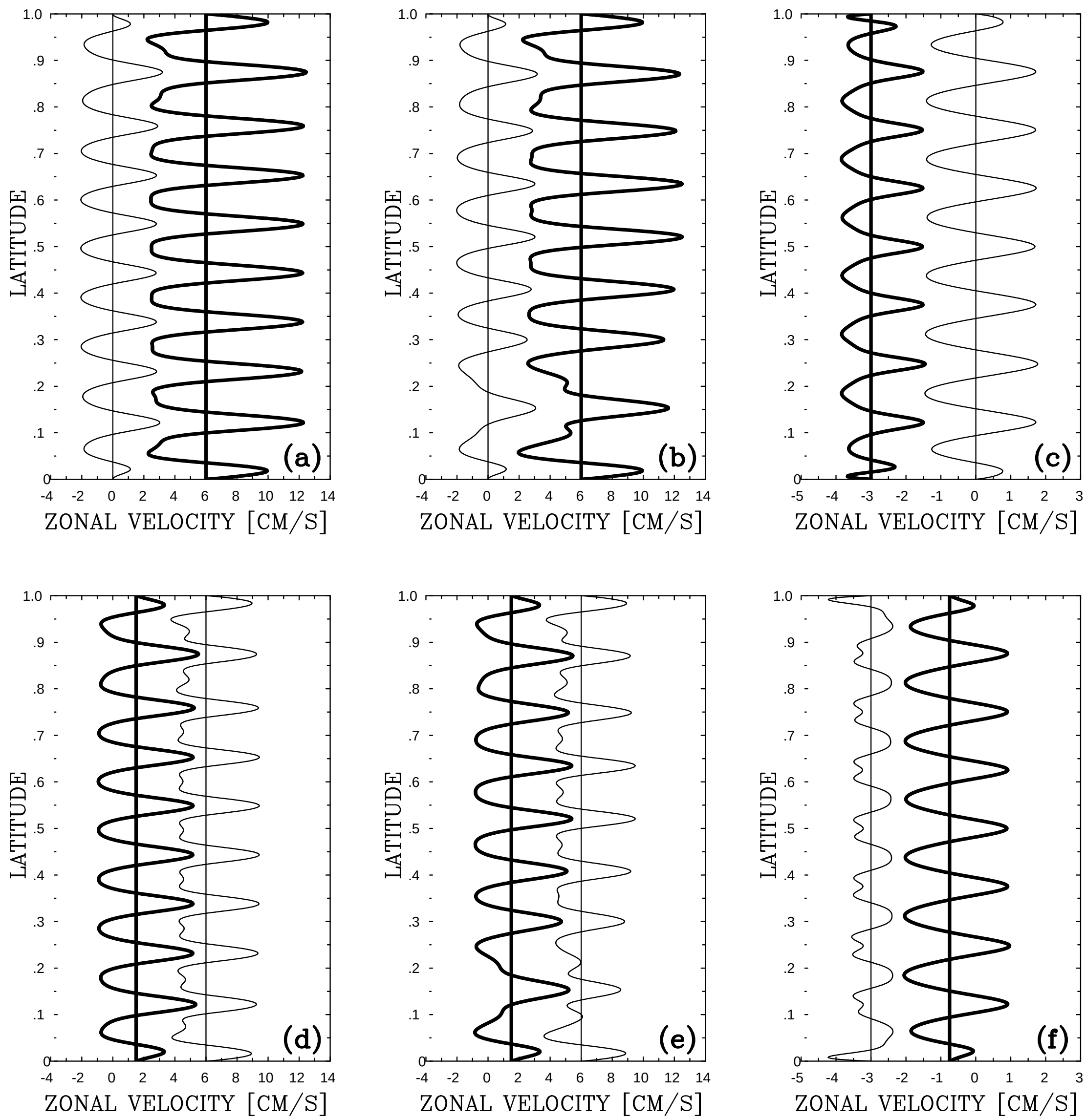

Figure 3: Time-mean zonal velocity components in the broad channel. Upper row of panels shows the upper-ocean (thick line) and deep-ocean (thin line) velocity components. Lower row of panels shows the corresponding barotropic (thick line) and baroclinic (thin line) velocity components. Multiple eastward-flow solutions with either 10 or 9 eastward jets are shown in panels (a,d) and (b,e), respectively. These solutions are the broad-channel equivalents of the solution in Fig. 2a,b. Westward-flow solution, which is the broad-channel equivalent of the solution in Fig. 2c,d, is shown in panels (c,f). Straight lines indicate the background velocities. Latitude values are normalized by the width of the channel ($L_y = 3600$ km $= 144Rd_1$).

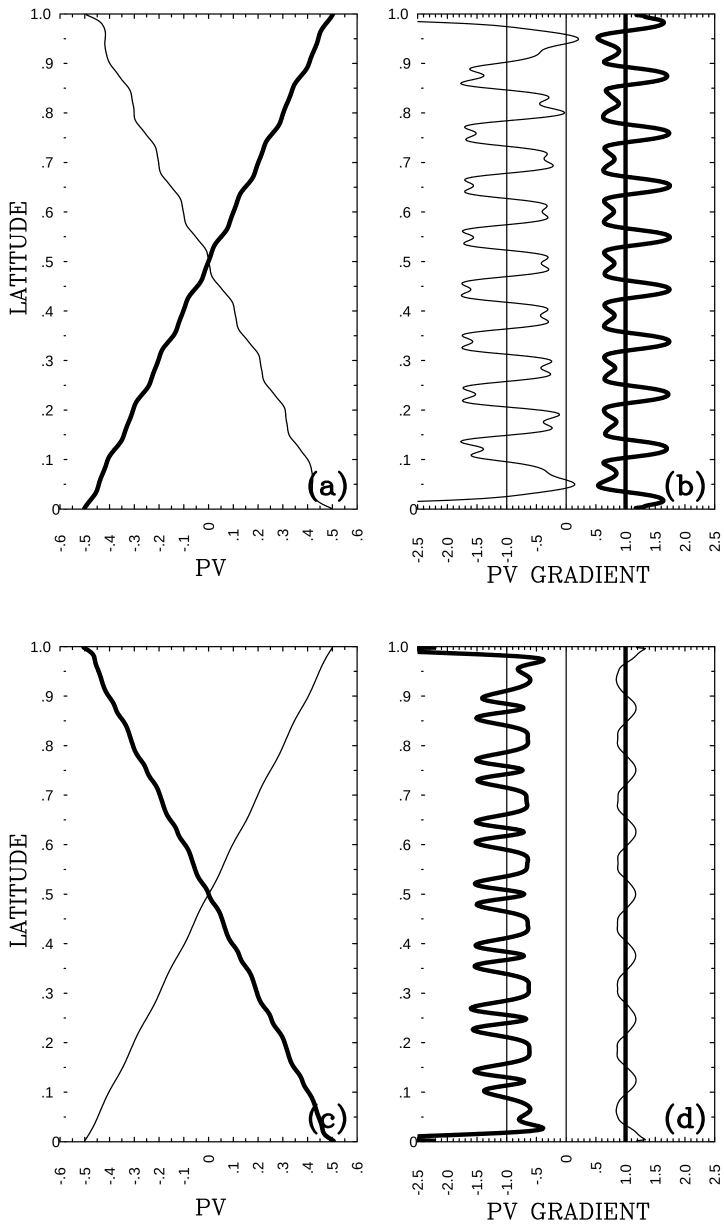

Figure 4: Meridional structure of the time-mean PV. Upper/lower row of panels corresponds to the EB/WB flow from Fig. 3a/c. (a,c) The upper- (thick) and deep-ocean (thin curve) PV profiles; and (b,d) the corresponding PV gradients. The upper- and deep-ocean PV profiles are normalized by $L_y|\beta + S_1U_1|$ and $L_y|\beta - S_2U_1|$, respectively; hence, the corresponding background gradients (indicated by straight lines) are either +1 or -1, depending on the sign of the background PV gradient.

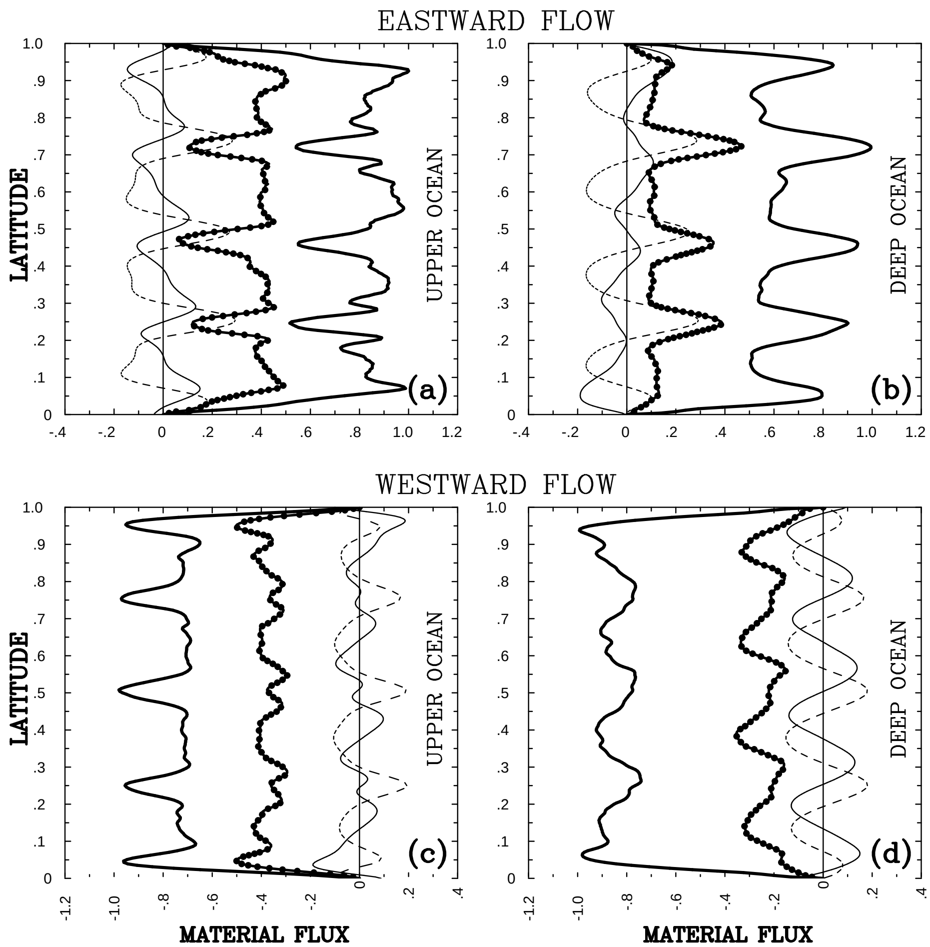

Figure 5: Meridional material transport. Total, M_i^{tot}, and irreversible, M_i^{irrev}, material fluxes are shown with thick curve and thick curve with filled circles, respectively. Both fluxes are normalized by the maximum value of the corresponding total flux. The corresponding profiles of the time-mean PV (thin) and zonal velocity (dashed curve) anomalies are shown for convenience, with arbitrary amplitudes. (a) Upper- and (b) deep-ocean material fluxes for the reference EB flow solution. The lower row of panels corresponds to the WB regime; since the background flow is negative, the corresponding material fluxes are multiplied by -1, for convenience.

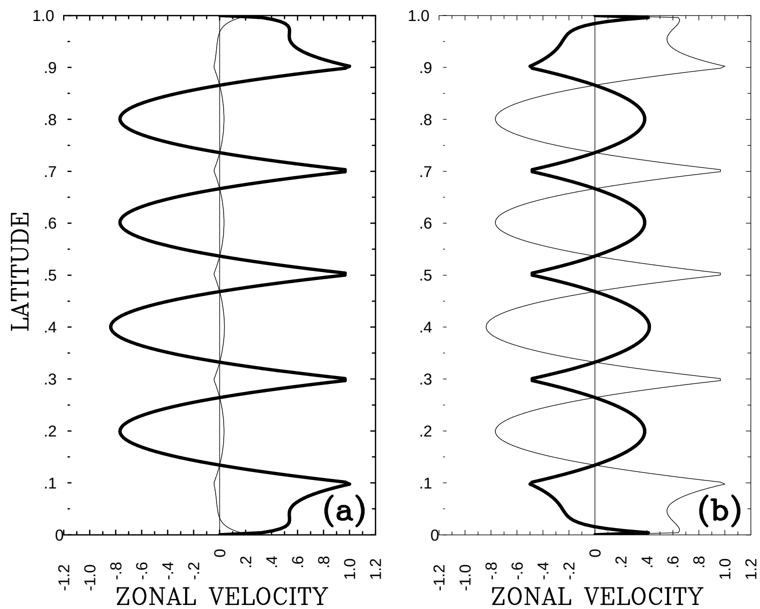

Figure 6: Zonal velocity profiles corresponding to the ideal PV staircases. These velocities are in sharp contrast to velocities of the actual solutions of the flow dynamics (Figs. 2 and 3). Isopycnal-layer velocities of the (a) eastward- and (b) westward-background reference solutions. Upper- and deep-ocean velocity profiles are normalized by their peak values and shown with thick and thin curves, respectively.

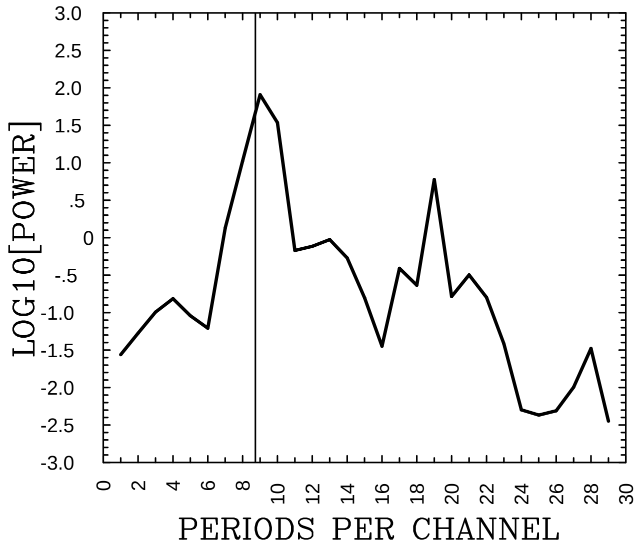

Figure 7: Fourier power spectrum of the time-mean, zonal barotropic velocity shown in Fig. 3d. Velocity was normalized by its maximum value before calculating the spectrum. Straight vertical line corresponds to L_j.

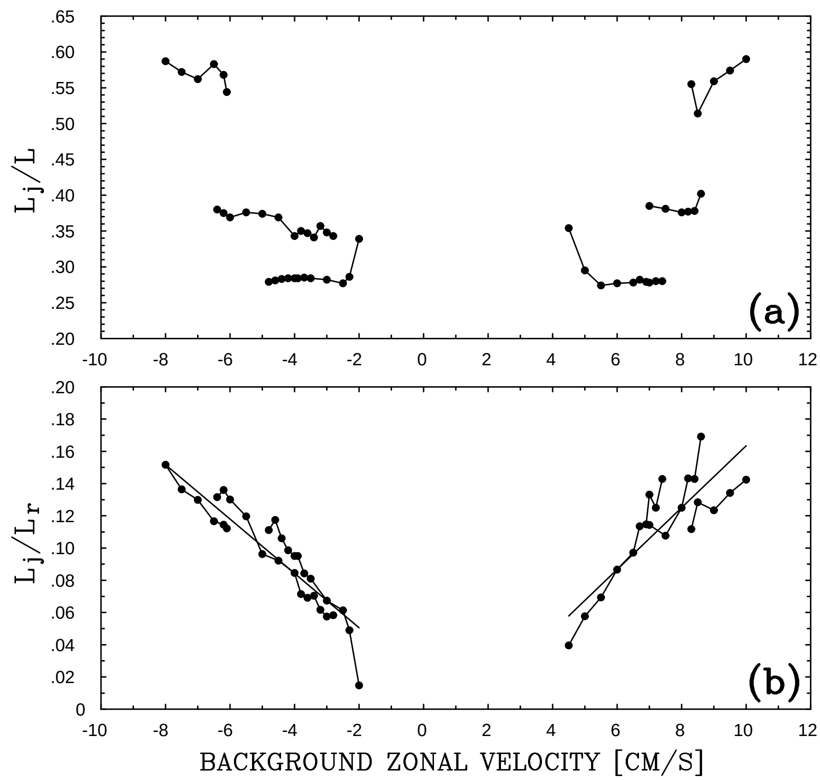

Figure 8: Dependence of the meridional jet scaling, L_j, on the background flow velocity. (a) Ratio of L_j to the channel width, and (b) ratio of L_j to the Rhines scale, L_r. Multiple solution branches are connected with continuous curves; straight lines in (b) indicate linear best-square fits.

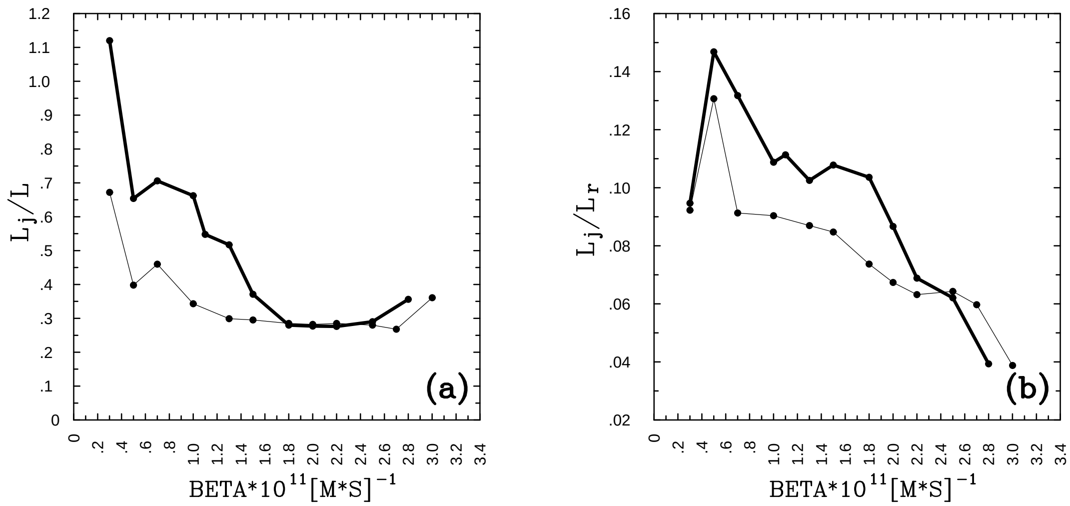

Figure 9: Dependence of the meridional jet scaling, L_j, on the planetary vorticity gradient, β. (a) Ratio of L_j to the channel width is shown for EB (thick) and WB (thin curve) flow solutions. Panel (b) shows ratio of L_j to Rhines scale, L_r, for the same set of solutions.

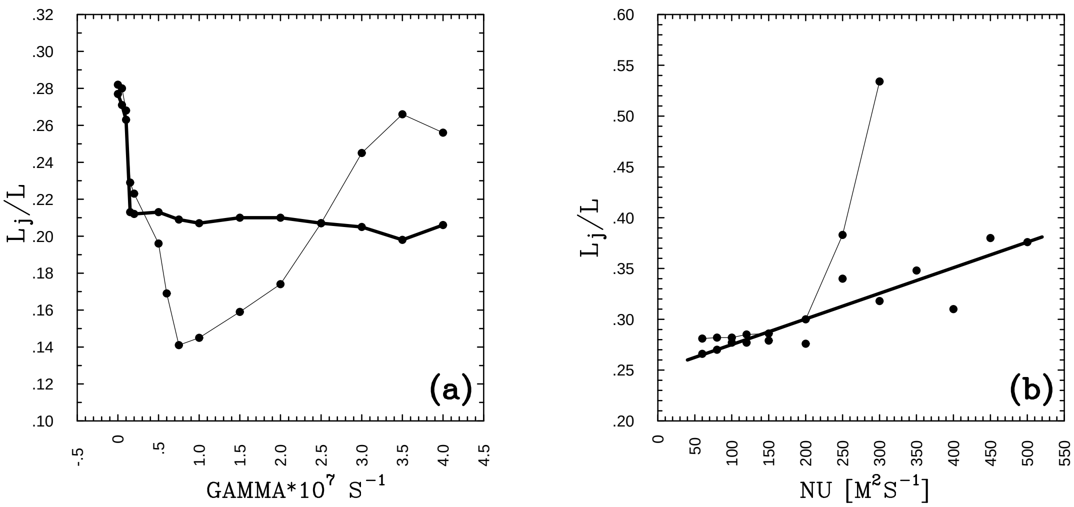

Figure 10: Dependence of the meridional jet scaling, L_j, on the (a) bottom friction, γ, and (b) lateral eddy viscosity, ν. Individual dots are connected with curves, except when straight line is least-square fitted in (b): thick and thin curves correspond to the EB and WB flow solutions, respectively.

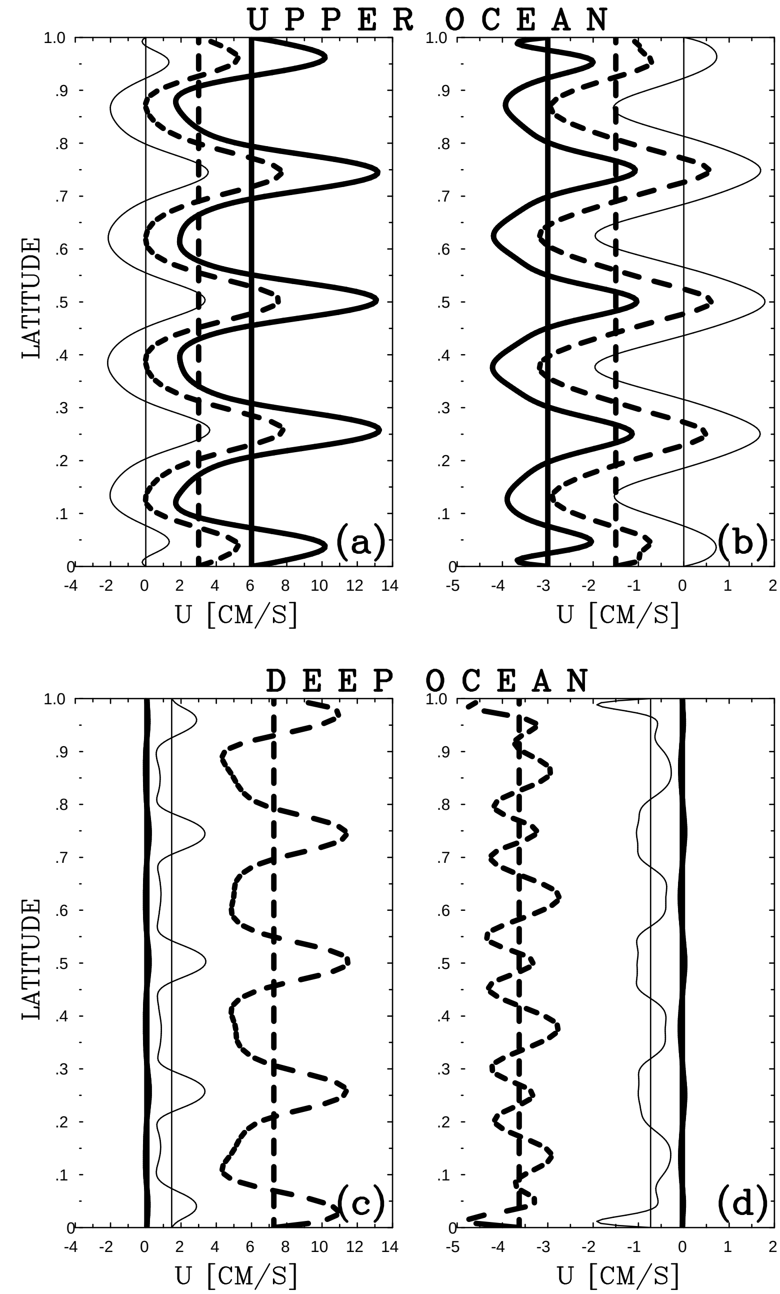

Figure 11: Time-mean zonal velocities of the three-layer channel model. Isopycnal-layer velocities corresponding to the (a) eastward- and (b) westward-background reference solutions are shown in the upper- (thick), middle- (dashed thick), and deep-ocean layers (thin curve). The lower row of panels shows the corresponding barotropic (thick), first baroclinic (dashed thick), and second baroclinic (thin curve) velocities. Vertical lines indicate the corresponding background flow velocities.

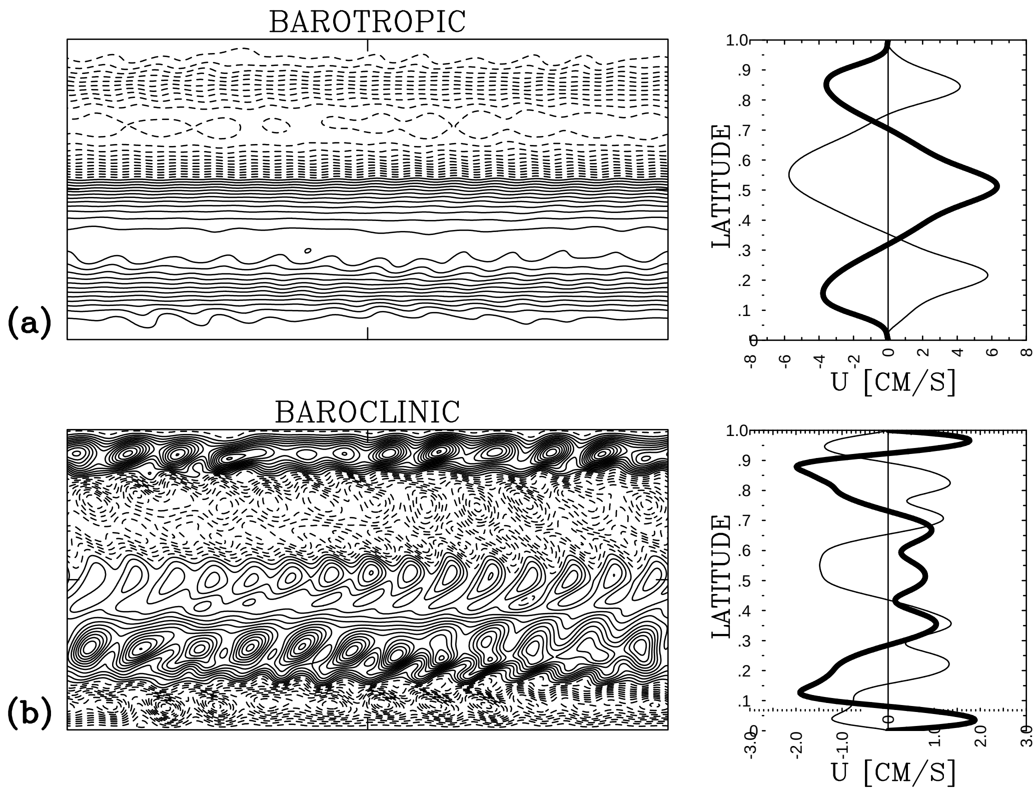

Figure 12: Single-jet flow regime. Instantaneous (a) barotropic and (b) baroclinic velocity streamfunctions in the EB flow regime with $U_1 = 6$ cm s^{-1} ((a) CI=4 Sv, (b) CI=1 Sv). The corresponding time-mean zonal velocity profiles are shown in the right panels with thick curves (such profiles for the alternative multiple solution are shown with thin curves).

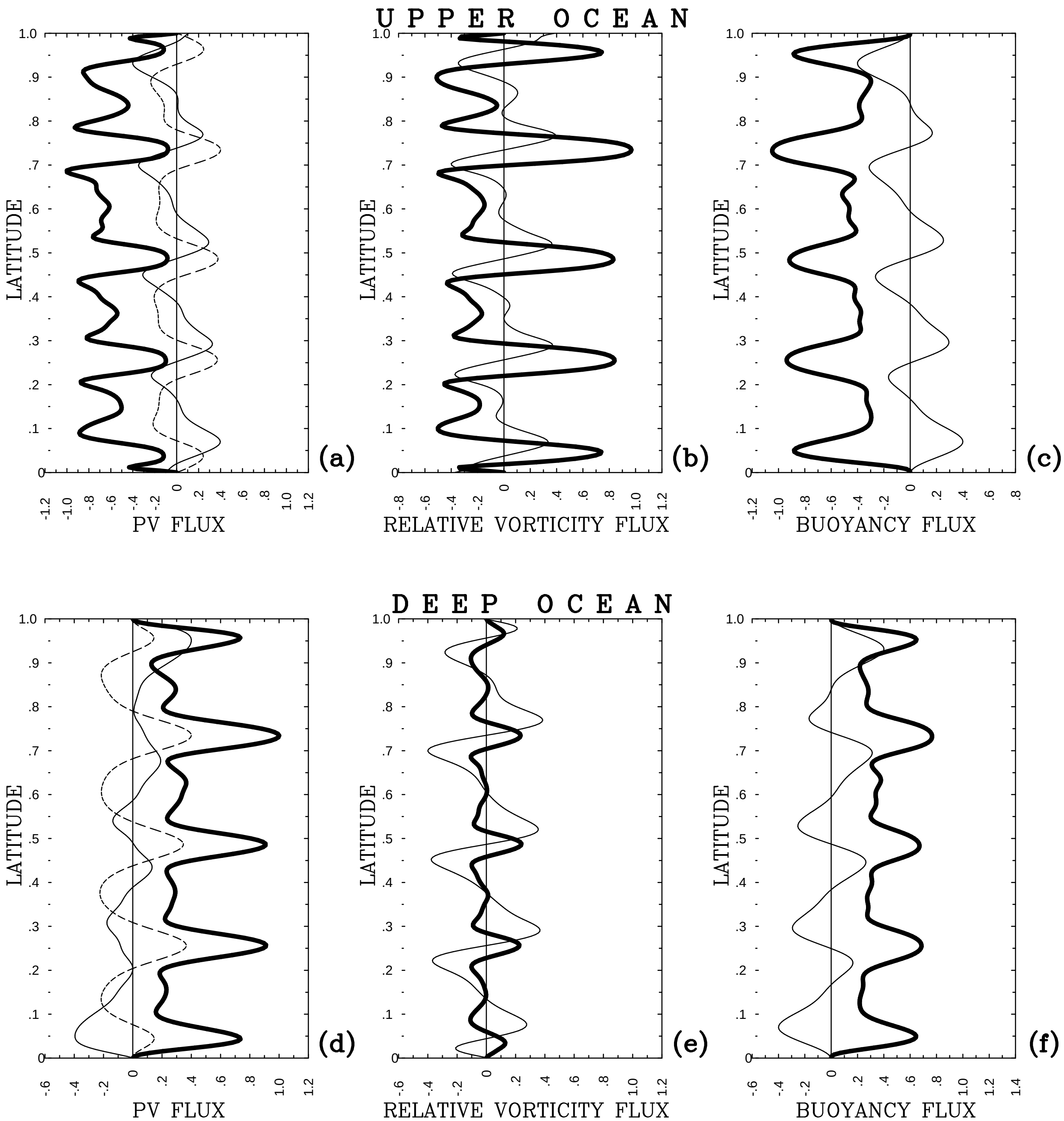

Figure 13: Time-mean meridional eddy fluxes of PV and its components in the reference EB solution. The upper row of panels describes fluxes of (a) PV, (b) relative vorticity, and (c) buoyancy in the upper ocean. The lower row of panels describes the same quantities but for the deep ocean. In each panel, the flux (thick curve) is normalized by the maximum value of the corresponding full PV flux. The corresponding profiles of the time-mean PV and its components are shown with thin curves, and the profiles of the time-mean zonal velocity are shown with dashed curves only on the left panels (both of these quantities have arbitrary units).

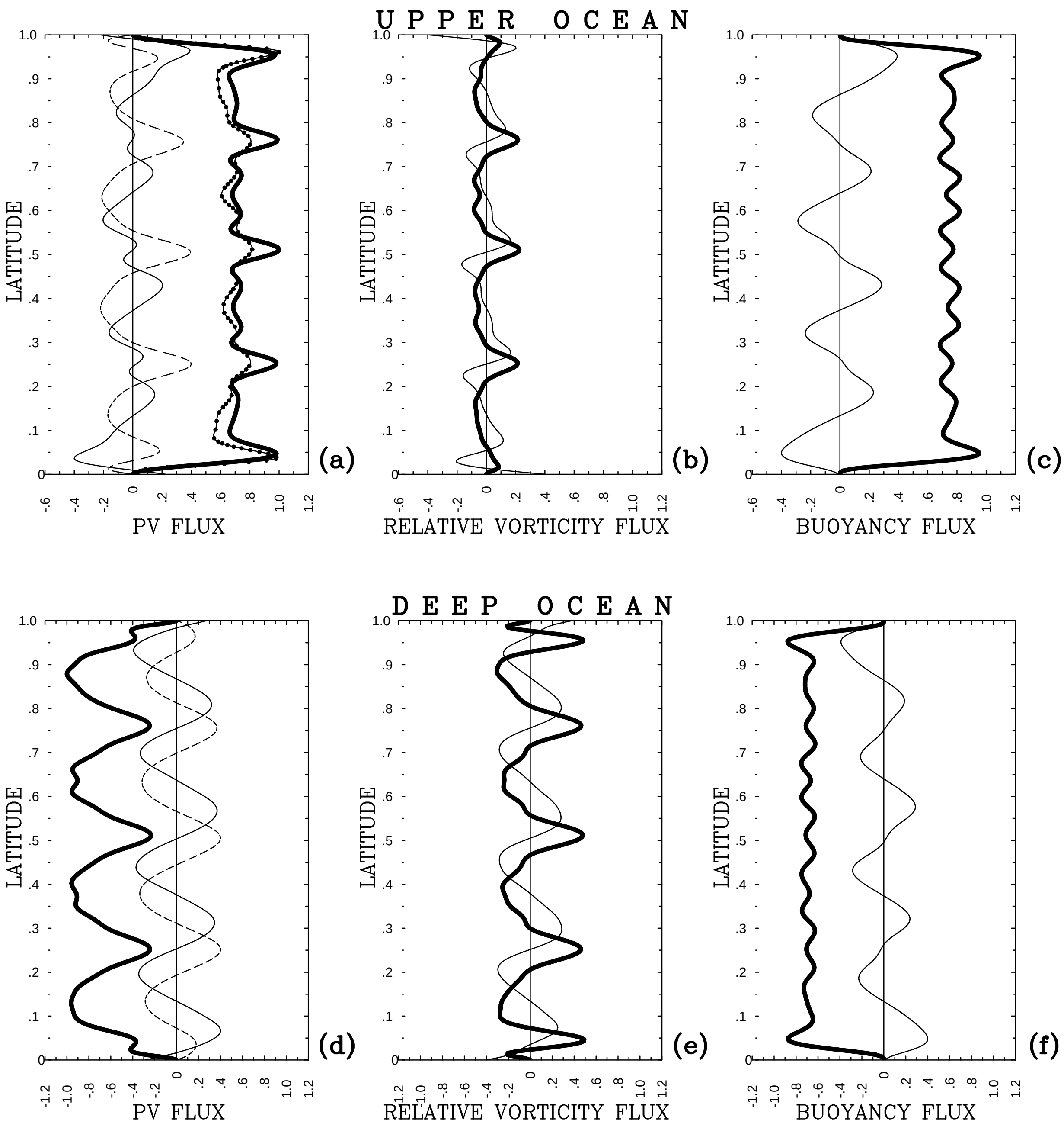

Figure 14: The same as Fig. 13, but for the reference WB solution.

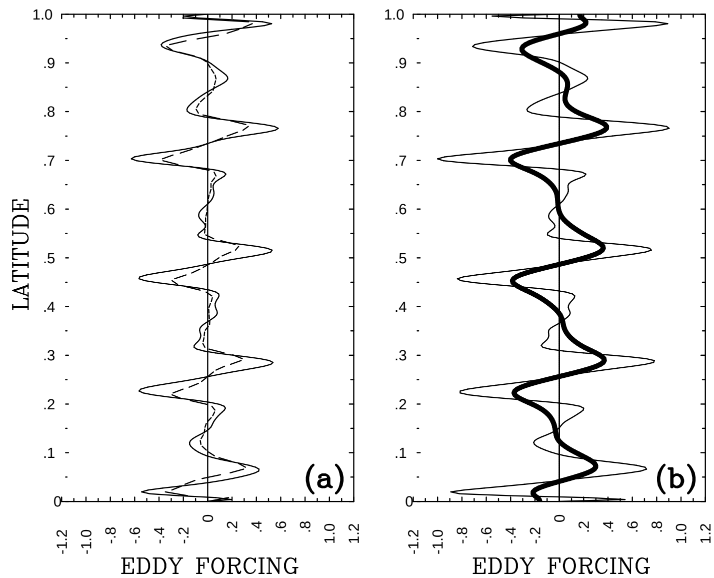

Figure 15: Barotropic eddy forcing and its components. (a) Barotropic-barotropic (continuous) and baroclinic-baroclinic (dashed curve) eddy forcing components of the reference, three-layer EB flow solution. (b) Full eddy forcing (thin) is shown along with the time-mean barotropic PV component (thick curve). The eddy forcing itself and its components are normalized by the maximum value of the eddy forcing; the barotropic PV is shown with arbitrary units.

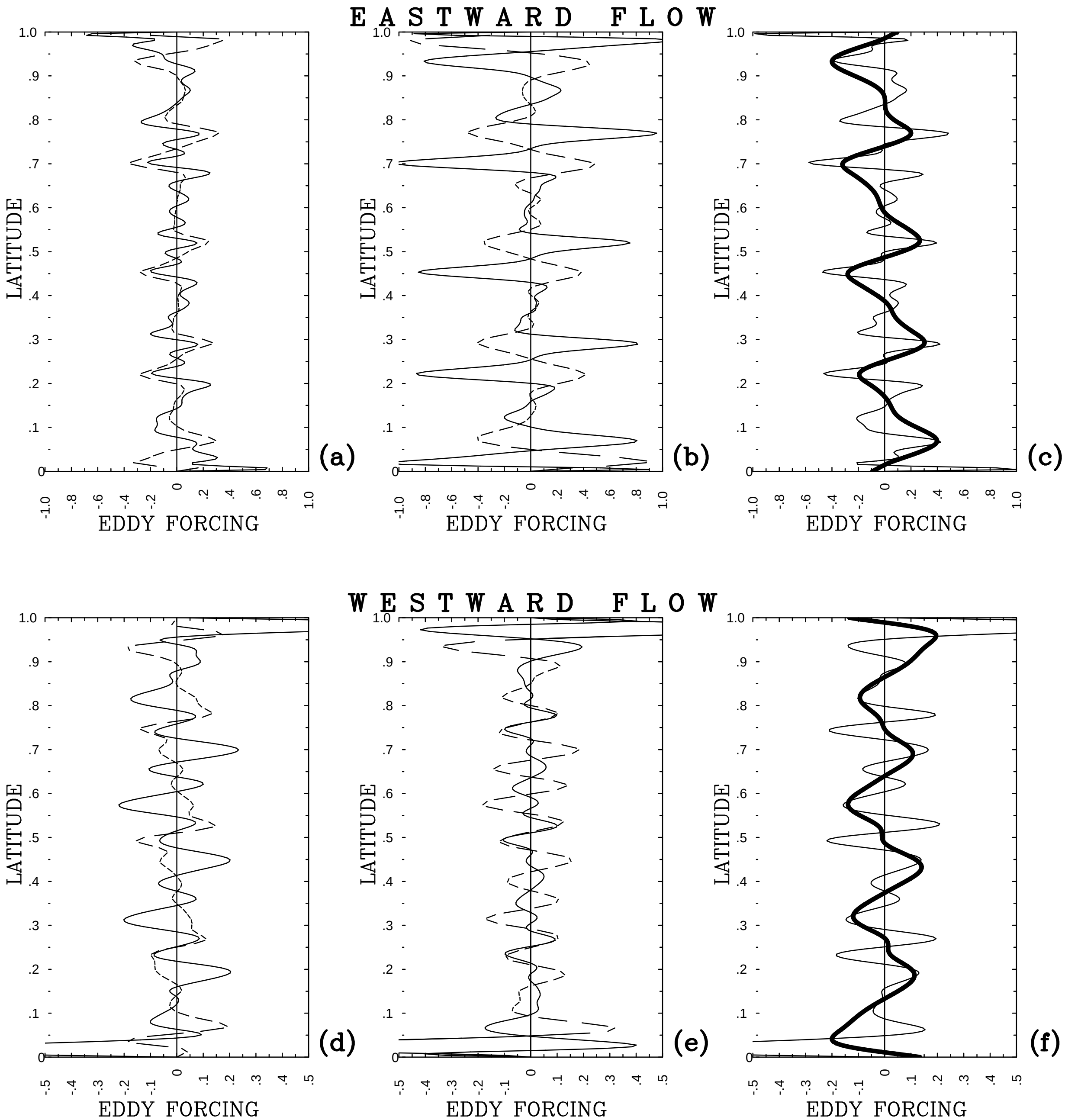

Figure 16: Baroclinic eddy forcing and its components. (a) Barotropic-baroclinic (thin) and baroclinic-baroclinic (dashed curve), (b) relative-vorticity (thin) and buoyancy (dashed curve) eddy forcing components of the reference, three-layer EB flow solution. (c) Full eddy forcing (thin) is shown along with the time-mean baroclinic PV component (thick curve). The eddy forcing itself and its components are normalized by the maximum value of the eddy forcing; the baroclinic PV is shown with arbitrary units. The lower row of panels shows the same quantities, but for the WB flow solution.

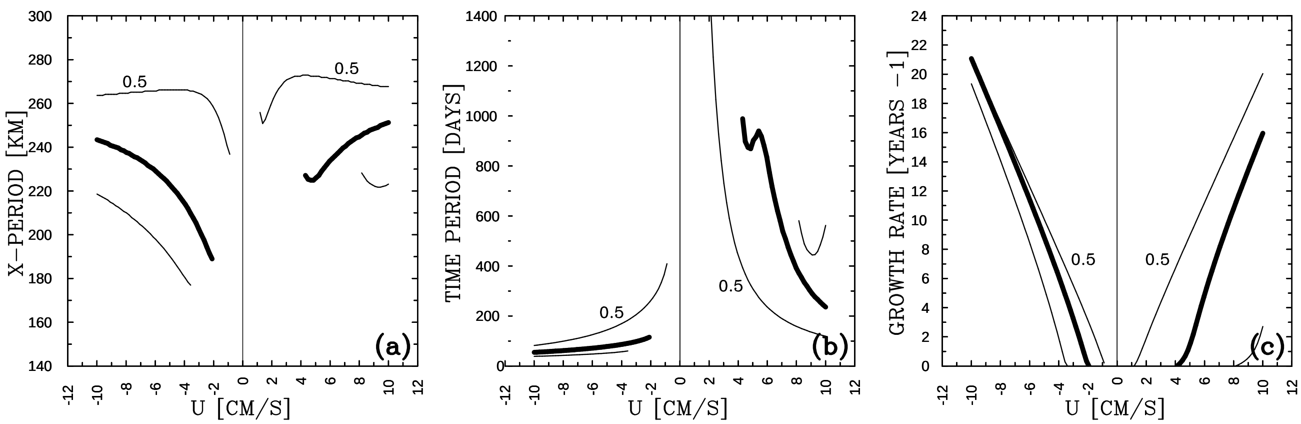

Figure 17: Properties of the most unstable eigenmode (i.e., "noodles") growing on the uniform zonal flow in the unbounded domain: dependence on the planetary vorticity gradient, β. (a) Zonal period, (b) time period, and (c) growth rate as functions of the upper-ocean background velocity. On each panel, thick curve corresponds to the reference values of $\nu = 100$ m^2 s^{-1}, $\gamma = 0$ s^{-1}, and $\beta = 2 \times 10^{-11}$ m^{-1} s^{-1}. There are three values of β considered: 0.5, 2, and 4×10^{-11} m^{-1} s^{-1} (curves corresponding to the lowest value are labeled by "0.5").

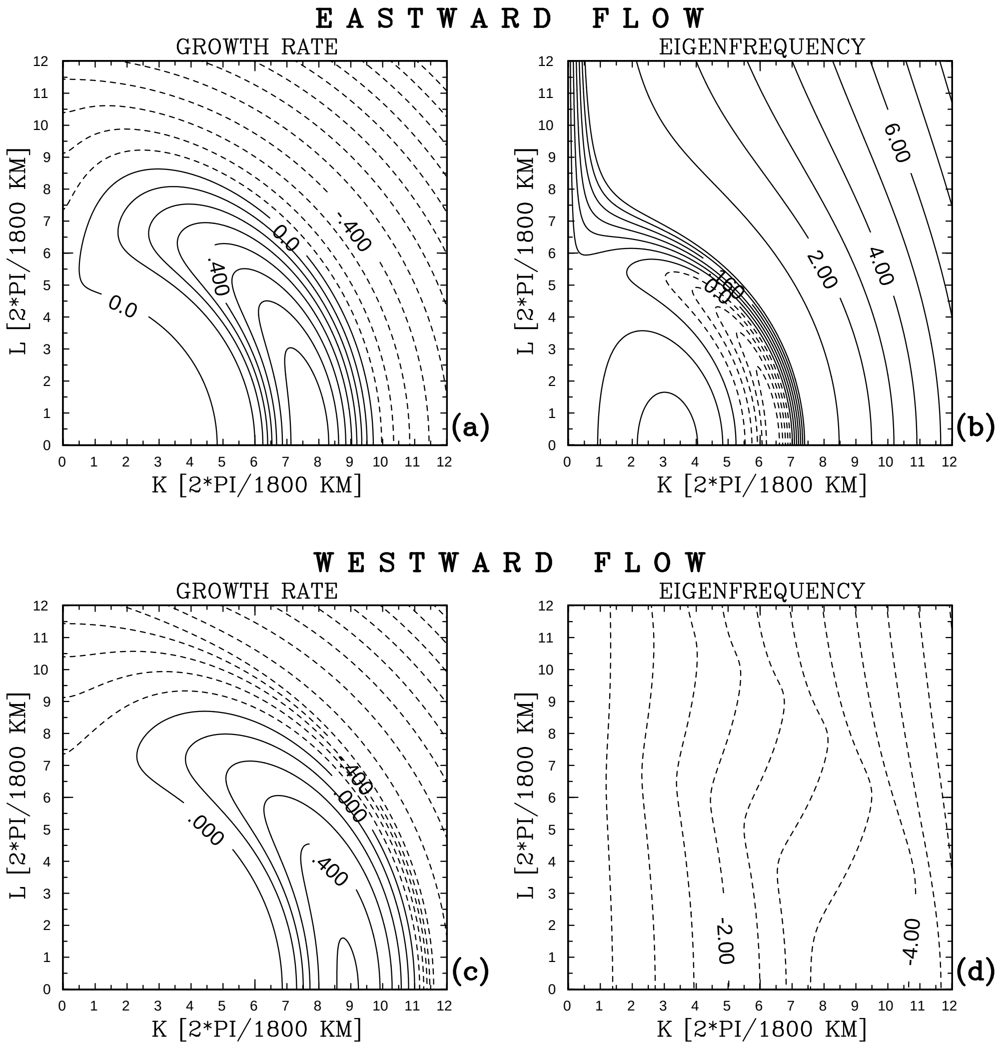

Figure 18: Dispersion relationship of the linear stability problem: uniform zonal flow in the unbounded domain. The upper row of panels shows (a) growth rate and (b) eigenfrequency of the reference EB flow as functions of the zonal (k) and meridional (l) wavenumbers. The lower row of panels shows the same values but for the reference WB flow. Contour intervals: (a) and (c) CI=0.1 years^{-1}; (b) CI=0.04 and 1.0 years^{-1} for the small and large eigenfrequencies, respectively; and (d) CI=0.5 years^{-1}. Positive/negative contours in the right panels correspond to the phase lines propagating to the east/west.

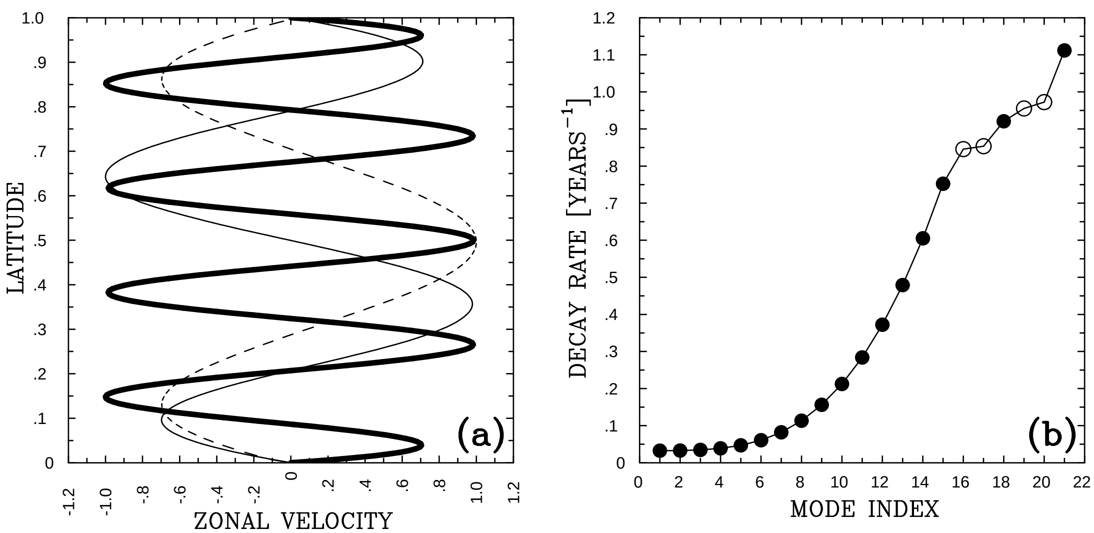

Figure 19: Annular eigenmodes. (a) Upper-ocean zonal velocity profiles of the second (dashed), third (thin), and eighth annular eigenmodes (thick curve), and (b) decay rates of the first 20 annular eigenmodes, ranked according to the increasing decay rate. The eigenmodes are calculated for the reference control parameters. Zonal velocities in (a) are normalized by their maximum absolute values. Filled/empty circles in (b) indicate predominantly baroclinic/barotropic eigenmodes.

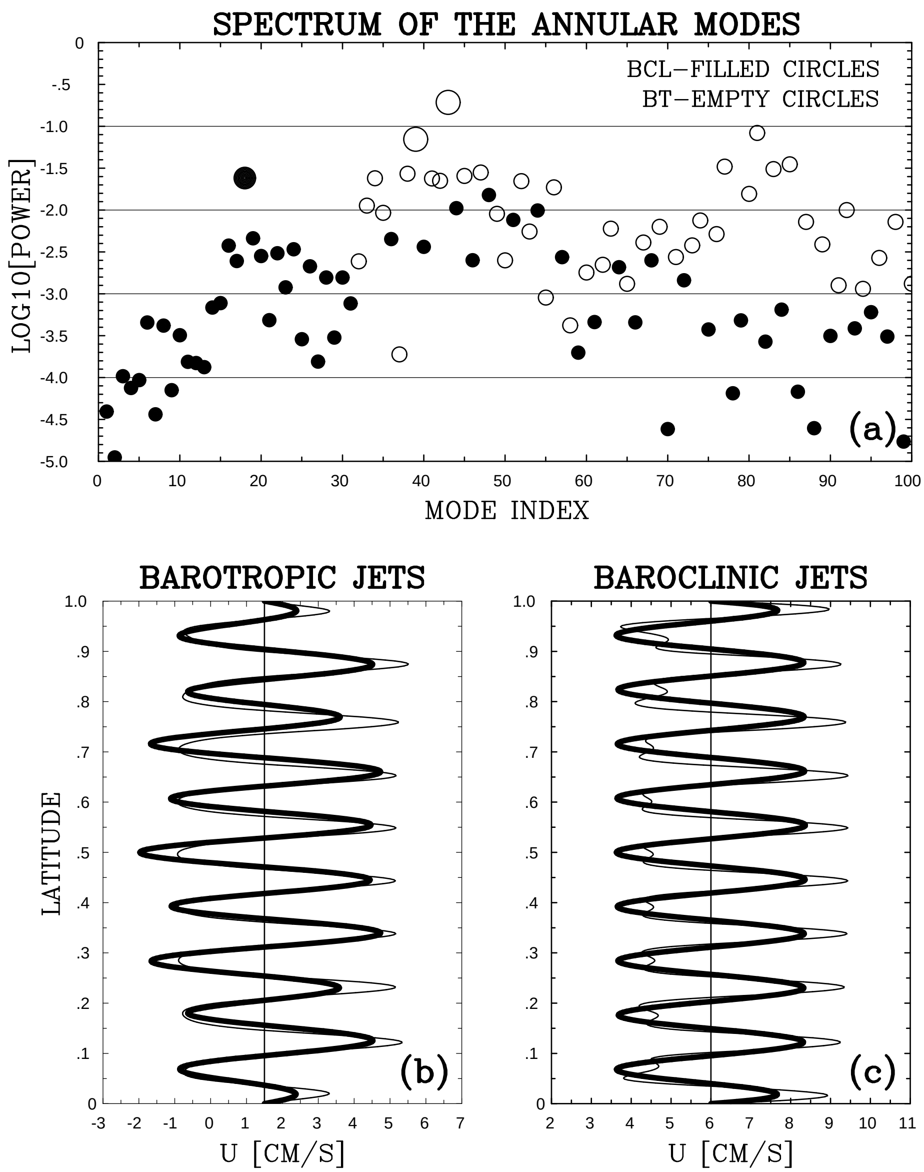

Figure 20: Evidence of the annular modes in the multiple-jet flow. (a) Normalized spectrum of the annular modes, $P_{ann}(n)$, where n is mode index, calculated for the time-mean flow shown in Fig. 3d. Predominantly baroclinic/barotropic modes are indicated with the filled/empty circles. Contributions of the leading (b) two barotropic and (c) one baroclinic annular modes (indicated by the large circles in panel (a)) to the jets are shown with thick curves, and the corresponding barotropic and baroclinic zonal velocity profiles are shown with thin curves.

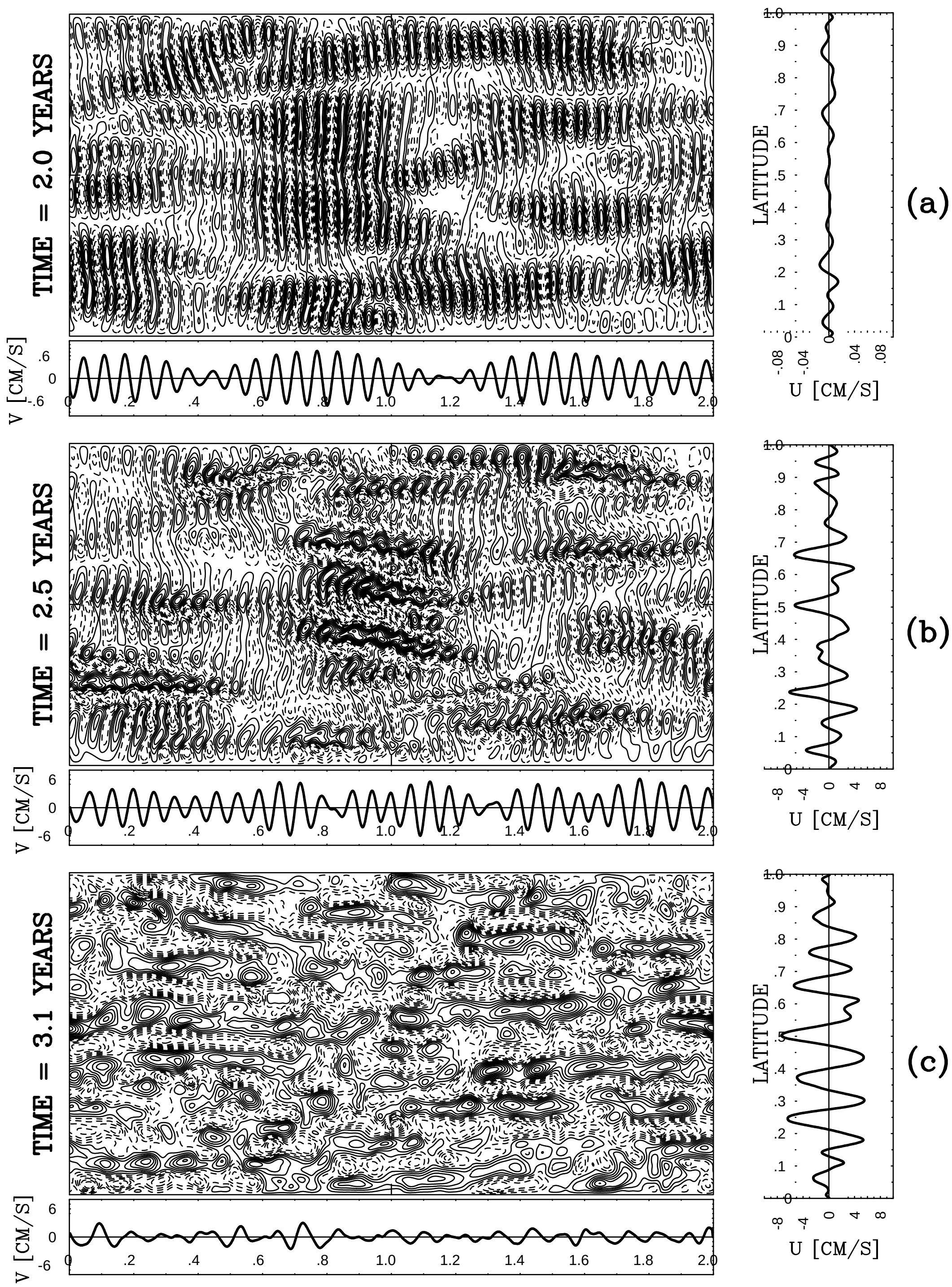

Figure 21: Spin up of the multiple jets. Instantaneous upper-ocean streamfunction is obtained (a) after 2 years of the model integration starting from small random perturbations, (b) 200 days later, and (c) another 200 days later (CI are (a) 0.4 Sv and (b,c) 5 Sv). The basin is twice as large in each dimension as the one used for the EB flow reference solution (compare with Fig. 2a,b), but all other parameters are the same. Panel to the right of each streamfunction field shows the corresponding zonally averaged zonal velocity, and panel below the streamfunction field shows meridionally averaged meridional velocity.

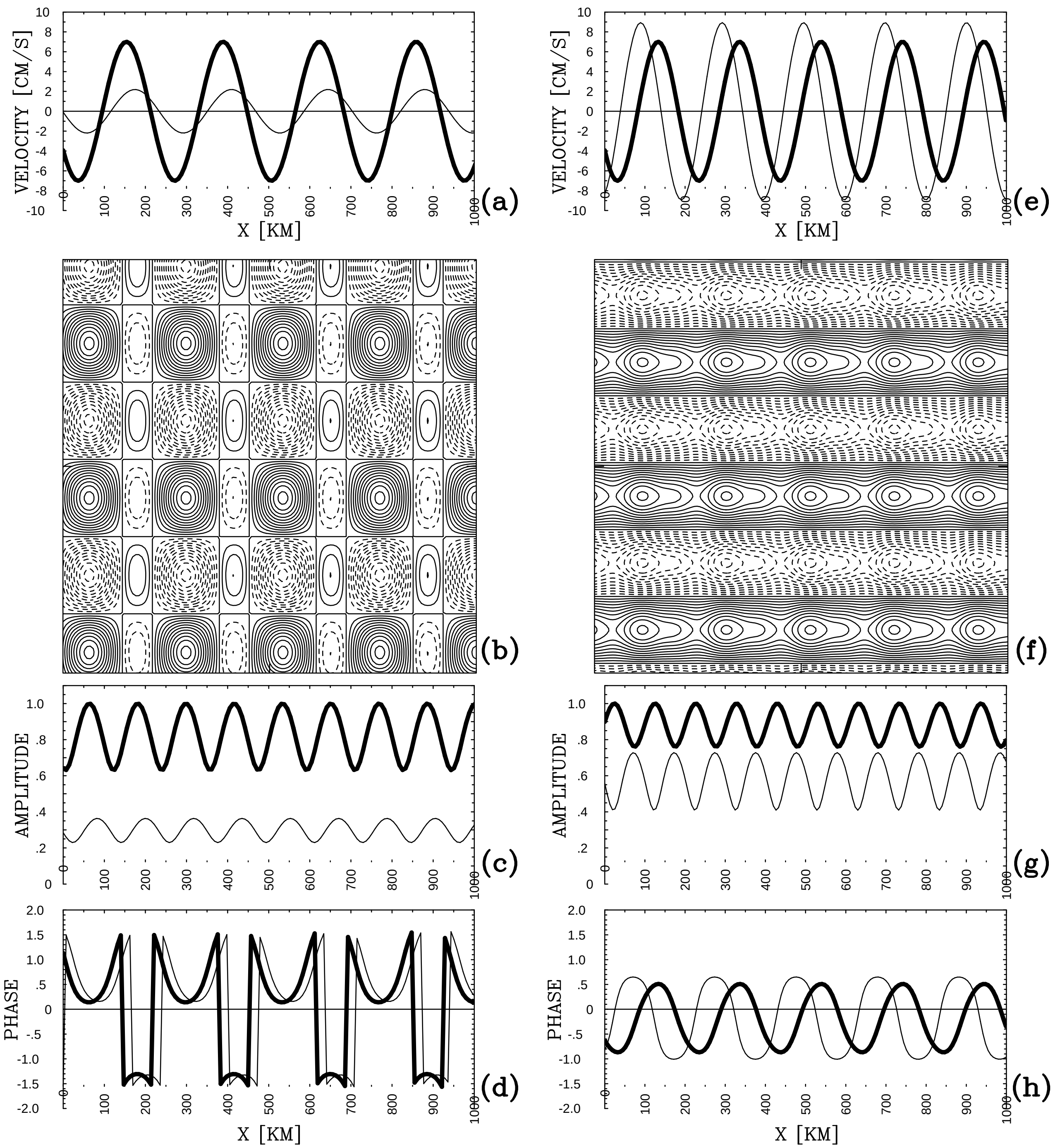

Figure 22: Critical eigenmodes of the finite-amplitude “noodles”. Left/right column of panels corresponds to the EB/WB reference solution. (a,e) Meridional velocity of the background “noodles” in the upper- (thick) and deep-ocean (thin curve) isopycnal layers. (b,f) Upper-ocean velocity streamfunction (arbitrary amplitude). (c,g) Amplitude (normalized by its upper-ocean maximum value) and (d,h) phase of the zonal component of the critical eigenmode.

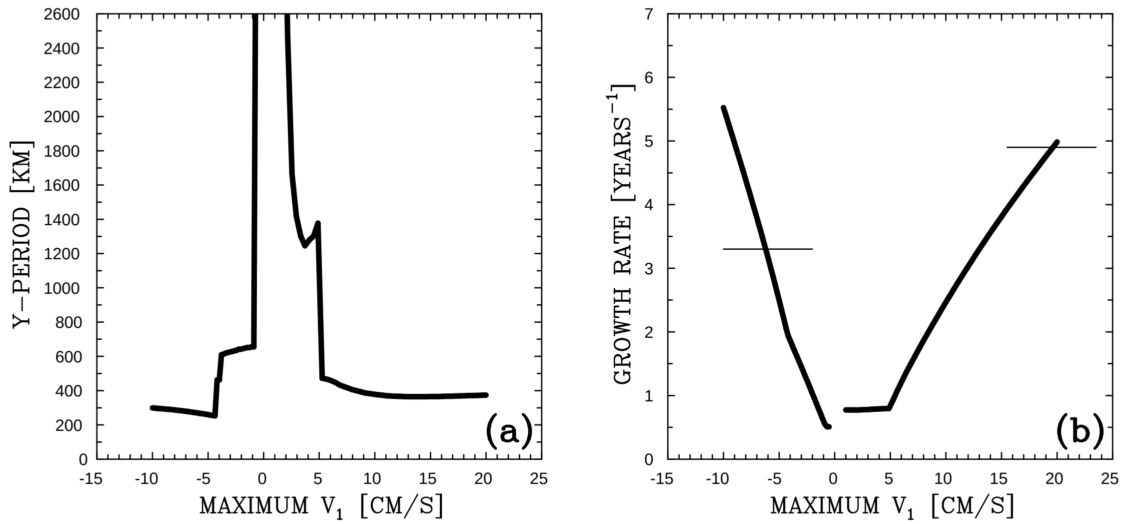

Figure 23: Stability properties of the finite-amplitude "noodles". (a) Meridional period and (b) growth rate of the critical eigenmodes of the EB and WB reference solutions. Positive/negative values of the maximum upper-ocean meridional velocity, V_1, indicate EB/WB flows. Thin horizontal lines in (b) indicate growth rates of the infinitesimal "noodles".

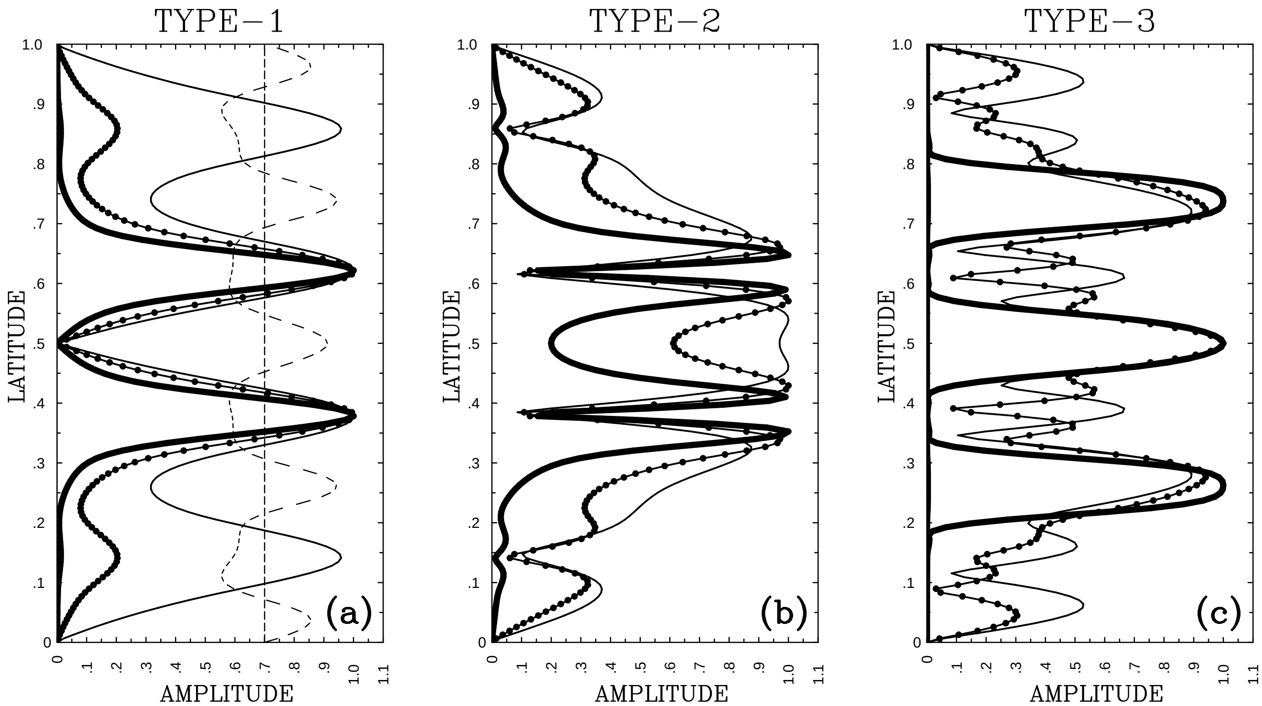

Figure 24: Localization of the "noodles" on the multiple jets. Amplitudes of the eigenmodes of (a) Type-1, (b) Type-2, and (c) Type-3 are shown for amplitude of the background jets, A_u, equal to 0.2 (thin), 0.5 (thin with filled circles), and 1.5 (thick curve). On panel (c), three isolated peaks corresponding to A_u=1.5 (thick curve) belong to three separate Type-3 eigenmodes trapped by the corresponding eastward jets (two more eigenmodes of this sort, trapped on the near-boundary eastward jets are not shown). Dashed curves in the panel (a) indicate the background and time-mean zonal velocities in the upper ocean (arbitrary units).

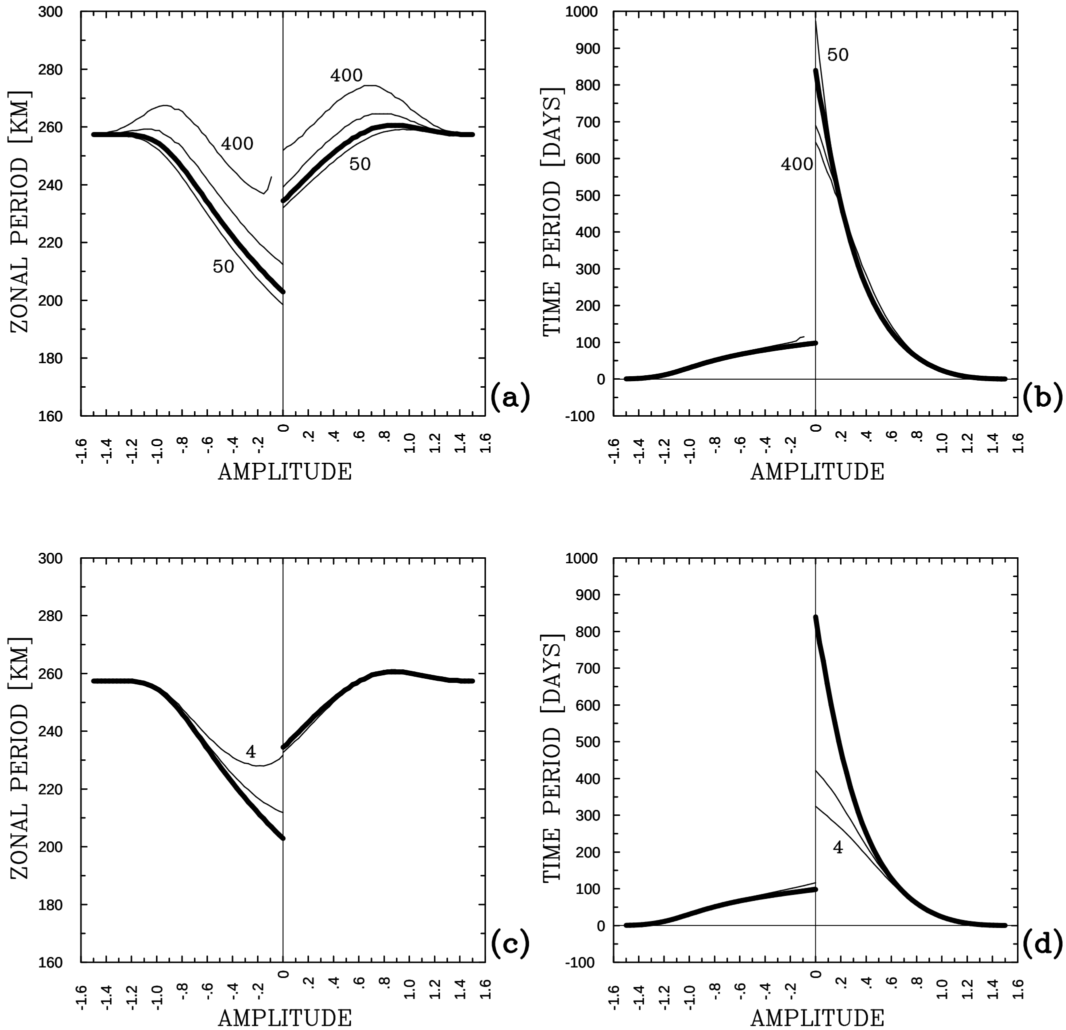

Figure 25: Stability properties of the multiple zonal jets. Dependence on the jets amplitude, A_u, eddy viscosity, ν, and bottom friction, γ, is explored. Left/right half of each panel corresponds to the WB/EB flow reference parameters. Upper panels show dependence on A_u of (a) zonal and (b) time periods of the critical eigenmode, for $\nu = 50, 100, 200$ and 400 m^2 s^{-1}. Left/right half of each panel corresponds to the WB/EB flow reference parameters. Amplitudes corresponding to the WB flow reference solution are indicated as $-A_u$, and amplitudes equal to the minus and plus unity correspond to the actual time-mean jets from the WB and EB flow reference solutions, respectively. Lower panels show the same properties but for $\gamma = 0, 2$, and 4 $\times 10^{-7}$ s^{-1}. Functions corresponding to the reference values of $\nu = 100$ m^2 s^{-1} and $\gamma = 0$ are shown with thick curves, and, for clarity, some curves are marked with the corresponding values of ν and γ.

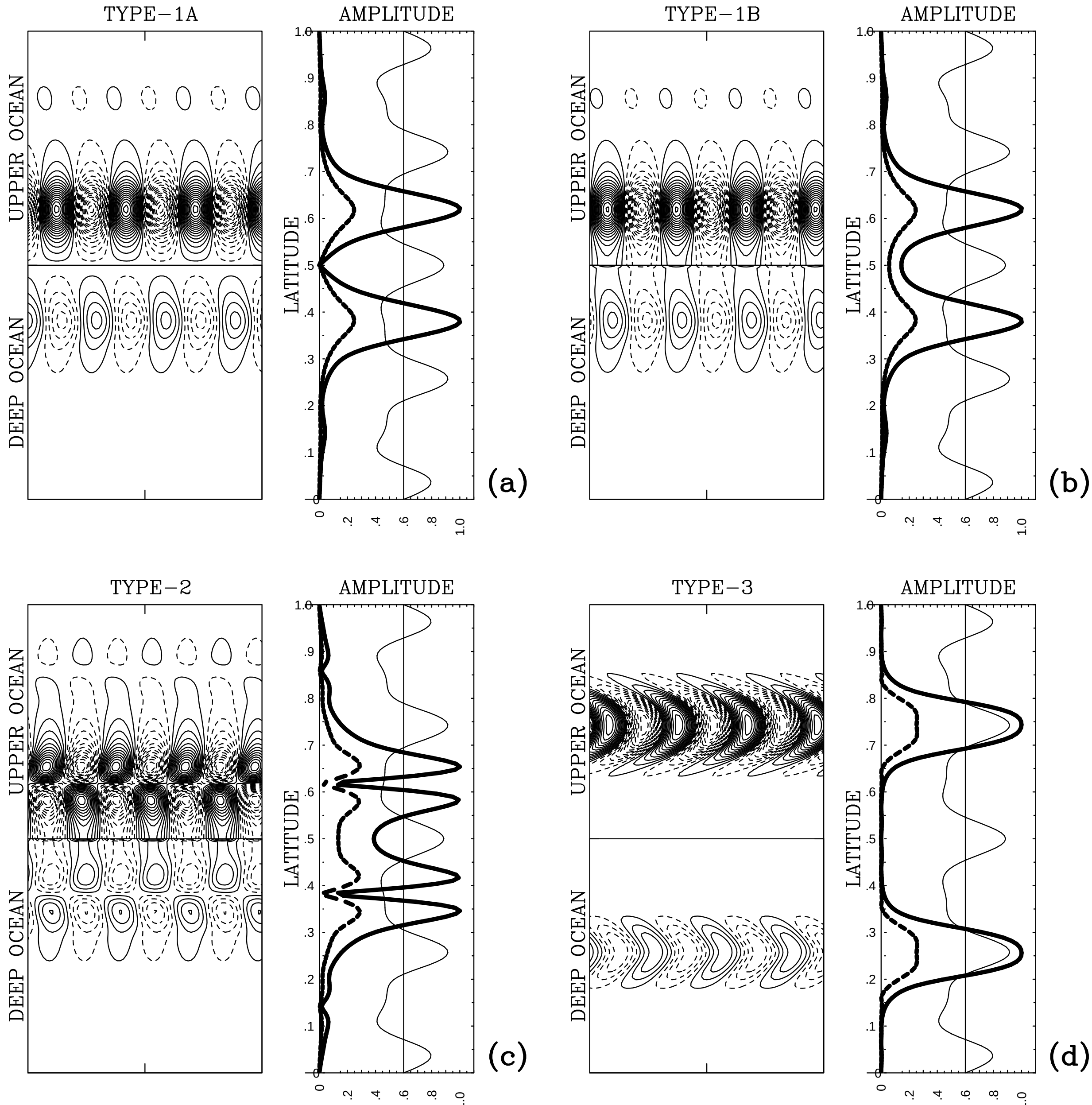

Figure 26: Unstable eigenmodes of the EB flow with multiple zonal jets. Eigenmodes shown have indices (a) 1, (b) 2, (c) 8, and (d) 9, ordered in terms of the increasing decay rates. Contour plots show velocity streamfunctions of the eigenmode patterns in the 1/4-period section of the channel. Since the eigenmodes are either symmetric or antisymmetric with respect to the middle latitude of the channel, the upper-ocean pattern is shown in the northern half of the plot and the deep-ocean one — in the southern half. All of the eigenmodes are normalized by the energy norm, and the (arbitrary) contour interval is the same throughout the figure. Sub-panels to the right of the contour plots show corresponding amplitudes of the upper- (thick continuous) and deep-ocean (thick dashed curve) components of the eigenmodes; the curves are normalized by the upper-ocean maximum amplitude. In each panel, thin curve with straight line in the middle show the time-mean zonal velocity profile of the jets (with arbitrary units).

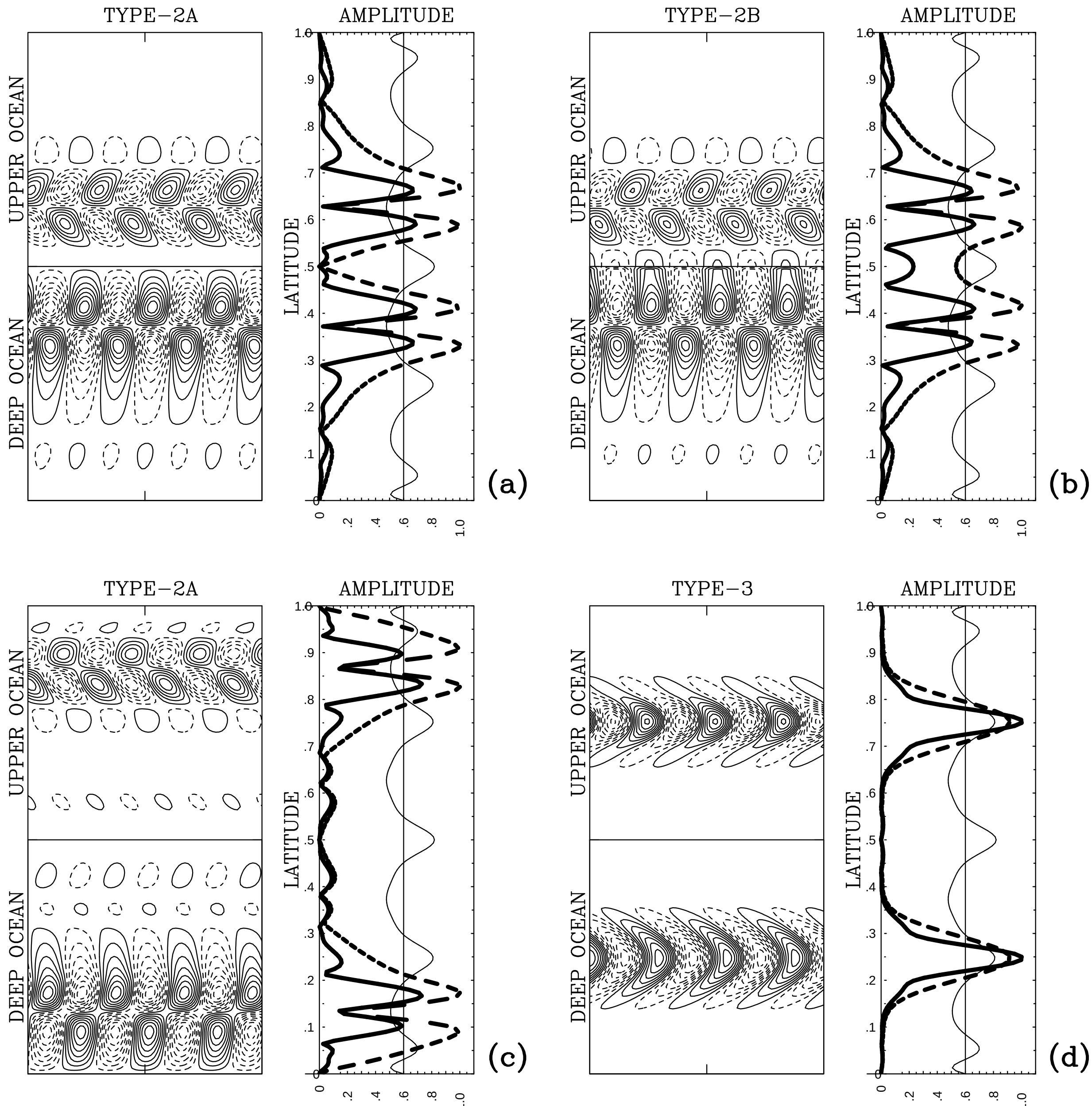

Figure 27: The same as Fig. 26, but for the WB flow. The eigenmodes shown have indices (a) 1, (b) 2, (c) 3, and (d) 7.

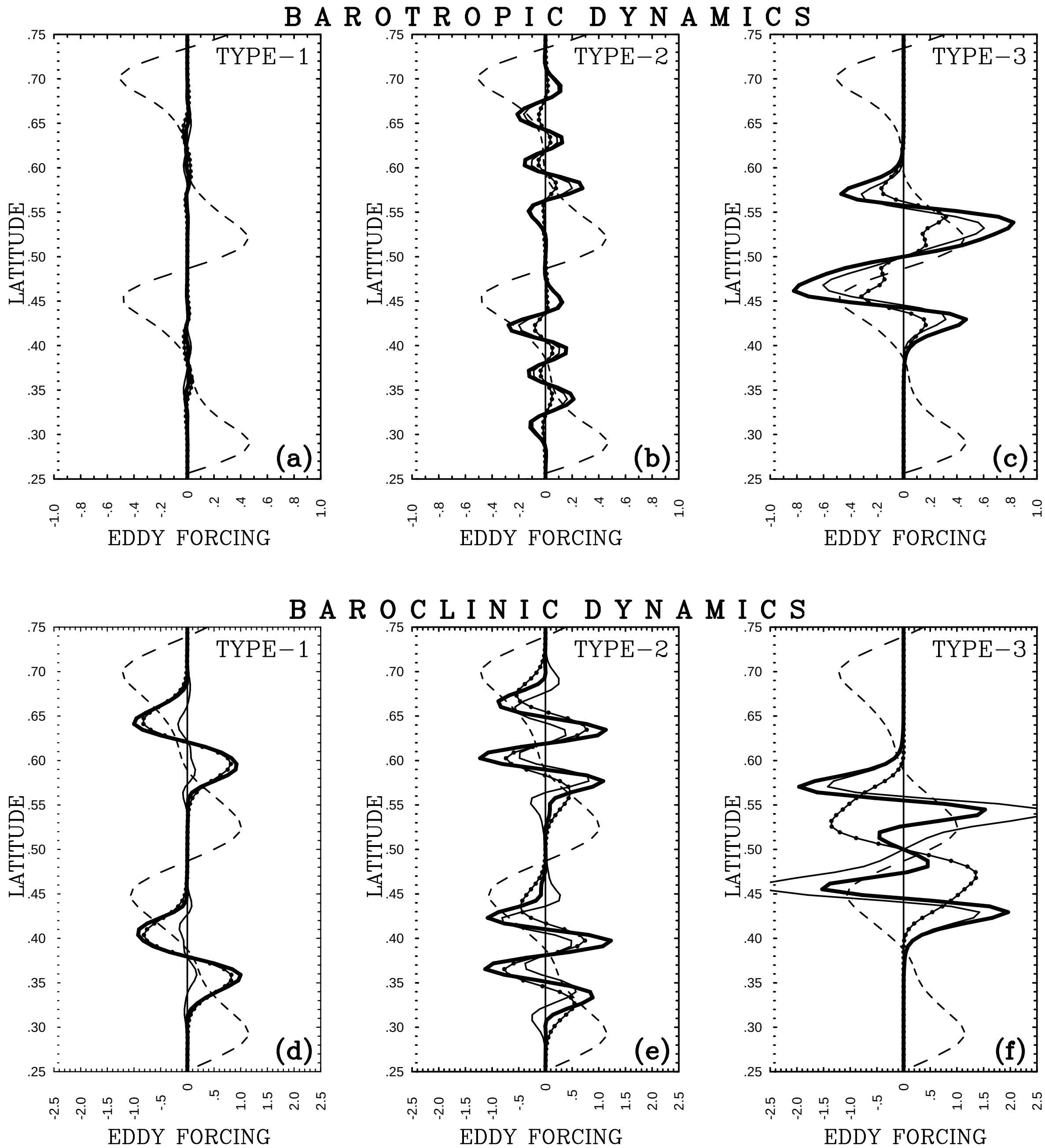

Figure 28: Eddy forcing of the meridionally localized eigenmodes and its components: EB flow. Upper row of panels corresponds to the barotropic eddy forcing of the gravest eigenmodes localized in the center of the channel: (a) Type-1, (b) Type-2, and (c) Type-3 eigenmodes. Upper row of panels: Full eddy forcing (thick), as well as its barotropic-barotropic (thin) and baroclinic-baroclinic (thin with filled circles) components are shown. Lower row of panels: Full eddy forcing (thick), as well as its Reynolds stress (thin) and form stress (thin with filled circles) forcing components are shown. The corresponding time-mean PV anomalies are shown with dashed curve (arbitrary value). Each eddy forcing curve is normalized by the maximum absolute value of the eddy forcing corresponding to the gravest eigenmode.

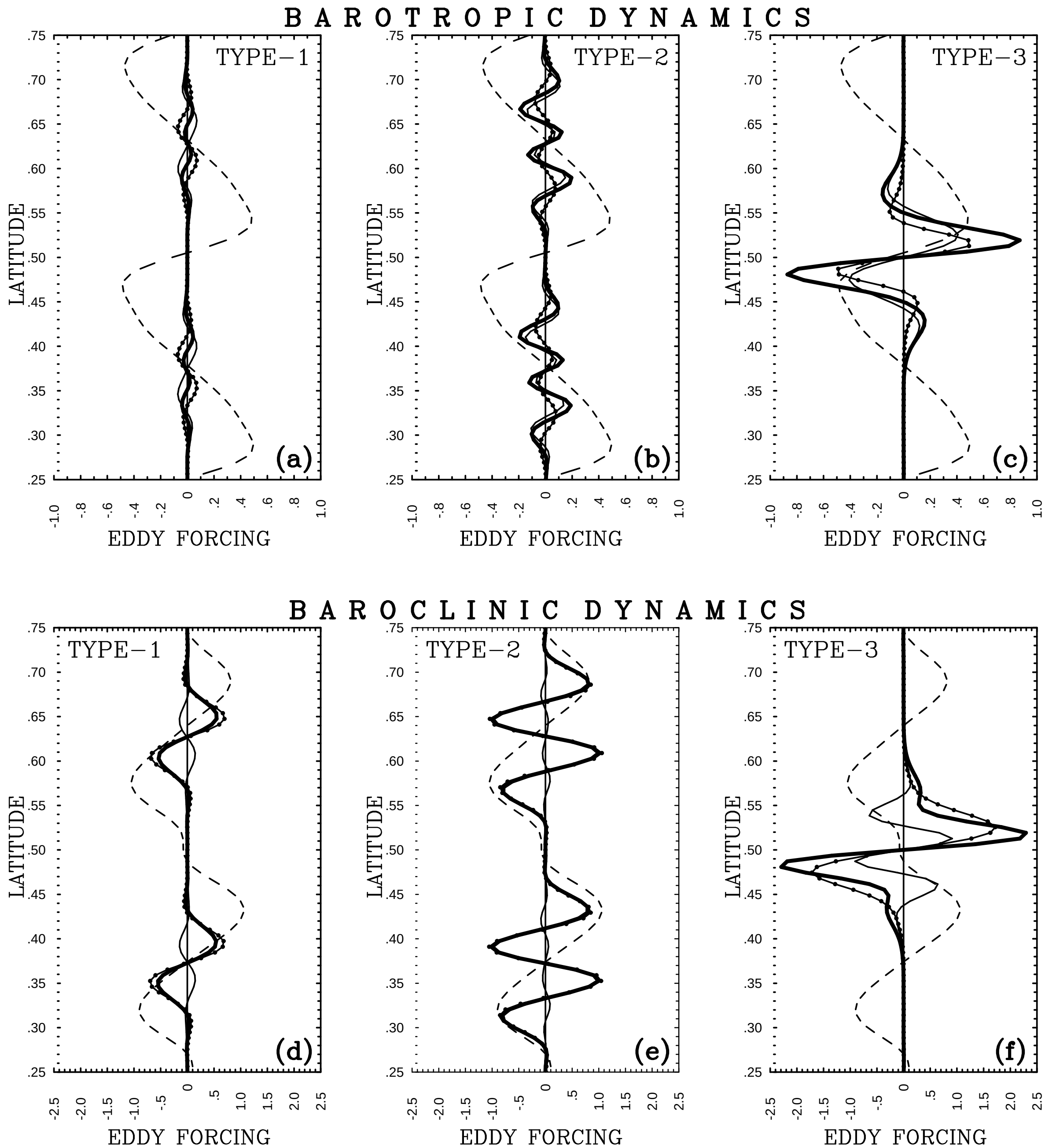

Figure 29: The same as Fig. 28, but for the WB flow.

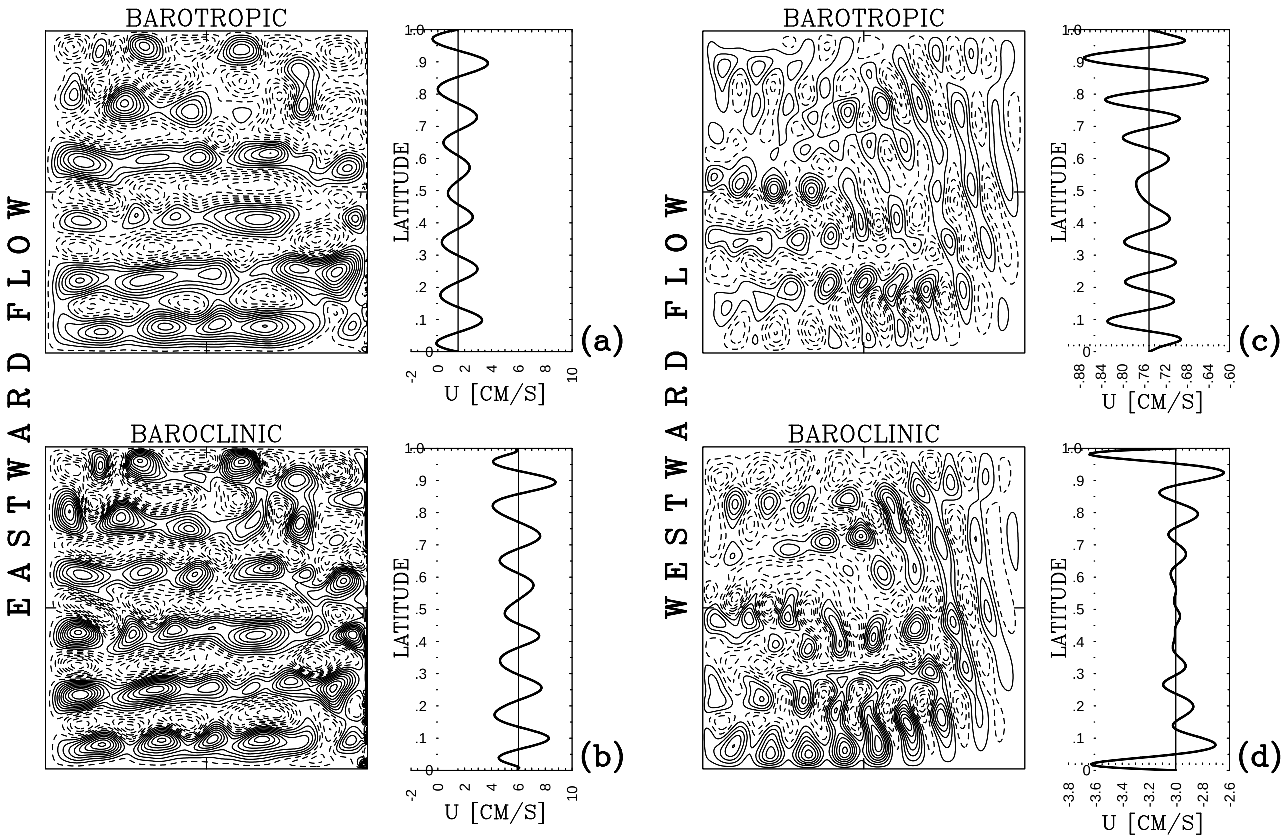

Figure 30: Multiple-jet flow in the two-layer closed basin. Instantaneous (a) barotropic and (b) baroclinic velocity streamfunctions in the eastward-flow regime with $U_1 = 6.5$ cm s^{-1} (CI=2.5 Sv). The corresponding time-mean zonal velocity profiles are shown in the right panels. Panels (c) and (d) show the same quantities as the left panels but for the westward-flow regime with $U_1 = -2.5$ cm s^{-1} (CI=1 Sv).

Table 1: Parameters used in the two-layer channel model. The other parameters are kept fixed: $L_x = 2L_y$, $Rd_1 = 25$ km, $H_1 = 1$ and $H_2 = 3$ km, and U_2 is zero.

	EB: U_1	WB: U_1	$\beta\times 10^{11}$	ν	$\gamma\times 10^{7}$	$\lambda\times 10^{7}$	L_y
reference value:	+6 cm/s	-3 cm/s	2 m^{-1}s^{-1}	100 m^{2}s^{-1}	0 s^{-1}	2 m^{-2}s^{-1}	1800 km
variation:	+4 $\div$ +10	-1.5 $\div$ -8	0.3 $\div$ 3	60 $\div$ 500	0 $\div$ 4	0 $\div$ 20	$L_y \rightarrow 2L_y$

Table 2: Vertical-mode representation of the eddy forcing in the barotropic zonal-channel dynamics. The non-zero ρ-terms are shown for the three- and two-layer (in brackets) multiple-jet reference solutions.

	$\rho_{11}^{(1)}$	$\rho_{22}^{(1)}$	$\rho_{33}^{(1)}$
EB:	+0.47 (+0.72)	+0.43 (+0.28)	+0.10
WB:	+0.63 (+0.63)	+0.34 (+0.37)	+0.03

Table 3: The same as Table 2, but for the first baroclinic dynamics. The columns and rows correspond to the first and second indices of $\rho^{(2)}_{kl}$, respectively. The ρ-terms with non-zero eddy buoyancy forcing are split into the Reynolds stress and form stress forcing components indicated by [R] and [B], respectively. The two-layer ρ-terms are shown in brackets. Empty sections of the Table correspond to $\rho^{(2)}_{kl} = 0$.

	1	2	3
1		WB: +1.43=+0.61[R]+0.82[B] (WB: +1.81=+0.70[R]+1.11[B]) EB: +0.27=+0.32[R]-0.06[B] (EB: -0.28=+0.19[R]-0.47[B])	
2	WB: -0.88 (WB: -0.90) EB: +0.48 (EB: +0.78)	WB: +0.02 (WB: +0.09) EB: +0.07 (EB: +0.50)	WB: +0.58=+0.10[R]+0.48[B] EB: +0.14=+0.05[R]+0.09[B]
3		WB: -0.18=-0.07[R]-0.11[B] EB: +0.01=-0.02[R]+0.03[B]	WB: +0.03 EB: +0.02

Table 4: The same as Table 3, but for the second baroclinic dynamics.

	1	2	3
1			WB: +1.03=+0.24[R]+0.80[B] EB: -0.84=+0.22[R]-1.06[B]
2		WB: -0.01 EB: +0.38	WB: +0.36=+0.06[R]+0.30[B] EB: +1.11=+0.29[R]+0.82[B]
3	WB: -0.24 EB: +0.54	WB: -0.16=-0.09[R]-0.07[B] EB: -0.12=0.07[R]-0.19[B]	WB: +0.01 EB: -0.07

Table 5: Projection on the time-mean jets of the eddy forcing associated with critical eigenmodes of the meridionally localized types. Correlation values labeled by BT/BCL correspond to the barotropic/baroclinic dynamics; labels EB and WB indicate direction of the background flow; and parameter A_u indicates strength of the multiple jets.

	EB: A_u=0.7	EB: A_u=1.0	EB: A_u=1.3	WB: A_u=0.7	WB: A_u=1.0	WB: A_u=1.3
Type-1: BT	-0.08	-0.02	-0.01	-0.06	-0.05	-0.02
Type-1: BCL	+0.24	+0.17	+0.13	+0.33	+0.30	+0.23
Type-2: BT	-0.19	-0.07	-0.06	+0.02	+0.01	+0.01
Type-2: BCL	+0.23	+0.16	+0.10	+0.14	+0.18	+0.19
Type-3: BT	+0.40	+0.29	+0.23	+0.34	+0.22	+0.19
Type-3: BCL	+0.01	-0.02	-0.04	-0.22	-0.14	-0.31